Discriminating Materials Using a Multi-particle Approach in an Active Interrogation Environment

by

Jason T. Nattress

A dissertation submitted in partial fulfillment
of the requirements for the degree of
Doctor of Philosophy
(Nuclear Engineering and Radiological Sciences)
in the University of Michigan
2018

Doctoral Committee:

Professor Igor Jovanovic, Chair
Professor Emeritus Frederick Becchetti Jr.
Dr. Namdoo Moon
Professor Sara Pozzi

"... to find the way by which the miraculous inventiveness of man shall not be dedicated to his death, but consecrated to his life." -President Eisenhower

Jason T. Nattress

jtnatt@umich.edu

ORCID ID: 0000-0001-5449-2520

Acknowledgments

I would like first to thank my advisor, Professor Igor Jovanovic. Your immeasurable guidance, motivation, and thoughtfulness helped propel me through the finish line. I am incredibly grateful for the opportunities you provided me and for helping me grow the knowledge and skills needed to succeed as a scientist. My gratitude extends to my other committee members: Professor Sara Pozzi, Professor Emeritus Frederick Becchetti Jr., and Dr. Namdoo Moon. Their recommendations and insightful direction forced me to examine my research from a broader perspective.

I thank Peter Binns of Massachusetts Institute of Technology (MIT) Bates Research and Engineering Center for help with operating the linear accelerator and all my other colleagues at MIT that were a part of the *Low-Dose Inspection for Nuclear Threats Using Monochromatic Gamma-Rays* project. I thank Professor Zoubedia Ounaies, Albert Foster, and Dr. Amira Meddeb of the Pennsylvania State University for their contributions to the development of one of the detectors used in this work. I would like to thank Dr. Paul Rose and Professor Anna Erickson of Georgia Institute of Technology for their contributions to the radiography experiments and more specifically to Paul for being my experimental campaign roommate, commiseration partner, and friend. I thank Professor John Mattingly of North Carolina State University and Jesson Hutchinson of Los Alamos National Laboratory for assistance with planning and carrying out the experiment at the Device Assembly Facility. I thank Professor Graham Peaslee and Sean McGuinness, and all of the other folks at Institute for Structure and Nuclear Astrophysics that helped with the experiments at the University of Notre Dame.

I thank Dr. Michael Mayer. You have been my big brother through this journey, without whom I most likely would still be trying to figure out what a pointer is. I thank all of my family and friends for their continued love and support, especially my mother for showing me what perseverance truly is. I thank Andrew Natoli for being my other big brother during this journey whose ongoing encouragement cannot be overstated. Most importantly, I thank my wife, Rosalee Nattress, for listening to me ramble on and on about my research. Her confidence in me and continued encouragement has been and will be my guiding light.

Lastly, I thank the funding sources that made this research possible. This research was performed under the appointment of the Nuclear Nonproliferation International Safeguards Fellowship Program sponsored by the National Nuclear Security Administration's Office of International Safeguards (NA-241). This work was partially supported by the U.S. Department of Homeland Security (2014-DN-077-ARI078-02 and 2015-DN-077-ARI096) and by the Consortium for Verification Technology under U.S. Department of Energy National Nuclear Security Administration award number DE-NA0002534.

Contents

List of Figures

List of Tables

Acronyms

AI active interrogation.

DPP PSD Digital-Pulse-Processing Pulse-Shape Discrimination.

DU depleted uranium.

FNGR fast neutron/gamma-ray radiography.

HEU Highly enriched uranium.

ISNAP Institute for Structure and Nuclear Astrophysics.

LDPE low density polyethylene.

MIT Massachusetts Institute of Technology.

PSD pulse-shape discrimination.

PSP pulse-shape parameter.

PVT polyvinyl toluene.

RFQ radio-frequency quadrupole.

SNM special nuclear material.

UND University of Notre Dame.

WGPu weapons grade plutonium.

WGU weapons grade uranium.

Abstract

Spectroscopic transmission radiography using MeV-class radiation is a powerful method for identifying the elemental composition of dense objects. This method has been used extensively in nuclear nonproliferation, nuclear safeguards, and nuclear security applications that employ active interrogation (AI). Of particular interest is the identification of special nuclear material (SNM) which relies on a characteristic signature such as energy-dependent transmission or the emission of delayed radiation unique to the fission process that occurs in SNM. Neither fast-neutron nor photon probes are universally applicable, as each suffers from poor penetrability at one extreme of the atomic number spectrum. While dual-energy photon radiography is adequate for the measurement of materials from low to moderate atomic numbers, its discrimination performance quickly diminishes at high atomic numbers, leading to poor contrast between elements such as lead and uranium. Further, transmission radiography is not sufficient to confirm or exclude the presence of SNM. More information about the interrogated material may be revealed if two primary measurement modes offered by AI (spectroscopic transmission radiography and the detection of fission signatures) commonly used independently are integrated. This dissertation combines these sources of information to characterize the elemental composition with improved accuracy and to indicate the presence of fissile material.

In previous work, we demonstrated a method based on the ^{11}B(d,nγ)^{12}C reaction that uses photon transmission spectroscopic signatures to deduce certain material properties. The deuteron-induced stripping reaction on ^{11}B produces two prominent gamma-ray ener-

gies (4.4 and 15.1 MeV) from the decay of the excited product nucleus, ^{12}C. Additionally, multiple quasi-monoenergetic neutrons are produced, with their energies governed by the reaction kinematics, specifically the incident deuteron energy and neutron emission angle. In this work, gamma rays and neutrons were detected with an organic liquid scintillator, which possesses the ability to discriminate between neutrons and photons. The relative attenuation at two prominent gamma-ray energies was used to simultaneously measure the aerial density and effective atomic number of materials spanning atomic numbers from thirteen to ninety-two. This was accomplished by measuring the light output distributions of the unattenuated and attenuated gamma rays and isolating the contributions of the gamma rays at specific energies.

Material identification by transmission radiography was then investigated using a combination of neutrons and gamma rays produced by nuclear reactions induced by a deuteron incident on a boron nitride target. The neutron time-of-flight technique was employed to measure the transmission over a broad range of neutron energies and is combined with spectroscopic photon transmission to provide a more accurate measurement of elemental composition. It is shown that the buildup and decay of delayed-neutron emission can be used not only detect the presence of fissionable material, but also to further distinguish among various uranium isotopes and infer the uranium enrichment level. This work demonstrates the first use of a single multi-particle, multi-energy source with a single type of detector to perform neutron and photon radiography simultaneously and distinguish between uranium isotopes based on the long-lived delayed neutron decay and buildup rates.

Chapter 1

Detecting special nuclear material

1.1 Introduction

Detection of SNM remains one of the greatest challenges facing the nuclear security and nonproliferation community, where small signal-to-background ratios and complex geometries lead to challenging measurement scenarios. AI has attracted increasing interest in recent years because it can enhance the strength of the fission signature and penetrate dense shielding. Monoenergetic or near-monoenergetic AI sources may offer additional benefits, such as improved performance in radiography and higher fission rates per unit of radiation dose [1]. Low-energy nuclear reactions represent a promising quasi-monoenergetic AI source. Such sources could help to construct low-dose, small-footprint systems, which could be used to detect illicit movement of SNM as well as support a broad range of measurements in the area of nuclear security and nuclear nonproliferation.

This dissertation presents a multifaceted AI methodology that applies to many nuclear nonproliferation and nuclear security applications. The methodology can be used in its entirety, or an individual component can be utilized for specific applications. To infer material properties of an unknown object, the system uses two primary AI signatures: radiography and the detection of a fission signature. Neutron and photon spectroscopic

transmission are used in tandem to perform material identification. Transmission radiography alone, however, is not sufficient to confirm or exclude the presence of SNM. Further material identification is performed by measuring the fission signature. Specifically, the delayed neutron signature is measured to determine uranium enrichment. Figure 1.1 shows the steps and different decision points of the methodology.

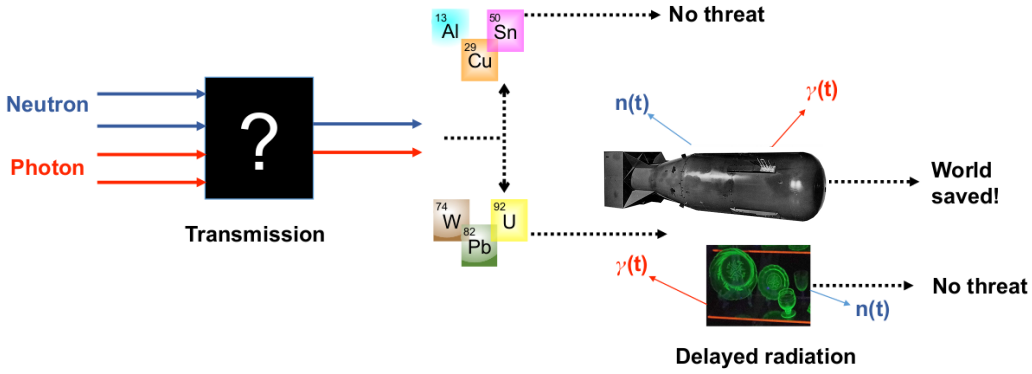

Figure 1.1: Overview of the steps in the presented methodology leading to the verification of the presence of fissionable material and uranium enrichment determination. The nuclear weapon shown in the diagram is a photograph of the uranium-based nuclear bomb ("Little Boy") dropped on the Japanese city of Hiroshima in 1945 during World War II.

1.2 Nuclear nonproliferation and security

The world has been engaged in an uphill battle to control the use and prevent the proliferation of atomic weapons from the fateful first use of atomic energy to bring World War II to a quicker end in 1945. The cries for a world without nuclear weapons can be traced as far back to 1953 in President Eisenhower's "Atoms for Peace" speech, when he drew attention to the "fearful atomic dilemma" and called for the eventual elimination of nuclear materials for military purposes [2]. Despite his efforts, since 1953 the num-

ber of states that possess nuclear capability has increased to a total of nine: the United States, the United Kingdom, France, Israel, Pakistan, India, Russia, China, and North Korea [3]. In the United States alone there is an estimated stockpile of 4,000 nuclear warheads and appears to be a shift towards a US military strategy that is more reliant on nuclear weapons [4]. Dr. Martin Luther King said, "The best way to solve a problem is to remove its cause." However, as long as nuclear weapons and the SNM needed to construct them exist and state policies support their use, the grave threat of nuclear proliferation and terrorism will remain.

The devastating attacks on September 11, 2001, have resulted in heightened security related to terrorist attacks and an escalated awareness surrounding the remote possibility of a terrorist-type nuclear attack. Despite the low probability, the effects of a nuclear terrorist attack anywhere in the world would have catastrophic consequences with reverberating international economic and psychological impact [5, 6]. The most challenging part of developing a nuclear weapon is obtaining the necessary nuclear material. By adequately securing existing SNM and inhibiting its illicit transport, the first step in building a nuclear weapon is made more difficult. The development and application of novel technologies and techniques that can be used to improve the ability to detect undeclared nuclear material and activities are needed to strengthen global nuclear nonproliferation capabilities.

A significant nonproliferation concern is the screening and interdiction of shielded SNM, which includes cargo containers, even smaller objects, and movement of illicit materials into and out of enrichment facilities [1, 7, 8]. Before the attack on the World Trade Center, approximately 2% of sea containers entering in the U.S. were scanned. Smuggling illicit cargo in normal shipping containers is not inconceivable, nor is it a new concept. Drug dealers, crime syndicates, and contraband traders have long been using sea-going containers as vehicles for illegal activity [9]. The potential impact caused by

smuggling illegal tobacco, however, pales in comparison when juxtaposed to a nuclear weapon.

Over several million ocean cargo containers land at U.S. seaports yearly [10–12]. In 2006, the United States passed the SAFE (Security and Accountability for Every) Port Act that deemed it necessary to scan 100% of these containers [13]. There has been much debate on whether this coverage of scanning is feasible or, for that matter, useful. Achieving 100% scanning raises serious practicality concerns based on the sheer volume of cargo passing through U.S. ports. The distribution of incoming containers is heavily concentrated at three ports, Los Angeles, Long Beach, and New York, at roughly 58% [10]. Taking a closer look at New York, 6,500 to 13,000 containers arrive daily [14]. Assuming an average number of containers per day and a 24-hour workday, the scanning rate needed for a 100% clearance would be 6.8 containers per minute. The high volume of containers that would need to be scanned to meet the requirements of the SAFE Port Act combined with the negative impact it would have on international commerce through delays and added costs makes the requirement too cumbersome to achieve and unlikely to be implemented under current circumstances. Although significant advances have been made, the current technology is just not capable of 100% clearance [11]. New and innovative detection capabilities and techniques are needed to help overcome the current limitations.

The ability to differentiate among different fissionable elements and isotopes is important for many nuclear non-proliferation applications. For example, material accounting in fuel canisters residing in enrichment facilities and verification of nuclear weapon dismantlement depends on measuring the isotopic fractions of ^{235}U and ^{238}U [15, 16]. Conventional nondestructive techniques for measuring uranium enrichment rely on the measurement of the ratio of emission of spontaneous, intrinsic gamma rays from ^{235}U and ^{238}U [17–19]. Because of the energy-dependent attenuation of the gamma-ray flux

incident on the detector from external shielding as well as self-shielding in the uranium, prior knowledge or assumptions are required for the geometry and characteristics of the sample and the shielding. New, more versatile enrichment determination techniques are required to meet the demanding nuclear nonproliferation and security environment.

1.3 Passive detection

"SNM" is defined by Title I of the Atomic Energy Act of 1954 as mainly plutonium or uranium enriched in the isotopes with atomic weight 233 or 235. Passive detection of SNM relies on spontaneous radioactive decay and results in a relatively small signal-to-background ratio. In many cases, passive measurements are easily confounded by shielding from common materials and compete with large, changing radioactive backgrounds [20]. Only highly penetrating radiation, such as neutrons and high-energy photons, is suitable for detecting SNM. Other radiation such as alpha- and beta-particles are easily stopped by the material itself or the air surrounding the material. The passive signatures of two fissile materials, weapons grade uranium (WGU) and weapons grade plutonium (WGPu) are considered, as these are the two primary materials used in United States and Russian warheads. WGU is uranium enriched >90% ^{235}U, and WGPu typically contains >93% ^{239}Pu.

Highly enriched uranium (HEU) spontaneously emits relatively intense but low-energy photons. Table 1.1 lists photon energies and intensities from the spontaneous radioactive decay of uranium isotopes of interest for nuclear security and nonproliferation applications. The intensity of neutrons emitted spontaneously from HEU is small due to the relatively low-rate of spontaneous fission. These neutrons are easily shielded by low-Z material. Table 1.2 shows neutron activities and spontaneous fission neutron yields for particular uranium isotopes of interest.

Table 1.1: Photon energies and activities of uranium isotopes for passive detection [21]

Isotope	Energy (keV)	Activity ($\frac{\gamma}{g-s}$)
^{234}U	120.9	9.35×10^4
^{235}U	143.8	8.40×10^3
	185.7	4.32×10^4
^{238}U	766.4	2.57×10^1
	1001.0	7.34×10^1

Table 1.2: Neutron activities and yields of uranium isotopes for passive detection [21].

Isotope	Activity ($\frac{n}{g-s}$)	Multiplicity (ν)
^{234}U	13,000	1.81
^{235}U	0.299	1.86
^{238}U	13.6	2.01×10^1

WGPu, conversely, spontaneously emits a large number of neutrons and high-energy photons from short-lived fission products and neutron capture events in the surrounding material [22]. Plutonium produces higher energy photons (>3 MeV) and a measurable yield of a 2.2-MeV photons from neutron capture on hydrogen in surrounding material. Table 1.3 lists important photon energies and activities associated with plutonium isotopes used for SNM detection.

Table 1.3: Photon energies and activities of plutonium isotopes for passive detection [21].

Isotope	Energy (keV)	Activity ($\frac{\gamma}{g-s}$)
^{238}Pu	152.7	5.90×10^6
	1.387	5.90×10^5
^{239}Pu	129.3	1.436×10^5
	413.7	3.416×10^4
^{240}Pu	45.2	3.80×10^6
	160.3	3.37×10^4
	642.5	1.044×10^3
^{241}Pu	148.6	7.15×10^6
	208.0	2.041×10^7

WGPu possesses a significant spontaneous fission rate resulting in emission of approximately 5.6×10^4 n/kg/s. These neutrons are mostly from isotopic impurities in the

material such as ^{238}Pu, ^{240}Pu, and ^{242}Pu. Table 1.4 shows the activities and neutron multiplicities for individual plutonium isotopes.

Table 1.4: Neutron activities and multiplicities of plutonium isotopes for passive detection [21].

Isotope	Activity ($\frac{n}{g-s}$)	Multiplicity (ν)
^{238}Pu	2.59×10^6	2.21
^{239}Pu	21.8	2.16
^{240}Pu	1.20×10^6	2.16
^{242}Pu	1.72×10^6	2.15

Table 1.5 lists photon rates on the surface of four representative nuclear weapon designs. The hypothetical designs use WGU and WGPu with either a tungsten or depleted uranium (DU) tamper device. Weapon composition and geometrical configuration are directly related to the emissions characteristics on the surface of the weapon [23]. Table 1.5 indicates that an HEU-based weapon with a tungsten tamper material exhibits the lowest rate of neutron emission of the four designs. For the HEU device using DU, the 1.001 MeV gamma ray is the most intense. This signature photon, however, is from the DU and not the HEU itself. As expected, the strongest neutron emitters are both the plutonium devices.

Table 1.5: Expected photon and neutron emission rates from four hypothetical nuclear weapons at the surface of the weapon, including gamma-ray energy most prevalent for detection.

Fissile Material	$\frac{n}{s}$	$\frac{\gamma}{s}$	γ energy (MeV)
12 kg WGU (W)	30	30	1.001
12 kg WGU (DU)	1,400	100,000	1.001
4 kg WGPu (W)	400,000	600	0.662
4 kg WGPu (DU)	400,000	60,000	1.001

The strengths of photon and neutron passive signatures are inversely proportional to the square of the distance from the source. Table 1.6 indicates the distances where the photon and neutron rates are approximately equal to natural background. For HEU-based

weapon with a tungsten tamper material, the radiation emission rate at the surface of the tamper is essentially at natural background level, making detection nearly impossible. Despite the higher intensities of radiation spontaneously emitted from WGPu, in the

Table 1.6: Distances from four hypothetical weapons where neutron and photon signatures are equal to background levels [23].

Fissile Material	neutron distance (m)	photon distance (m)
12 kg WGU (W)	0.2	0.4
12 kg WGU (DU)	1.5	3-20
4 kg WGPu (W)	25	0.6
4 kg WGPu (DU)	25	2-15

presence of significant shielding, passive detection of plutonium still proves challenging [22]. Taking into consideration the spontaneous signatures of SNM in particular behind shielding, passive detection is inadequate.

Intact nuclear weapons are mostly under heavy physical security making their acquisition difficult. A terrorist group has a greater possibility of obtaining the necessary material required to construct a crude nuclear device in smaller quantities. The theft of HEU is particularly troubling because of the straightforward manner in which a weapon could be built from this material and its global availability. The global stockpile of HEU is triple that of separated Pu at 1,600,000 kg; in some instances, HEU is located in research reactors in developing countries with no binding global standards governing how these materials should be secured [24]. Based on the spontaneous fission rates and accessibility, detecting kg quantities of HEU is, consequently, the most challenging, tangible threat to defend against.

1.4 Transmission Radiography for SNM detection

1.4.1 Dual-energy photon transmission radiography

Dual-energy transmission radiography has been a long-standing technique used to increase the contrast in radiographic images and/or determine the concentration of a particular element [25]. Since the 1950s, dichromatic transmission radiography has been used in a multitude of applications ranging from improving the quality of mammograms to finding illicit materials such as narcotics, explosives, weapons, and nuclear materials [26, 27]. Photons of different energies are used to perform material identification in dual-energy transmission radiography. The dependence of the mass attenuation coefficient on both the photon energy and the atomic number can be exploited to differentiate among materials. It is desirable for the photon energies to be adequately separated to ensure only one of the three main photon interactions (photoelectric effect, Compton scattering, and pair production) dominates at that particular energy. Each of these main processes scales differently with atomic number. This method represents an improvement over traditional monochromatic transmission radiography insofar as it provides greater contrast for materials that appear similar when using a single photon energy. This is because a thicker lower-Z material may result in as much attenuation as a thin high-Z material. Further discussion of the underlying physics of dual-energy transmission radiography is provided in Chapter 5.

Dual-energy radiography is widely used in x-ray scanners to determine elemental composition of luggage or cargo and relies on the difference in the Z-dependence of photoelectric and Compton scattering cross section. X-ray radiography has demonstrated the capability to readily identify high-Z materials which could indicate the presence of SNM [28]. Other dual-energy radiography methods rely on electron linear accelerators that produce broadband bremsstrahlung radiation [29]. The presence of low-energy pho-

tons in the bremsstrahlung spectrum significantly contributes to the imparted radiation dose and degrades the image quality [1, 30].

Prior work using the ^{11}B(d,nγ)^{12}C as an AI source for material identification has been conducted [31–33]. In this work, an ion-beam accelerator was used to generate highly energetic photons and probe various objects. Atomic numbers of various objects were inferred by dual-energy gamma transmission radiography. At two of the gamma-ray energies produced by this accelerator-driven source, the dominant photon interactions were Compton scattering and pair production, as opposed to photoelectric absorption and Compton scattering in common lower-energy bremsstrahlung sources. Despite accuracies to within 5–10% when determining Z_{eff} using dual-energy photon radiography, challenges remain in distinguishing high-Z materials such as SNM from non-SNM such as lead or tungsten [34].

1.4.2 Fast neutron/gamma-ray radiography

Much attention has been given to the use of fast neutron radiography to identify nuclear materials [35]. Typically, small portable neutron generators are employed to produce monoenergetic fast neutrons, which are then used to infer the composition of an object. In past work, two mono-energetic neutron sources were used to perform simple spectroscopic neutron radiography to perform crude geometric imaging and confirm the presence of fissile material [36]. Additionally, fast neutrons generated with larger particle accelerators were used to classify cargo containers based on their hydrogen content in cargo and gain insight into possible shielding that may disguise SNM signatures [37]. Other nontraditional probes such as high-energy protons [38] and muons [39–41] have also been used to perform radiography for certain material detection applications.

Single-particle-type probes by themselves are not universally applicable due their poor penetrability through certain materials, or extreme interaction probability (too small, or

too high). One method to overcome this limitation and increase the effectiveness of material probing is dual-particle transmission radiography. A less exploited radiography technique which combines fast neutron and photon radiography – fast neutron/gamma-ray radiography (FNGR) – is an example of a dual-particle probe and is based on the same principles as dual-energy photon radiography. Neutrons are highly penetrating through high-Z shielding, whereas photons easily pass through low-Z shielding, both providing useful information of the properties of the intervening material. Photon transmission can thus be augmented by neutron radiography, which provides a complementary signal. Implementation is particularly convenient if the nature of the AI source is such that it produces both photons and neutrons. The FNGR technique is different from dual-energy photon radiography in that, unlike photon attenuation, neutron attenuation does not scale monotonically with atomic number. Further, neutron attenuation depends not only on the atomic number, but also on the nucleon number (isotope).

1.5 Active Interrogation

1.5.1 Fundamentals of active interrogation

Passive detection relies on spontaneous radioactive decay, and in many instances can be easily masked by shielding from common materials. In contrast, AI uses external probing radiation to induce a higher signal intensity, providing a more viable method for SNM detection and nuclear material characterization. AI is defined as the use of ionizing radiation to cause nuclear reactions in the SNM and produce prompt and delayed neutrons and gamma rays. The neutrons and gamma rays produced from AI have a greater intensity and energy as compared to the passive detection signatures.

AI relies on inducing nuclear reactions in the material by exposing it to an external radiation source [42]. A material's probability of interaction is defined by its cross-

section. The higher the cross-section, the higher the rate of interaction and thus, higher intensity of detectable characteristic neutrons and gamma rays. The relationship among the reaction rate (R), number density (N), flux (ϕ), and the microscopic cross-section (σ) is

$$R = N\phi\sigma. \tag{1.1}$$

The most prevalent interrogation sources are neutrons and photons, which are usually produced by charged particle accelerators or radioisotope sources. The cross-sections are energy dependent and vary significantly for neutrons and photons. Figure 2.1 shows the fission cross-sections of uranium isotopes for photons and neutrons of various energies.

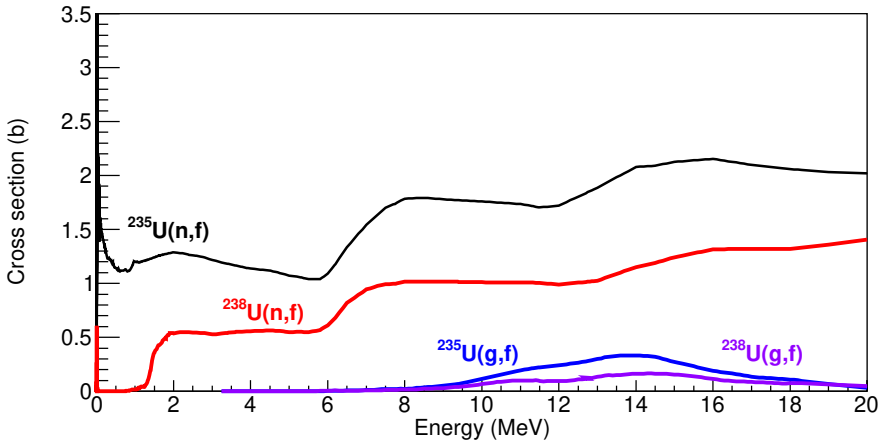

Figure 1.2: Neutron- and photon-induced fission cross-sections of two uranium isotopes.

The reaction rate for neutron-induced fission is higher over the full energy range of the incident particle. The photofission cross-section does not become significant until approximately 6 MeV, making AI via photons impractical below this energy. Even at its highest value in the range of 10 to 15 MeV, the σ for photofission is still approximately an order of magnitude lower compared to neutron-induced fission. Fission cross-sections for incident neutron energies at and below thermal energies are not displayed in Fig. 2.1. They are several orders of magnitude greater for ^{235}U when compared to ^{238}U [43].

However, thermally-induced fission is not discussed in this work due to the low penetration for thermal neutrons. The photofission signature can be supplemented by secondary photoneutrons emitted in the surrounding materials from (γ, n) reactions [42].

Signatures from fission also exhibit a time dependence and are characterized as either prompt or delayed. The neutrons that appear essentially instantaneously within 10^{-14} s are considered prompt, whereas any neutrons after 10^{-14} s are considered delayed. Prompt neutrons appear during the scission of the nucleus, while delayed neutrons originate from the decay of fission fragments and are emitted at a far lower rate as compared to prompt neutrons, with delayed to total neutron fractions ranging from 0.0064 to 0.0020 for fast-neutron induced fission of ^{235}U and ^{239}Pu, respectively [44].

The energy spectra of neutrons and gamma rays emitted from neutron-induced, photon-induced, and spontaneous fission are similar regarding their energy. For neutron-induced fission, the average number of neutrons per fission ($\bar{\nu}$) is larger in comparison to spontaneous fission and is a linear, slowly increasing function of incident neutron energy. For example, ^{239}Pu has a multiplicity of 2.6 neutrons per spontaneous fission, whereas the multiplicity for neutron-induced fission is 2.88 and 3.16 neutrons per fission for incident neutron energies of 0.025 eV and 2 MeV, respectively.

1.5.2 Ion-beam driven nuclear reactions as an AI source

Low-energy, ion-beam driven nuclear reactions can be utilized to produce high-energy neutrons and photons suitable for interrogation of heavily shielded fissile material. Reactions that carry a large positive Q-value allow the use of lower energy (and thus typically smaller and simpler) accelerators to create highly penetrating energetic photons and neutrons. By choosing proton- or deuteron-induced exothermic reactions with large Q-values, the minimum energy required to kinetically allow the reaction is governed by the Coulomb

barrier. The minimum energy required to overcome this threshold is approximately

$$E_c = 1.2\frac{Z_x Z_X}{A_x^{1/3} + A_X^{1/3}}. \tag{1.2}$$

Consider for example the $^{11}B(p,\gamma)^{12}C$ reaction. The Q value can be calculated from the mass differences,

$$Q = (m_x + m_X - m_y - m_Y)c^2. \tag{1.3}$$

and equals 15.95 MeV. Using Equation (1.2), the proton energy threshold for this reaction is 1.86 MeV. An AI system employing such a reaction as its source has the potential to be more cost effective, less complex, and result in a smaller footprint as compared to other more traditional high-energy AI sources [45].

1.5.3 Low-energy-threshold reaction candidates for AI

There are several reactions that produce either photons above the photo-fission energy threshold or neutrons that are viable for AI interrogation. As noted, these particles can be of high energy ($>$ 10 MeV) and used to penetrate dense cargo to perform radiography for material identification. In Ref. [46] many reactions were considered, including (p,γ), (p,$\alpha\gamma$), (d,nγ), and others. Four candidate targets (^{11}B, ^{7}Li, ^{19}F, and ^{15}N) were selected based on target atomic number, the Q-value of the reaction, and known gamma-ray energies from the resulting excited nuclei. Proton, deuteron, and triton beams were used to bombard the targets. Of primary interest in the work was the ^{11}B(d, nγ) reaction, which has a Q value of 13.7 MeV, an E_{th} of 1.63 MeV, and can excite the 15.1 MeV state of ^{12}C. The results of the study indicated that the ^{11}B(d, nγ) reaction was the strongest source of high-energy gamma rays that can be produced with low-energy p, d, and ^{3}He beams [46]. Extensive Monte Carlo simulation was performed in Ref. [47] examining the neutron and gamma-ray production from deuteron-based reactions as potential AI

sources. The reactions studied included the ^{11}B(d,n)^{12}C and ^{27}Al(d,n)^{28}Si.

This dissertation does not provide an exhaustive list of potential reactions, but lists a few that show good promise as AI sources. Due to the availability of specific accelerators for our experiments, this work focuses on two deuteron-based reactions both of which result in the excited state of ^{12}C along with other excited nuclei. While representative, the sources based on those two reactions do not necessarily fully explore the potential of low-energy threshold ion-beam driven nuclear reactions as practical AI sources.

1.6 Contributions of this work

Up to this point, this dissertation has introduced various methods to detect SNM including passive techniques, radiography, and AI. The focus of the research presented here has been to combine radiography and AI using a dual-particle, multiple-energy quasi-monoenergetic source. The source is based on accelerating deuterons into a boron-containing target. This dissertation establishes a detection methodology that starts with radiography of an unknown object and concludes with detection of SNM and enrichment determination for uranium that may be present in the object.

Elemental identification is performed for the first time by measuring the attenuation of neutrons and photons from an AI source based on deuterons incident on a boron target. FNGR presented in this work is more sensitive to changes in elemental composition as compared to dual-energy photon radiography. Such a system based on FNGR which employs several photon and neutron energies is likewise less vulnerable to shielding configurations designed to shield one type of particle or energy. A single, multi-particle, multiple-energy, mono-energetic source and a single detector type are used for the first time to perform simultaneous neutron and photon spectroscopic radiography. Figure 1.3 depicts a conceptual design of one important application – a cargo screening AI system

– where a multi-particle isotopic source could prove its utility.

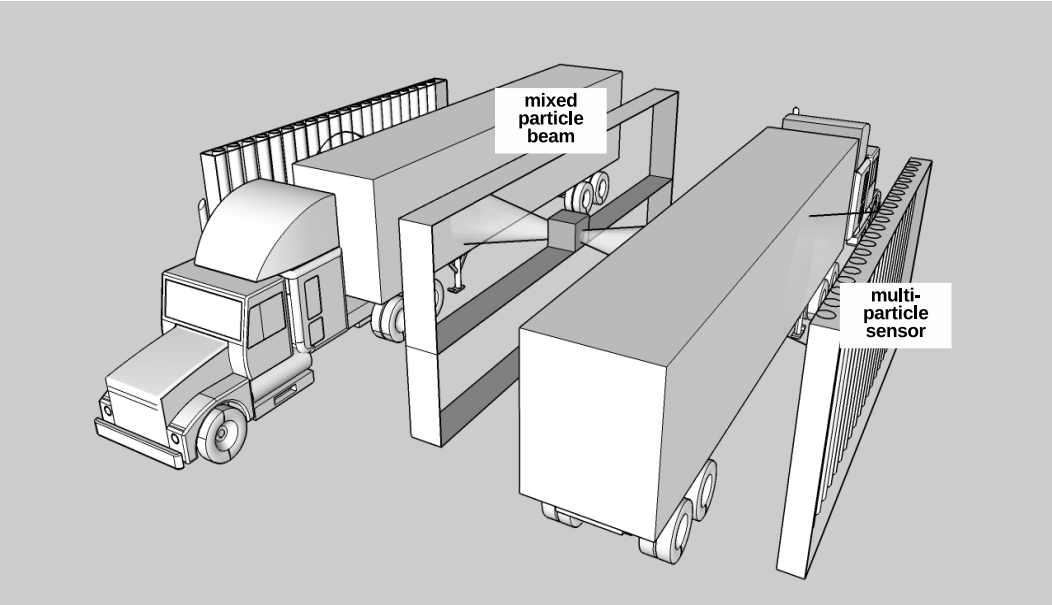

Figure 1.3: Depiction of potential cargo scanning system using an AI source. A single source may be used to implement simultaneous scanning of multiple cargo streams.

In this dissertation, fissionable material is detected using a custom-constructed capture-based scintillation neutron detector by measuring the time-dependent buildup and decay of delayed neutron emission from uranium. This work concentrates on observation of the delayed-neutron rate from uranium samples, but the method developed may be extended to plutonium or other fissionable materials. Although verifying the presence of fissile material by observing delayed neutrons is not a new technique, some gaps in prior work remain and are addressed here. Specifically, it is shown experimentally for the first time that not only the decay but also the time-dependent buildup of delayed neutron emission can be used to detect uranium and measure its enrichment. To that end, a novel method is presented to determine uranium enrichment by exploiting the differences in characteristic long-lived delayed neutron groups for two principal uranium isotopes in SNM, requiring no calibration standards.

1.7 Dissertation structure

While highly related, the remaining chapters in this dissertation can be treated as standalone contributions. The experiments discussed here were completed in three separate campaigns at three different facilities. Their combined strength arises from the fact that they provide complementary contributions to an overall AI methodology that may be used to identify the location of various materials (including high-Z material), detect SNM, and in the process even measure its isotopic enrichment. The successive chapters explain the steps necessary and applicable detectors that are suitable for this detection methodology. Although a system based on a low-energy ion-beam driven nuclear reaction source may offer these multiple functionalities, the technology presented can be used on an individual basis as well. Using the combined power of the presented techniques for specific applications such as cargo inspection could be most beneficial. If the application is focused on treaty verification techniques where uranium enrichment is the sole focus of the measurement, time-dependent delayed neutron measurements may be sufficient, and other AI sources (such as DD and DT neutron generators) may be more practical.

Chapter 2

Scintillation detectors for neutron/gamma-ray detection in an active interrogation system

In this chapter the relevant properties of the detectors used throughout the dissertation are discussed. The response of an organic liquid scintillator to high-energy neutrons and gamma rays is investigated. The method of *spectrum stripping* is presented as a way to reconstruct the incident neutron and gamma-ray energy spectra. Additionally, the time-of-flight (TOF) technique is discussed as a complementary means to measure the neutron energy. The operation of capture-based scintillation detectors is explained, including their potential advantages when used in specific nuclear nonproliferation and security applications. Lastly, the choice and the justification for the types of detectors used in this dissertation research are stated. This chapter includes edited portions of the 2017 publication in the journal Nuclear Instruments and Methods in Physics Research, Part A, *Response and Calibration of Organic Scintillators for Gamma-ray Spectroscopy up to 15-MeV Range* [48].

2.1 Organic Liquid Scintillators

There has been an increasing interest in the use of organic scintillators in nuclear safeguards and in nonproliferation applications to address a range of needs. The interest stems mostly from of their high-detection efficiency for fast neutrons, their fast timing properties, and their scalability to large sizes [16]. Applications of liquid scintillators in particle spectroscopy rely on the accuracy of their calculated response functions for monoenergetic photon and neutron sources and their agreement with calibration measurements.

Liquid scintillators are generally used to perform fast neutron spectroscopy, where pulse-shape analysis techniques are used to discriminate between neutrons and photons. Measuring the neutron TOF or employing unfolding algorithms are the most common methods used to extract the energy spectra of the incident neutrons in organic neutron scintillation detectors. Due to the partial energy deposition and different collision histories for neutrons of the same energy, organic liquid scintillators suffer from poorly resolved features in the light output distributions [49–51]. This lack of resolution increases the difficulty in spectral unfolding, making TOF often the preferred choice to measure neutron energy [52, 53].

While it is well-known that low-Z organic scintillators are also sensitive to photons and their response is nearly proportional, photon spectroscopy usually is not attempted due to low efficiency, resolution, and the absence of photopeak features in the spectrum. Instead, photon interactions with organic scintillators are usually rejected by pulse shape discrimination or the timestamp of a gamma interaction.

Although the presence of prominent full-energy deposition peaks is favored for photon spectroscopy, many common high-Z scintillators rely on expensive crystalline materials with slow decay timing characteristics, which can perform poorly in high-rate environments. Also, they can be costly to scale to large volumes of space, or may not be able

to differentiate between neutron and photon interactions. An organic liquid scintillator's fast rise-time and decay-time response, with the ability to adequately detect and identify both neutrons and photons make it a suitable choice for an AI system that requires the measurement of both types of particles in a high-rate environment.

Organic liquid scintillators are commonly used for measuring the fast neutron flux and energy spectrum. The low-effective atomic number of the constituent materials means that these detectors have a strong affinity for neutron interactions. With their high fast-neutron detection efficiency, these scintillators can be used in mixed radiation fields to perform neutron-photon spectroscopy through various unfolding techniques or TOF. In the same vein, due to their excellent neutron/photon discrimination combined with their fast response compared to a more traditional gamma-ray detector such as NaI(Tl), organic liquid scintillators may prove their usefulness for photon spectroscopy in high radiation fields as well.

2.1.1 Light output response

In an organic scintillator, the light output is strongly dependent on the type of recoil charged particle produced in the interaction. Neutrons are detected predominately through proton recoils, while energetic gamma rays are detected through electron recoils produced primarily by Compton scattering or pair production. The scintillation light output of organic scintillators has been described by the Birks' formula:

$$dL/dx = \frac{S\ dE/dx}{1 + kB\ dE/dx}, \tag{2.1}$$

where dL/dx is the energy emitted as light per unit length, S is the absolute scintillation efficiency, dE/dx is deposited energy per unit length in the form of ionized and excited particles, k is a constant related to the light quenching of the material, and B is a

constant [54]. As a result of light quenching, the ratio between the deposited energy and the emitted scintillation light is not the same for particles with different stopping powers, dE/dx. The response of organic scintillators also displays nonlinearities for both electrons and heavy charged particles (HCPs), which is most apparent at lower energies, i.e. below ∼125 keV for electrons and above slightly higher energies for HCPs [54, 55]. The response of organic scintillators to electrons above 125 keV is fairly linear and is used to scale the detector output to light output in *electron equivalent* units [56, 57]. The term *electron equivalent* (ee) is introduced to describe the light yield on a absolute basis and is defined as the amount of light that would produced by an electron of that energy. However, because of the quenching process for heavier charged particles, such as recoil protons, generation of certain amount of scintillation light requires a particle energy that greatly exceed the electron equivalent energy.

The shape of the light output spectrum in low-Z, organic scintillators is dependent on the energy of the incident particle. The Compton scattering process for photons remains the dominant interaction process in the energy range of 0.5–20 MeV, with the pair production process being the second highest contributor, becoming energetically possible above approximately 1 MeV. The contribution of the photoelectric effect to the interaction rate is considerably lower than both the Compton scattering and the pair production and can be considered negligible for low-Z materials. Figure 2.1 shows the calculated linear attenuation coefficients for the three primary photon interactions in the energy range of 0.5–20 MeV for the EJ-309 ($C_{4.35}H_{5.43}$) liquid scintillator [58].

Elastic scattering on hydrogen is the dominant process for neutron interactions in an organic liquid scintillator that contributes to the light output spectrum. An incident neutron can deposit anywhere from 0 to 100% its energy to the hydrogen nucleus producing a recoiling proton. Additionally, neutrons can scatter off a carbon nucleus, where the incident neutron can then lose anywhere from 0 to 28% of its energy. Figure 2.2

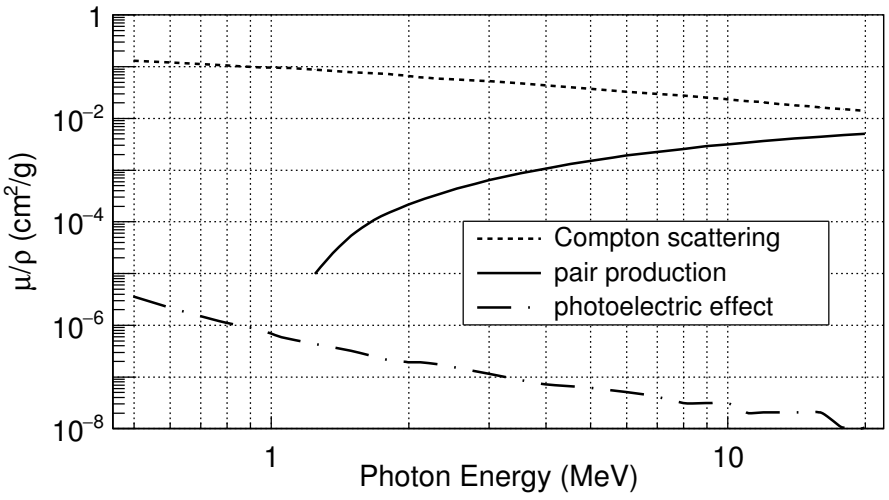

Figure 2.1: Linear attenuation coefficients of the three primary photon interactions for an EJ-309 ($C_{4.35}H_{5.43}$) liquid scintillator [58].

shows the microscopic cross-sections for elastic scattering of a neutron with hydrogen and carbon nuclei. Despite having a comparable or slightly higher interaction probability for neutron energies ranging from 1 to 20 MeV, recoiling carbon nuclei contribute less to the light output spectrum as a consequence of a decreased scintillation efficiency (equation 2.1) from a higher dE/dx and a lower-average energy for the recoiling carbon nuclei. Collision histories and the amount of energy deposited vary for incident neutrons of the same energy. This variability gives rise to a broad distribution of light output even for a monoenergetic neutron source.

2.1.2 Particle identification

Organic scintillators are comprised of aromatic hydrocarbons and have scintillation rise and decay times on the order of a few ns. The scintillation light relies on the transitions made by "free" electrons in the molecules that occupy the π molecular orbital. Ionizing radiation produces charged particles that excite the electronic and vibrational modes of the scintillator molecule, producing singlet and triplet states.

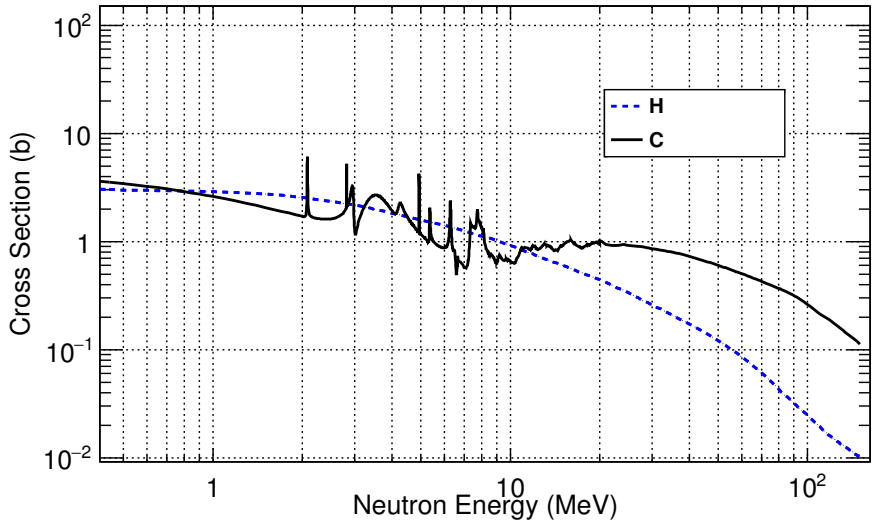

Figure 2.2: Microscopic cross-section for elastic scattering of a neutron on hydrogen and carbon [59].

The scintillation light is made up of two primary components – prompt and delayed. The singlet excitations decay quickly and contribute to the prompt component of the resulting emission (prompt fluorescence), while the delayed emission from triplet states proceeds primarily through inter-system crossing (delayed fluorescence) [55]. The fraction of light that appears in the delayed component is attributed to the fraction of triplet states produced, which is dependent on the recoil particle type and scintillator material. The process of pulse-shape discrimination (PSD) exploits this difference between the fast and slow components to identify the type of incident radiation (neutron or photon). Figure 2.3 shows a typical pulse shape from a neutron and photon event recorded from an organic scintillator. It is readily apparent through visual inspection of the two different pulses that the neutron pulse shows greater light output at later times.

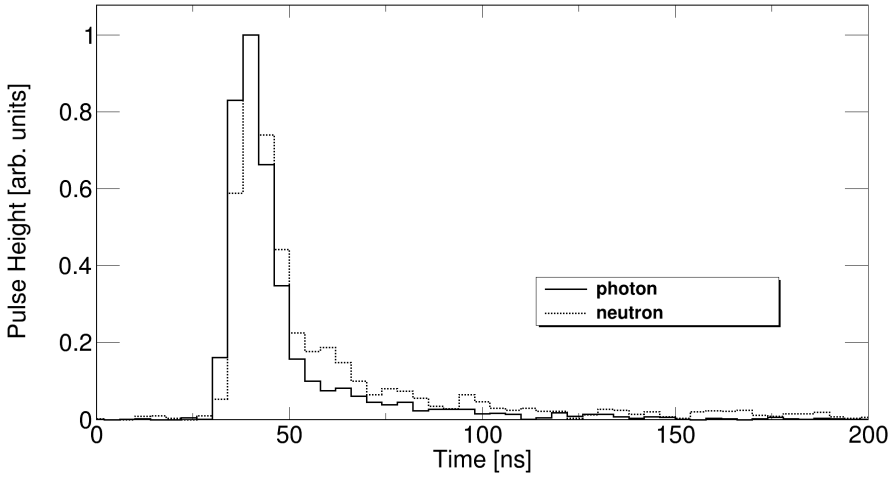

Figure 2.3: Representative pulse shapes from a neutron and photon event in a liquid scintillator.

2.1.3 Particle spectroscopy

Spectrum stripping

If the incident photon spectrum consists of several discrete, sufficiently separated energies, a spectroscopy technique known as *spectrum stripping* can be used. The response function for each of the expected photon energies can be simulated using a particle transport Monte Carlo code or by direct measurement using calibration sources. The response function for the highest expected energy is then fit to the high end of the measured spectrum. The fit response function is then "*stripped*" back by subtracting the response function from the measured spectrum. Now, the high end of the subtracted spectrum is solely due to the next highest energy. The subsequent anticipated energies are then fit in descending order until the entire recorded spectrum is accounted for. The relative intensities of each of the fit response functions give the intensity and light output spectrum of the photons detected. This process applies to both neutrons and photons if spectra are monoenergetic or multiple-monoenergetic, well-distributed, and the appropriate response functions are known or can be calculated [60].

Neutron time-of-flight (TOF)

An alternative method to determine neutron energy is by measuring its TOF. The neutron energy, E_n, is calculated from:

$$E_n = mv^2/2,\ v \lesssim 0.1c \text{ or} \tag{2.2}$$

$$E_n = \frac{mc^2}{\sqrt{1 - v^2/c^2}},\ v \gtrsim 0.1c \tag{2.3}$$

where m is the mass of a neutron, v is the neutron's velocity ($v = L/TOF$ with L being the distance from the origin of the neutron to the detector), and c is the speed of light.

2.2 Composite neutron scintillation detectors based on the ^{6}Li(n,α) reaction

Neutrons, being neutral particles, are detected by producing reaction-induced charged particles, for example by recoil or in nuclear capture reactions. A scintillator may contain a capture agent such as ^{6}Li , ^{10}B, ^{157}Gd , or ^{3}He, that exhibits large neutron interaction probability at low energy and produces a detectable reaction product. Due to the characteristic $1/v$ dependence of these isotope's nuclear reaction cross-sections, a hydrogenous material can first be used to moderate neutrons, thereby increasing the detection efficiency for fast neutrons.

Considerable work with loading neutron-sensitive material into scintillators in both homogeneous and heterogeneous configurations has been done [51, 61–64]. Homogeneous designs come in either solid-state or liquid form, and isotopes with large neutron interaction cross-sections are chemically loaded into another material to achieve a uniform distribution throughout the detector volume [51]. Heterogeneous or composite designs,

such as those in Refs. [65–67], are comprised of different materials that are not chemically combined and can be anisotropic or isotropic.

A heterogeneous composite detector combines scintillation materials with different scintillation properties. By exploiting the variations in decay time constants, fluorescence, cross-sections for varying particle types, and ranges of charged particles, neutron-photon discrimination is possible in materials that do not otherwise intrinsically possess this capability. Composite detectors that rely on neutron capture on ^{6}Li are accompanied with a relatively large Q-value (4.8 MeV), resulting in a high scintillation light yield, which uniquely identifies a neutron capture event. Thermal neutron capture on ^{6}Li produces two heavy charged particles:

$$^{6}\mathrm{Li} + \mathrm{n} \rightarrow {}^{4}\mathrm{He}\ (2.05\ \mathrm{MeV}) + {}^{3}\mathrm{H}\ (2.73\ \mathrm{MeV}). \tag{2.4}$$

^{6}Li-based heterogeneous composite detectors can distinguish neutron from photon events in two dimensions, light output and pulse shape. Composite detectors demonstrate their value in high-rate environments such as seen in AI systems, where high discrimination power is a necessity. Detectors based on capture reactions have essentially no low-energy threshold for neutron detection. Detectors based on capture reactions have essentially no low-energy threshold for neutron detection. Figure 2.4 shows the energy-dependent neutron capture cross section on ^{6}Li, exhibiting a characteristic $1/v$ behavior. Although a neutron can undergo capture on ^{6}Li at any energy, the probability of capture increases rapidly with the reduction of neutron energy [68]. The average energy of a delayed neutron from fission is on order of a few hundreds of keV. This makes capture-based detectors, with an appropriate amount of hydrogenous scintillator for neutron moderation, highly suitable for such a measurement with reasonable detection efficiency.

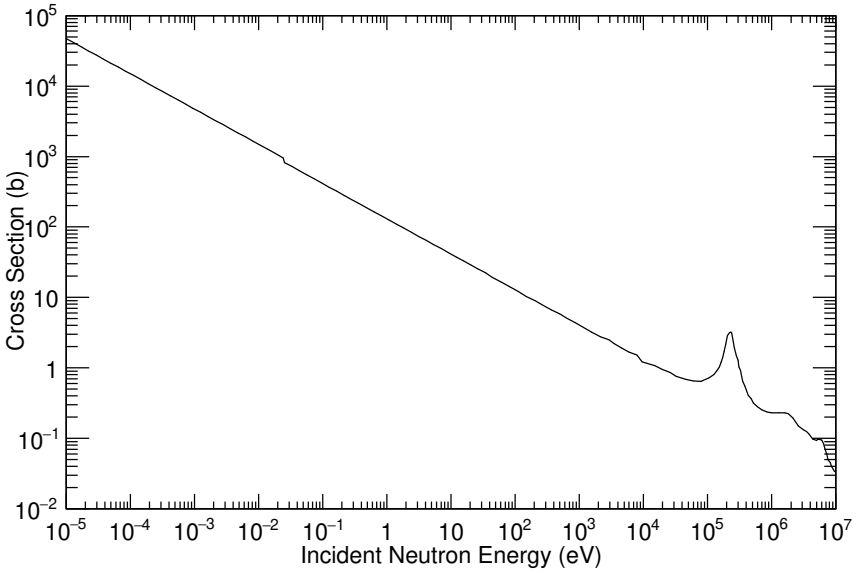

Figure 2.4: ^{6}Li cross-section as a function of incident neutron energy [68].

2.3 Detectors selected for this work

Two categories of experiments – neutron/gamma-ray radiography and the detection of delayed neutrons from fission – are discussed in this dissertation. The spectroscopic transmission radiography required modest energy resolution since the gamma rays produced in our deuteron-based nuclear reactions had discrete, well-separated energies. The high-event rate in our AI environment demanded a detector with a fast response time. Although two types of detectors designed explicitly to measure neutrons or photons could have been used, a more straightforward approach is taken, where one type of detector that was capable of effectively detecting both types of particles is employed. A 3-inch diameter, 3-inch tall cylindrical EJ-309 organic liquid scintillator manufactured by Eljen Technology is used for the neutron and gamma-ray radiography experiments [69]. This hydrocarbon-based scintillator can adequately detect and separate neutrons from photos and possesses sufficient energy resolution for detecting gamma rays in this environment.

Liquid scintillators exhibit relatively high efficiency for fast neutrons, but their abil-

ity to distinguish between neutrons and photons is diminished at lower energies (on the order of 100 keVee $\sim$ 1 MeV neutron energy or less [50]). Delayed neutrons are on order of several hundreds of keV, making delayed neutron detection more challenging with organic liquids. The detector used for the delayed neutron measurements was a custom-built heterogeneous composite scintillator coupled to an appropriate photomultiplier tube [67]. Capture-based detectors can detect lower neutron energies compared to traditional recoil-based organic scintillators due to their zero threshold. When accompanied by moderating material, these types of detectors are effective for both fast and slow (including thermal) neutron detection. Characteristics of the composite detector used in the present experiments could provide benefits for certain applications, such as the detection and spectroscopy of the relatively low energy delayed neutrons from fission in a high mixed radiation field, where sensitivity to low energy neutrons and a good particle discrimination are necessary.

A custom cylindrical detector was constructed from enriched ^{6}Li scintillating glass inside a matrix of scintillating polyvinyl toluene (PVT). The detector consists of an array of 1×1×7.6 cm^3 GS20 lithium glass square rods, and the PVT matrix has a height and diameter of 12.7 cm. The glass rods are centered in the PVT matrix. The lithium in the GS20 glass is enriched to approximately 95% in ^{6}Li and serves as the neutron capture material; the total lithium content in the glass is 6.6%. Figure 2.5 shows a photograph of the detector and a `Geant4` [70] rendering of the side and top of the detector.

Neutrons incident onto the detector typically undergo thermalization in the PVT and are subsequently captured in the lithium-doped glass. A neutron at thermal energies (0.025 eV) has a mean free path approximately 230 µm in the glass. This distance is smaller than the transverse dimensions of the rod making neutron capture highly likely. These neutron capture events can be easily distinguished from events that take occur in the PVT due to unique response that results from both the Q-value of the capture

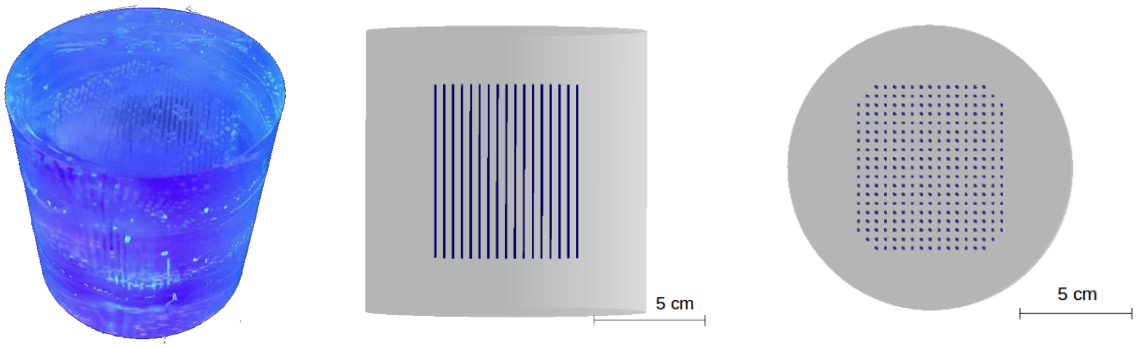

(a) (b) (c)

Figure 2.5: Photograph of the (a) composite neutron detector and the geometry as defined in `Geant4` simulation: (b) side and (c) top view.

reaction and different scintillation properties between the PVT and glass.

The heavy-charged particles produced from neutron capture on ^{6}Li (equation 2.4) have ranges on the order of tens of µm and typically deposit their full energy in the glass [66, 71]. In contrast, the typical range of an energetic electron produced by an interaction of a photon with the composite detector dramatically exceeds the transverse dimensions of the glass rod. Since the glass composes a comparatively small fraction of the detector mass, the electrons deposit their energy primarily in the PVT and can be readily distinguished by their pulse shape. Similar to photons, the neutron-induced nuclear recoils deposit their energy mainly in the PVT and are identified based on their pulse shape and subsequent neutron-capture event. A detailed description of the fabrication process and the specifications of the individual materials of the detector has been presented in Ref. [67]. Additionally, a full description of the underlying physics that occur in a lithium-based heterogeneous composite is found in Ref. [72].

Chapter 3

High-energy photon and neutron spectroscopy using an organic liquid scintillator

In this chapter, the characterization of the EJ-309 liquid scintillator used for many of the experiments conducted is discussed. In a broader context, this chapter presents a versatile calibration methodology that can be readily applied to organic scintillators over a wide neutron and photon energy range (approximately 0.5–20 MeV). The methodology is based on the identification of multiple features in the light output spectrum that can be attributed to the varying contributions of the two dominant radiation interaction mechanisms. The calibration method is applied to the EJ-309 organic liquid scintillator [69] and enables accurate high-energy photon spectroscopy in this material which is not traditionally used for this purpose. This method is used for the work described in the subsequent chapters, specifically in experiments related to the FNGR method. The characterization of the capture-based neutron detector used in this research is presented in chapter 6. This chapter includes edited portions of the 2017 publication in the journal Nuclear Instruments and Methods in Physics Research, Part A, *Response and Calibration of Organic Scintillators for Gamma-ray Spectroscopy up to 15-MeV Range* [48].

3.1 Simulation

Organic scintillators have been extensively studied by modeling in the `Geant4` framework, and their response to monoenergetic neutron and photon sources has been experimentally characterized [73–76]. To an even further extent, Monte Carlo N-Particle Transport Code (`MCNP`), specifically $\texttt{MCNP} - \texttt{PoliMi}$ [77], has been widely used to model particle responses in organic scintillators [53, 78–80]. Typically custom post-processing codes are used to analyze the output of $\texttt{MCNP} - \texttt{PoliMi}$, where the number of elastic collisions that occur on hydrogen and carbon nuclei are recorded [81]. There are two primary methods to obtain the detected light output spectrum from a Monte Carlo simulation; the first employs a complete simulation of the time-resolved production and transport of optical photons [76], while the second requires a post-processing step using the experimentally determined energy resolution and the correlated light-output functions. The latter technique is used in this work.

Monte Carlo simulations were performed in the `Geant4`.10.0.p4 framework, an object-oriented toolkit for simulating the passage of particles through matter [70]. The standard electromagnetic packaged `Geant4` physics list, *G4EmStandardPhysics*, was used to simulate interactions for various monoenergetic photon energies, accounting for both photon and lepton physics. A cylindrical scintillator was simulated with 7.62 cm diameter and height and surrounded by air. The direction of a particle fan beam was set such that the zenith and azimuth angles were equal to the detector's height and diameter at its center plane. The elemental ratio of hydrogen to carbon for the simulated detector was 1.25, which is equivalent to the organic liquid EJ-309 [69]. A large number of particle histories were examined to observe the effect on the spectral shape of the post-processed light output spectra.

3.2 Materials and methods

All gamma-ray measurements were conducted at the MIT's Bates Research and Engineering Center. A commercial EJ-309 liquid scintillator assembly was used for the measurements [69]. The dimensions of the detector were identical to those used in the simulation. The liquid scintillator was housed in an aluminum casing and was connected to a Hamamatsu R7724 photomultiplier tube.

Three photon energies were used to establish the resolution fitting parameters in the range of 0.5–4.4 MeV, originating from Pu-Be and ^{60}Co radioisotope sources and the activation of surrounding materials, which provides a strong 0.511 MeV photon flux. The detector was exposed to each of the photon energies for approximately 15 minutes to establish sufficient measurement statistics.

A radio-frequency quadrupole (RFQ) was then used to accelerate 3-MeV deuterons onto a 2-mm thick natural boron target, consisting of approximately 20% of ^{10}B, with the remainder being ^{11}B. The accelerator and facility described in Ref. [31] was also used in this experiment. The ^{11}B(d,nγ)^{12}C nuclear reaction produces several characteristic gamma rays, with two prominent energies at 4.4 MeV and 15.1 MeV [46]. A gamma-ray line is also readily observable at 0.511 MeV from the activation of the surrounding material induced by the accelerator. A competing reaction is ^{11}B(d,pγ)^{12}B, which yields two more gamma rays at 0.95 MeV and 1.67 MeV. All of these gamma rays, except for the 0.95 MeV gamma ray, were used to perform a calibration to electron-equivalent energy with just a single source over a broad energy range.

The detector was placed approximately 8 meters from the target. The accelerator was operated at 6 µA, with the photon production rate on order of 10^7 and 10^6 photons s^{-1} per µA at 4.4 and 15.1 MeV, respectively. The boron target was surrounded by borated polyethylene, lead, and concrete of various thicknesses. The mixed photon-neutron flux generated from the target was passed through two sets of concrete blocks and collimated

to a vertical fan beam with a width of about 5 cm.

In both the neutron and photon measurements, the detector was powered by a CAEN DT-5533 high-voltage power supply, and the photomultiplier tube anode light-pulse signals were digitized using a CAEN DT-5730 14-bit 500 MS/s desktop waveform digitizer. All data was processed in the ROOT framework [82]. A pulse-shape parameter (PSP) was calculated as

$$PSP = (Q_{long} - Q_{short})/Q_{long}. \tag{3.1}$$

CAEN's Digital-Pulse-Processing Pulse-Shape Discrimination (DPP PSD) Control Software was used to measure two preset scintillator light pulse integral regions, Q_{long} and Q_{short}, for each event. The waveform integration bounds were set to [t_s, t_s+64 ns] and [t_s, t_s+180 ns] for Q_{short} and Q_{long}, respectively, where t_s is the location of the start of the waveform (trigger position–gate offset). As a result of the choice of these bounds, the short integration region is fully contained within the long integration region.

Figure 4.7 shows the response of the detector in the PSP-light output parameter space when exposed to the accelerator source. A fiducial cut was placed at $PSP \approx 0.2$ to select the gamma interactions and a low light output cut was additionally applied at 50 keVee during post-processing. The response of the detector in the PSP-light output parameter space for the Pu-Be source is shown in Fig. 3.2 for comparison provides a much clearer display of the two separate neutron and gamma-ray PSP regions. The high event rate of the accelerator leads to significant pile up. The tight gamma-ray PSP selection window shown in Fig. 4.7 removes these invalid events along with other events lacking fidelity in the regions below and above the graphical cut.

The light output distribution for the EJ-309 response to the accelerator source is shown in Fig. 3.3 for the events located in the fiducial cut displayed in Fig. 4.7. The spectral features from the ^{11}B(d,nγ)^{12}C reaction to the interaction of a 15.1-MeV gamma ray emitted by the excited ^{12}C nucleus are easily distinguishable at the high end of the

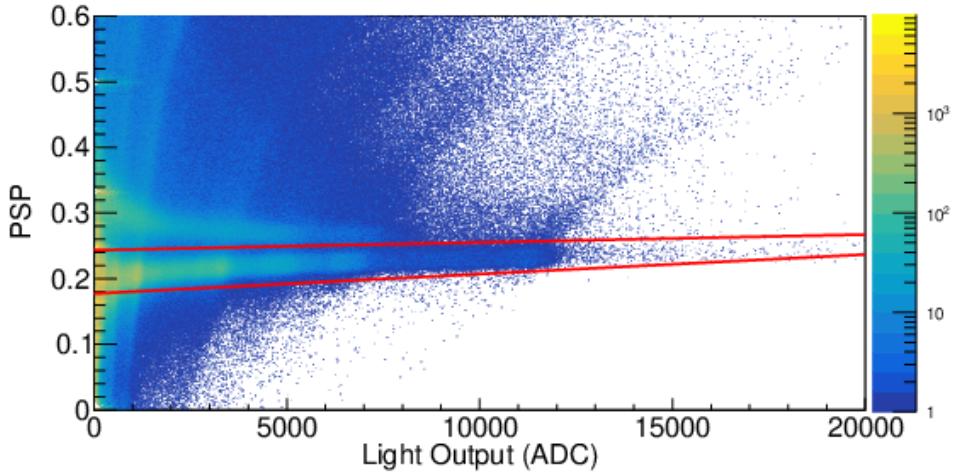

Figure 3.1: Response of the EJ-309 scintillation detector exposed to the accelerator source inducing the ^{11}B(d,nγ)^{12}C and the ^{11}B(d,pγ)^{12}B reaction with a fiducial cut on photon region shown in red.

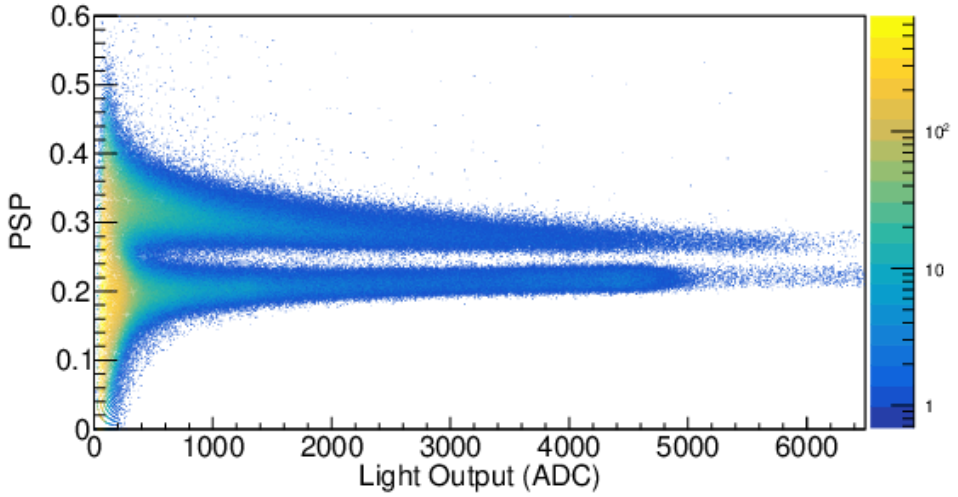

Figure 3.2: Response of the EJ-309 scintillation detector exposed to a PuBe source.

light output spectrum, and the presence of several other gamma-ray energies throughout the lower part of the spectrum is also visible.

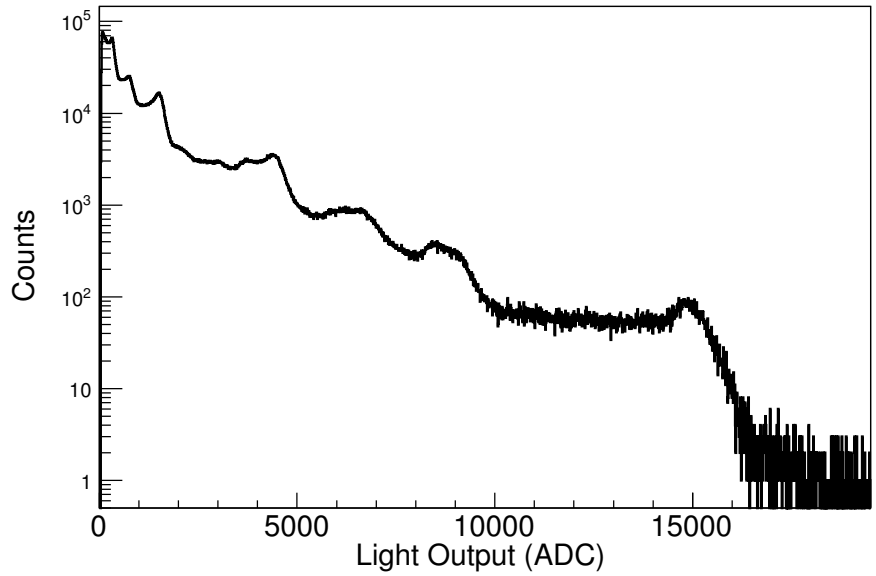

Figure 3.3: Photon spectrum of the AI source recorded with EJ-309 liquid scintillator.

3.3 Resolution parameter search

The results of the simulation were post-processed using a custom analysis code to predict the light-output distribution, L. The detector resolution, $\Delta L/L$, is described with a Gaussian broadening model, which was applied event-by-event:

$$\frac{\Delta L}{L} = \sqrt{\alpha^2 + \frac{\beta}{L} + \left(\frac{\gamma}{L}\right)^2}. \tag{3.2}$$

Equation (3.2) [83–85] is a well-established parameterization, where α is due to the position-dependent light transmission between the scintillator and the photocathode, while β accounts for the statistical nature of the photon production and attenuation of light in the scintillator and includes the quantum efficiency and electron amplification of the photomultiplier tube. Lastly, γ is the contribution of electronic noise of the photomultiplier tube [86].

The fit coefficients (α, β, and γ) are determined using an iterative process. First, an

initial value is selected for each of the coefficients. The simulated light-output spectrum is then calculated by convolving the resolution function in Eq. (3.2) with the deposited energy spectrum on an event-by-event basis. Both the experimental and simulated light-output spectra are then normalized to their maxima at the high end of their respective light-output distributions. The range of the simulated response to 4.4-MeV photons where the maximum is identified for instance is 3.7–5 MeVee. The range is selected to exclude the maximum value that occurs at the low end of all light output spectra. The values for the experimentally-measured light output spectra are identified in arbitrary units set by the data acquisition system, which we refer to as the ADC units. Following the normalization, the conversion of the experimental spectrum (in ADC units) to light output spectrum (in MeVee units) is performed by selecting the location of the peak in the simulated smeared spectrum and the location of the peak in the experimentally-measured spectrum. The units for the experimental spectrum are then converted to electron equivalent energy. A least-square value is calculated to compare the two light-output spectra, with the range of analysis limited to the high end of the light-output spectrum. For example, for the 4.4-MeV experimental-simulation comparison, the range was set to 3.7–5 MeVee.

To search over a broad parameter space, 100 values of α, β, and γ were tested for the detector responses to 0.511 MeV, 4.4 MeV, and ^{60}Co gamma rays separately. The values for each of the coefficients were initialized to 0.01 and were incremented by 0.01 over 100 steps. Each of the 10^6 parameter combinations were tested by the least-square criterion. The crude search resulted in parameter values all greater than 0.05 for each of the three gamma-ray sources, providing a more constrained starting point for α, β, and γ. A more precise parameter search was then performed by incrementing each of the coefficients by 0.001 over 50 steps, with α, β, and γ initialized to 0.05.

A range of the best α, β, and γ groups were recorded for each of the gamma-ray

sources. The α, β, and γ values for each of the groups were tested at the three different gamma energies. For each of the groups, the sum of the squares of the least-square values was calculated, and the minimum sum was selected to yield the best α, β, and γ combination. The values of 0.069, 0.058, and 0.069 were identified for α, β, and γ, respectively, to have the best agreement with the experimental data. The resolution as a function of light output over the range of 0.25–15 MeVee is shown in Fig 3.4 using the previously obtained α, β, and γ for values inserted into Eq. (3.2). Figure 3.5 shows

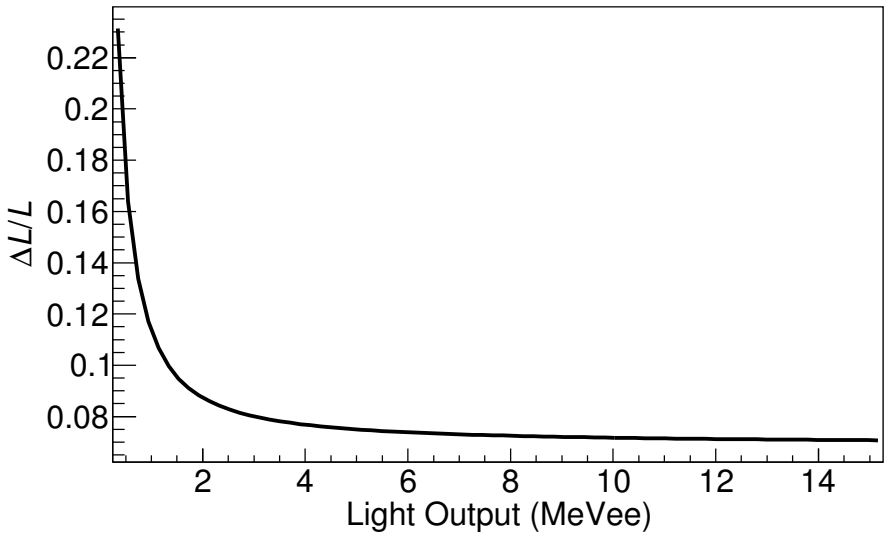

Figure 3.4: Resolution as a function of light output using the values of 0.069, 0.058, and 0.069 for α, β, and γ in Eq. (3.2).

the comparison of the experimental and simulated light output spectra using the best-fit values for α, β, and γ for 0.511-MeV, ^{60}Co, Pu-Be, and 15.1-MeV sources. The 15.1-MeV source is shown to illustrate the accuracy of the method despite not calculating the best-fit values of α, β, and γ at this energy.

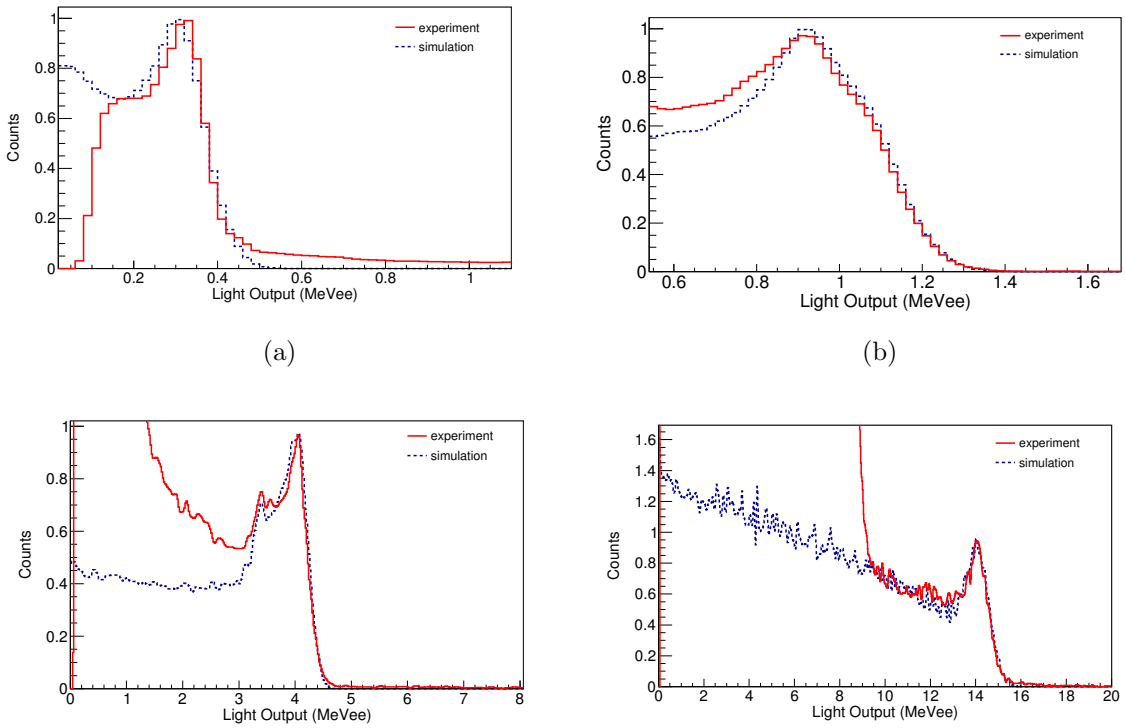

Figure 3.5: Experimental and simulated light output spectra with the optimal energy resolution fitting for (a) 0.511 MeV, (b) ^{60}Co, (c) Pu-Be, and (d) 15.1 MeV gamma ray sources.

3.4 Energy calibration

The common method for calibrating organic scintillators typically relies on the identification of the position of the Compton edge relative to the maximum number of counts at the high edge of the light output spectrum for a monoenergetic photon source. The methods vary slightly insofar as of the choice of the position corresponding to the Compton edge. In Ref. [87], a NE102A plastic scintillator has been examined, with the Compton edge point found at 4.8%±1.4% above the Compton edge maximum using a fast/slow coincidence system. Ref. [86] uses the comparison of a measured pulse height spectrum with Monte Carlo pulse height distributions folded with detector resolution to identify the position of the Compton edge in the NE213 (comparable to EJ-309 [69]) liquid scintillator. In that work it was found that the position of the Compton edge is greatly affected by detector size and photon energy due to multiple scattering events occurring in the detector. In Ref. [88], a calibration method analogous to the one described in Ref. [86] was used, finding a point for the Compton edge located at 83% of the Compton maximum for a 662 keV gamma ray. In Ref. [50] a ^{137}Cs source was used for calibration, with no clear indication of how the calibration point was identified on the light output distribution. Yet another method described in Ref. [89] provides a convenient graphical representation to identify the Compton edge position depending on the energy resolution.

In contrast to these methods, a technique can used where the measurement of the response to nearly monoenergetic electrons from Compton scattering events can be accomplished. In addition to the organic scintillator under characterization, the technique typically uses an additional high-purity germanium or NaI(Tl) detector placed at a specific angle relative to the incident gamma rays. By selecting coincident events, the Compton scattered electrons in the organic scintillator's light output spectra can be resolved and correlated to the deposited energy at the specific scattered gamma-ray angle [90]. If, however, experimental constraints prevent the use of a two detector system, the former

method is left to accomplish the calibration task.

Due to the poor energy resolution of organic scintillators, ranging from 8% for stilbene up to 25% for plastics, an accurate energy calibration is typically not required [89]. If photon spectroscopy is to be performed over a large energy range, e.g. up to high photon energies, these calibration procedures become cumbersome, and small calibration errors affect the accuracy of experimental results when using unfolding techniques. As the photon energy increases, the high-end region of the light output distribution from a monoenergetic (gamma) source becomes increasingly affected by the energy deposition of electrons and positrons from pair production, making the Compton edge feature in the light output spectra traditionally used for organic scintillator calibration more difficult to identify [91].

An energy calibration for a scintillator is typically performed by using clearly identifiable features in its light output spectrum. For example, in a NaI(Tl) detector, photopeaks are typically used with a linear fit performed to two or more points. Due to the low atomic number of the constituents of organic scintillators, the photopeaks are absent and other spectral features must be used.

Below 1.022 MeV, pair production is energetically impossible and the Compton edge can therefore be used for calibration. The location of a Compton edge is identified relative to the location of the peak at the high end of the light output response to a gamma ray. At energies >1.022 MeV, the light output spectrum becomes more complex due to the contribution of pair production. Although the Compton scattering continues to dominate the linear attenuation coefficient of the liquid scintillator up to 20 MeV, pair production interactions start to dominate the high end of the light output spectrum. The inclusion of these two concurrent processes in the analysis allows for a complete and well-understood set of prominent features in the spectrum to be used for calibration.

Figure 3.6(a) shows the simulated energy deposited and simulated light output spectra

convolved with energy resolution for a 4.4 MeV gamma ray. The Compton edge for a 4.4 MeV gamma ray can be identified in the deposited energy spectrum at its calculated value of 4.16 MeV. The Compton edge in the light-output spectrum can then be identified at the corresponding point in the deposited energy distribution. An intersection of the deposited energy spectrum and the light output spectrum occurs at the Compton edge energy, ∼4.16 MeV, which is ∼86% of the Compton maximum. Another discernible feature in the light output spectrum is the double escape peak at 3.38 MeV, which is easily identifiable at the intersection of the narrow peak in the energy deposited spectrum and the broadened smaller peak in the light output spectrum. Figure 3.6(b) shows the contributions to the light output spectrum for a 4.4 MeV gamma ray. The higher edge of the light output spectrum is dominated by Compton scattering interactions, which allows the same technique for selection of calibration used for points below 1 MeV.

Figure 3.7(a) shows the simulated energy deposited and light output spectra for 15.1-MeV gamma rays. The energy of the Compton edge for a 15.1-MeV photon is 14.85 MeV, but the Compton events are no longer the dominating contribution of light output at the high end of the light output spectrum, as seen in Figure 3.7(b). The greatest contribution to the broadened peak is the double escape from the pair production event, and the Compton edge cannot be discerned. The shift in the contributions to the high edge of the light output spectrum gives rise to an identifiable peak located at 14.1 MeV (15.1–1.022 MeV).

A fraction of bremsstrahlung deposits its energy in the detector and makes a significant contribution to the light output spectra for both 4.4- and 15.1-MeV photons, aiding in the in the resolution of the double escape peak from pair production. The two photons created during pair production typically escape, and the two energetic electrons lose some of their energy through bremsstrahlung, a fraction of which escapes from the detector. However, some of the bremsstrahlung photons undergo additional interactions

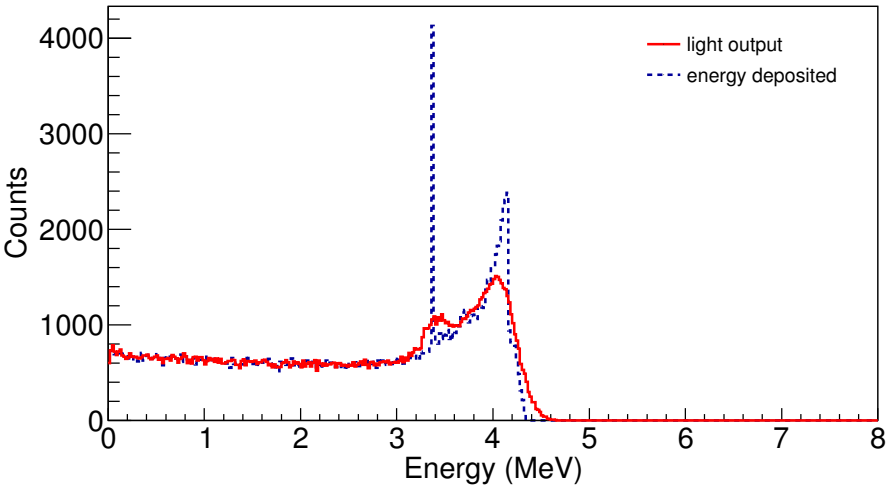

(a)

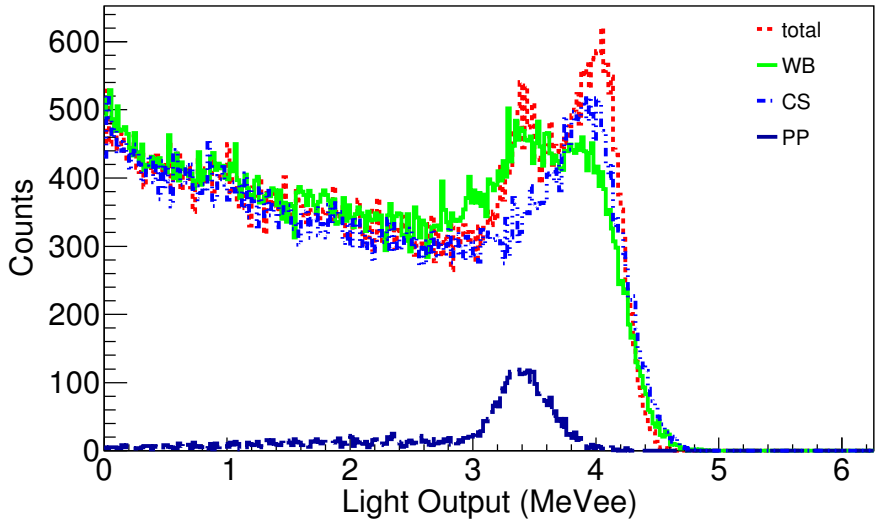

(b)

Figure 3.6: (a) Simulated deposited energy (blue) and light output (red) for a 4.4-MeV gamma ray; (b) relative contributions to the light output spectrum by the various processes in an EJ-309 detector. The processes displayed are Compton scattering (CS), pair production (PP), light output with the exception of light produced from bremsstrahlung (WB), and the total light output.

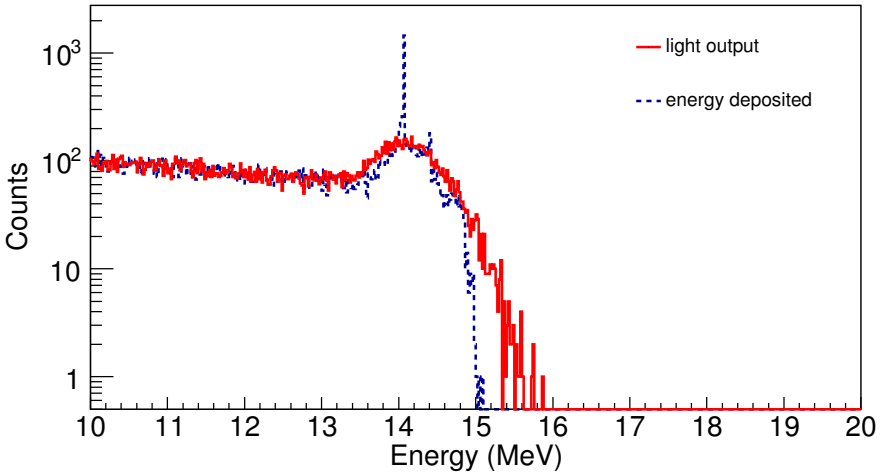

(a)

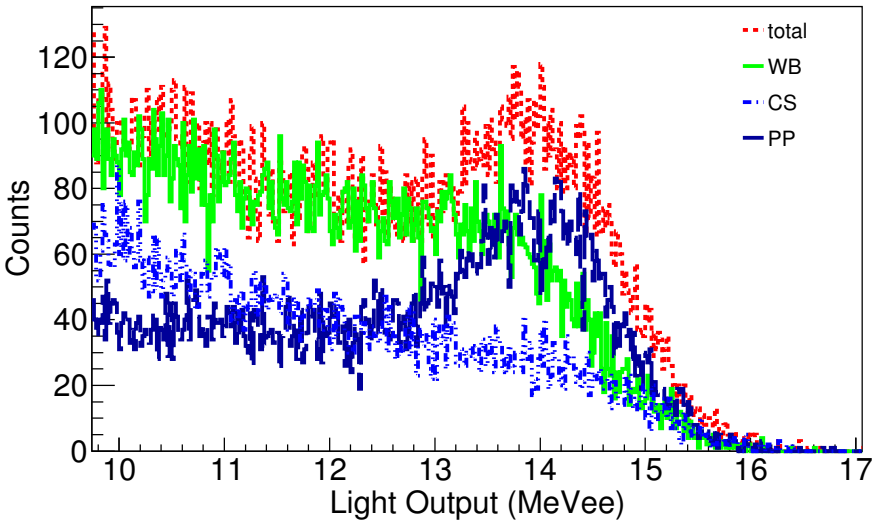

(b)

Figure 3.7: (a) Simulated deposited energy (blue) and light output (red) for a 15.1-MeV gamma ray; (b) contributions of various processes to the light output spectrum in an EJ-309 detector. The processes displayed are Compton scattering (CS), pair production (PP), light output with the exception of light produced from bremsstrahlung (WB), and the total light output.

in the detector volume and can lead to deposition of an energy equivalent of the double escape peak. This is shown in Figure 3.6(b) and 3.7(b) at 3.38 and 14.08 MeV for the respective incident gamma energies of 4.4 and 15.1 MeV. The importance of the contribution of bremsstrahlung becomes apparent by comparing the total light output from all photon processes to the light output when the energy redeposited from bremsstrahlung is excluded, as seen in Figure 3.6(b) and 3.7(b).

Two different linear calibration fits were tested for their agreement between the simulated and experimental light output spectra. The first calibration fit uses the Compton edge position at 86% of the peak at the edge of the light output spectrum for four different gamma ray energies, resulting from the ^{11}B(d,nγ)^{12}C and ^{11}B(d,pγ)^{12}B nuclear reactions and the 0.511 MeV annihilation gamma ray. The result of the fit is shown in Figure 3.8(a). The second calibration fit uses three calibration points corresponding to the locations of Compton edges used in the first fit, and adds two additional points at the position of the double escape peaks of the 4.4 and 15.1 MeV gamma rays. The result of the five-point fit is shown in Figure 3.8(b). Parameters $p0$ and $p1$ displayed in Fig. 3.8(a) and (b) follow the following linear relationship for conversion of ADC units to MeVee:

$$Light\ Output\ (\text{MeVee}) = p1 \times ADC + p0.. \tag{3.3}$$

Using the parameters from the three-point fit in Fig. 3.8(a) to convert the experimental spectrum in units of ADC to MeVee, the high-energy end of the gamma-ray spectrum from the ^{11}B(d,nγ)^{12}C reaction was compared to the simulated detector response to a 15.1-MeV gamma ray. The results of this comparison are shown in Figure 3.9. A clear difference is apparent in the shape of the light output spectrum near its end point, which could be due to Compton edge position selection and the lack of another calibration point at high energies. A Gaussian fit was performed with three different spectra on their peaks at the high end of the light output spectra. The mean light output for the simulated

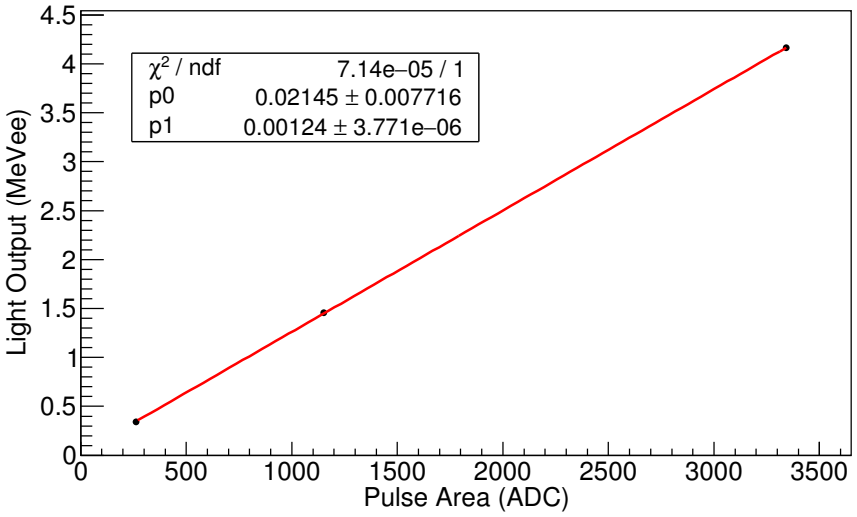

(a)

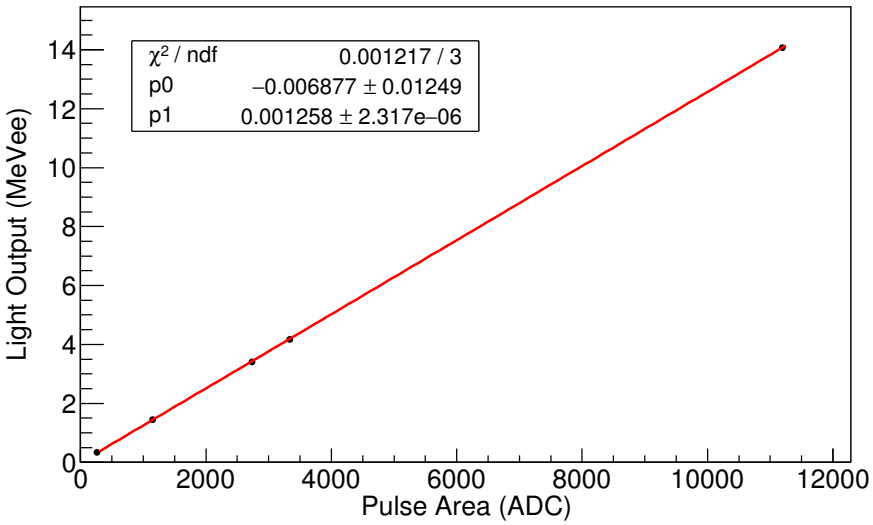

(b)

Figure 3.8: Linear calibration fits for (a) three-point fit using the Compton edge for 0.511-, 1.67-, and 4.4-MeV gamma rays; (b) five-point fit using the Compton edge for 0.511-, 1.67-, and 4.4-MeV gamma rays and the double escape peaks for 4.4- and 15.1-MeV gamma rays.

spectra yielded 14.1±0.05 MeVee. The three- and five-point calibrated spectra resulted in mean light outputs of 13.8±0.04 and 14.1±0.04 MeVee, respectively. The five-point calibration fit is in much better agreement compared to the three-point calibration fit, while the three-point calibrated spectra are not within 3σ of the expected result. The selection of the position of the Compton edge is affected by the resolution of the detector, which can lead to approximations that contribute to calibration shifts at higher energies. Using the three-point calibration, all of the lower energy fits are still in good agreement with simulation.

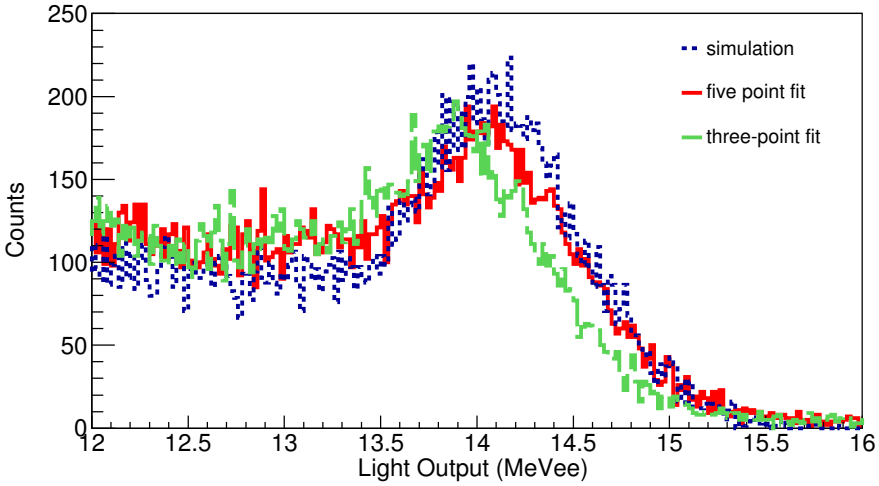

Figure 3.9: Comparison of simulated (blue) 15.1 MeV and high end of the ^{11}B(d,nγ)^{12}C experimental gamma-ray light output spectrum using the three-point calibration (green) and five-point calibration (red).

A similar comparison as the three-point fit was performed between the experimental and simulated light output distributions for a 15.1-MeV gamma ray using the parameters from the five-point fit in Fig. 3.8(b). The results of the comparison are shown in Fig. 3.9 for a side-by-side comparison with the three-point fit. With visual inspection alone, it is clear that the five-point fit represents a more accurate calibration method.

3.5 Discussion

A versatile iterative process for extrapolating resolution fitting parameters for an organic scintillator to high energies was developed and applied to the EJ-309 scintillator. Three different photon energies were used in the process, and a least-square test between experimental and simulated data was performed. An optimal combination of resolution fitting parameters for the EJ-309 liquid scintillator was determined. The methodology can be utilized for any organic scintillator where a well-parameterized resolution function can be applied, and a step-by-step procedure to perform this method is outlined Fig 3.10. The method does not require the measurement of the resolution at many photon energies to extract the resolution fit parameters, and could thus reduce the number of additional experiments that would otherwise be required.

Above 1.022 MeV, pair production starts competing with Compton scattering for a contribution to the light output spectrum. At higher energies, the light output spectrum develops additional features that can be resolved and used for a more robust calibration to electron equivalent energy. The feature that can be utilized is caused by the pair production process, where the double escape peak starts to appear at energies greater than 4 MeV. Simulated results in Fig. 3.11 show the percentage of interacting photons that undergo pair production as a function of energy. The simulated evolution of the pair production feature with increasing incident photon energy is shown in Fig. 3.12. By examining Fig. 3.12, one can see the double escape peak starts to be resolved around 4 MeV, where the pair production events begin to make an observable contribution to the light output spectrum. Eventually, as the photon energy increases, the contribution to the light output from pair production begins to dominate the spectral shape at the high end of the light output spectrum, compromising the ability to use Compton scattering features for calibration.

Two calibration fits were established for comparison of experimental data and simu-

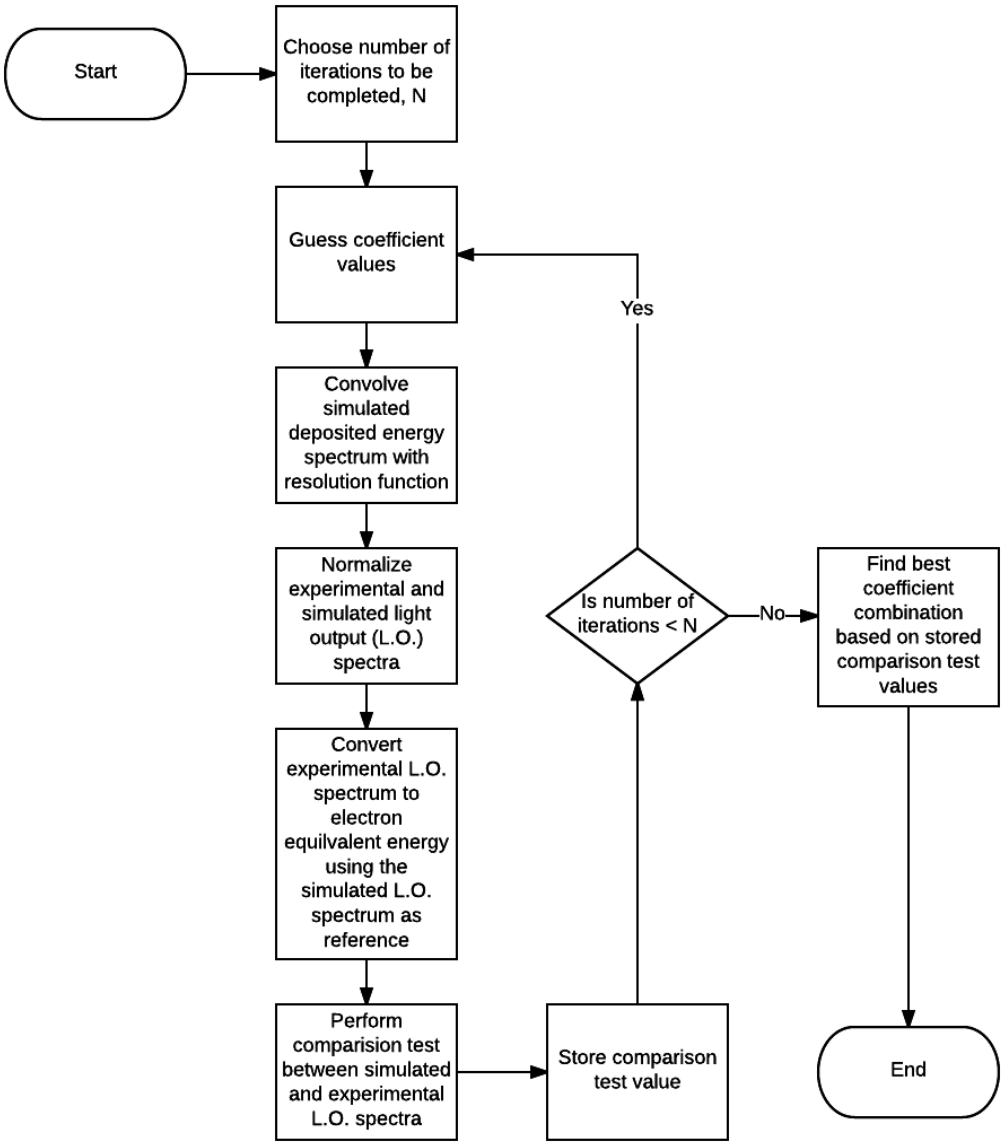

Figure 3.10: Flow chart describing the method to extract resolution parameters for an organic scintillator.

lations. A three-point linear fit was performed using the Compton edge at three different photon energies: 0.511, 1.67, and 4.4 MeV. Additionally, a five-point linear fit was performed using those same energies, as well as two points corresponding to the double escape peak of 4.4-MeV and 15.1-MeV gamma rays. A least-squares test was performed in the range of 13.5–16 MeVee, resulting in values of 1.23 and 0.49 for the three- and

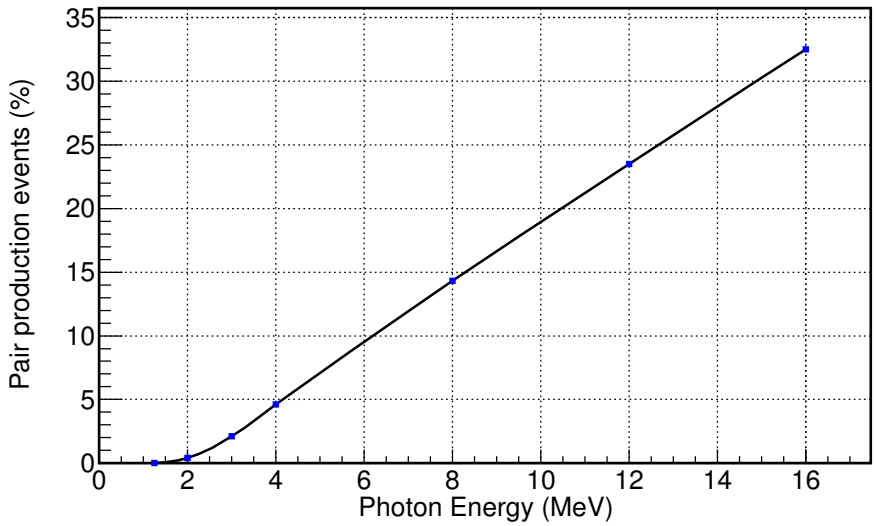

Figure 3.11: Percentage of photons that interact with the detector that undergo pair production.

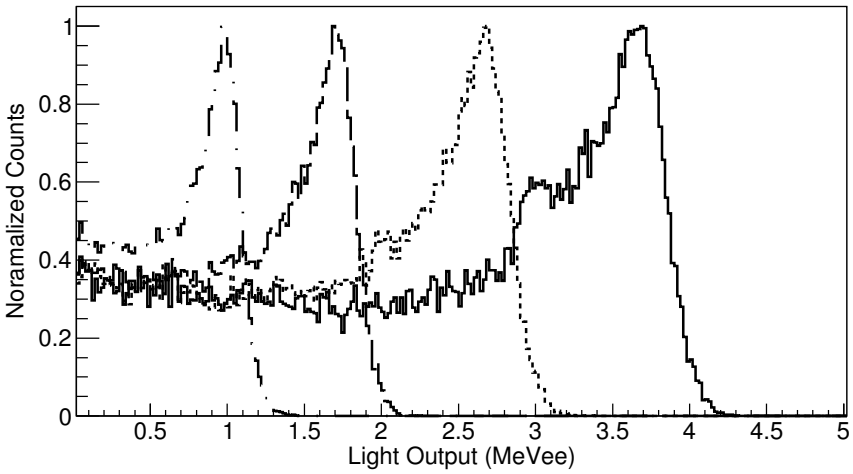

Figure 3.12: Light output spectra for 1, 2, 3, and 4 MeV photons from left to right, respectively.

five-point calibrations, respectively. Due to the poor resolution of organic scintillators, identification of the position of the Compton edge is often challenging. When easier to identify, features such as peaks can be used in addition to the Compton edge, yielding a more accurate calibration to electron equivalent energy. The ability to perform photon spectroscopy over a broad range of energies is heavily dependent on the accuracy of

the energy calibration. At high higher photon energies, the Compton edge is no longer identifiable and other points must be selected to improve the accuracy of the conversion. The five-point calibration presented here is adaptable and can also be applied to a broad range of organic scintillators to enable high-energy photon spectroscopy and was used to calibrate the liquid scintillators used in the remaining experiments discussed.

Chapter 4

Single-mode dual-energy transmission radiography

In this chapter, accelerator-based measurements conducted at the MIT Bates Research and Engineering Center are discussed. Here, *single-mode* refers to a single type of radiation used (photons); however, two photon energies are employed to perform dual-energy spectroscopic transmission radiography and determine the effective atomic number of several pure materials ranging from aluminum to uranium. 3-MeV deuterons were used to drive a multiple-particle AI source, and EJ-309 liquid scintillators were used to detect the transmission of gamma rays and neutrons. The accelerator target used to stop the deuterons was made of natural boron and produced a mixed neutron/gamma field. Two prominent gamma-ray energies are present, at 4.4 and 15.1 MeV. By measuring the attenuation of the gamma-ray beam at these two photon energies, moderate to large changes in atomic number among objects can be readily discerned. Despite this capability, dual-energy photon transmission radiography material identification provides relatively poor material discrimination between materials in the high Z-range ($Z \gtrsim 74$). The work presented in this chapter uses low-resolution liquid organic scintillation detectors for the first time to perform dual-energy photon radiography. Further, the material identifica-

tion approach uses a single AI source, single detector type imaging system based on the ^{11}B(d,nγ)^{12}C reaction.

4.1 Introduction

The intensity of photon radiation through matter follows a simple exponential attenuation law. Absorption removes the photon from the beam, while scattering reduces its energy and changes its emission angle. As a result, scattered radiation may not be detected, depending on the scattering angle and the solid angle covered by the detector. The probability of all interaction processes per atom depends on both the energy of the photon and the atomic number of the absorber. The total probability that an interaction occurs per unit path length is referred to as the total linear attenuation coefficient, μ , and is the sum of all coherent and incoherent interaction cross-sections.

$$\mu = \tau_{(photoelectric)} + \sigma_{(Compton)} + \kappa_{(pair)}. \tag{4.1}$$

Since the linear attenuation coefficient depends on density, it is convenient to define attenuation using the mass attenuation coefficient, μ/ρ.

The energy-dependent transmission (T) of photon radiation is described by the Beer-Lambert law,

$$T(E) = I/I_0 \ = \exp[-(\mu(E)/\rho)\kappa], \tag{4.2}$$

where I and I_0 is the measured intensity of the transmitted photons with and without the absorber present, respectively, and κ is the areal density of the absorber.

Different processes dominate photon interactions for material in specific energy regimes. Material identification using dual-energy photon transmission radiography exploits the dependence of the interaction cross section on the atomic number Z and photon energy.

Figure 4.1 shows the regions in which the three main photon interaction processes with matter dominate with the two separate photon energies, 4.4 and 15.1 MeV, selected for this work indicated with a dashed (red) line.

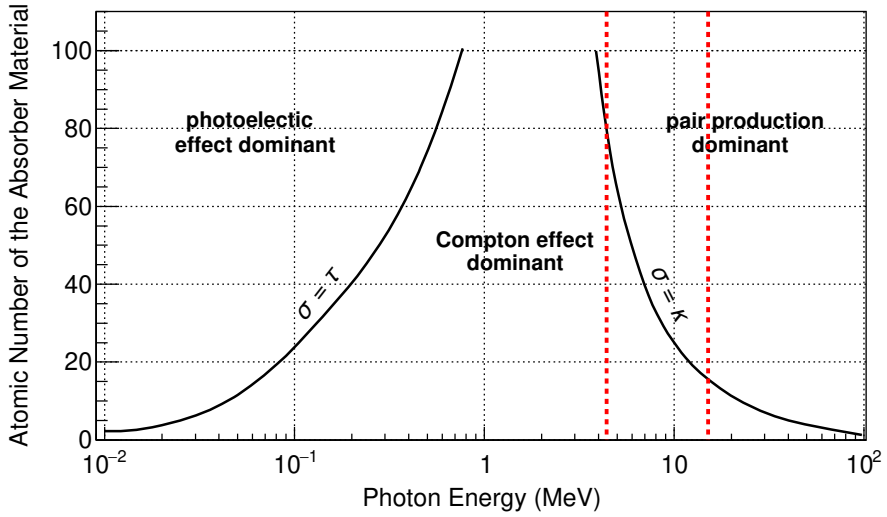

Figure 4.1: Relative importance of the three main interaction processes as a function of photon energy and atomic number of the absorber. The solid lines indicate where the processes on either side are equal. The dashed red lines indicate the two photon energies used for dual-energy (single-mode) radiography.

Interactions at 4.4 and 15.1 MeV are dominated by different mechanisms, which scale differently with Z. Figure 4.2 shows the energy dependent variation of the total attenuation coefficient for uranium, lead, iron, and aluminum. At 4.4 MeV, the dominant interaction process is Compton scattering($\sigma \propto Z$), whereas pair production ($\kappa \propto Z^2$) is the dominant process for most elements at 15.1 MeV. This varying Z-dependence between low- and high-Z ($Z > 74$) allows high-Z materials to be identified.

If transmission is measured at two energies ($E1$ and $E2$), one can write

$$R = \frac{\mu_1}{\mu_2} = \frac{\ln(T_{E1})}{\ln(T_{E2})}. \tag{4.3}$$

Here, R is the ratio of the mass attenuation coefficients (or attenuation coefficients) at

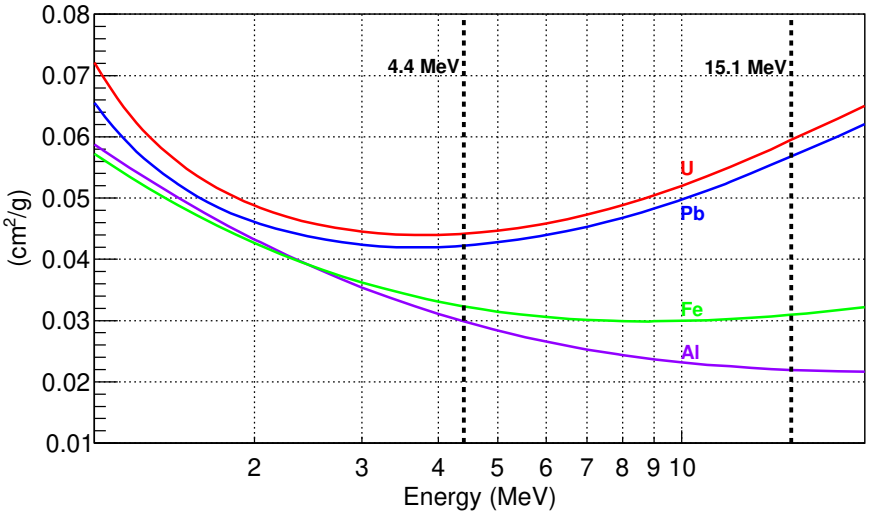

Figure 4.2: Energy dependent variation of the total attenuation coefficient for uranium (red), lead (blue), iron (green), and aluminum (purple) with two gamma-ray energies used for dual-energy transmission radiography

energies $E1$ and $E2$, which is specific to the material the photons traverse. Therefore, the ratio of the mass attenuation coefficients at two energies can be used to compare the experimentally measured quantity $\ln(T_{E1})/\ln(T_{E2})$.

If the ratio of attenuation of monoenergetic photons of 15.1 and 4.4 MeV are used as an example, a unique ratio of attenuation coefficients exists across the periodic table, as indicated by Fig. 4.3. For the case of broad-bremsstrahlung radiation with dual-energy boundaries, the aforementioned ratio becomes sensitive to areal density. In these cases, the ratio is no longer unique and is treated as a ratio of effective attenuation coefficients averaged over the bremsstrahlung spectra. The mass thickness is estimated from one of the bremsstrahlung spectra and a lookup table used to estimate Z [92].

If an an object is a combination of multiple pure elements or a mixture of elements, the object can be hypothetically considered as a pure element and represented by its effective atomic number ($Z_{effective}$). The transmission of a monoenergetic photon for an object or objects containing i components with mass attenuation coefficient, μ_i/ρ_i, and

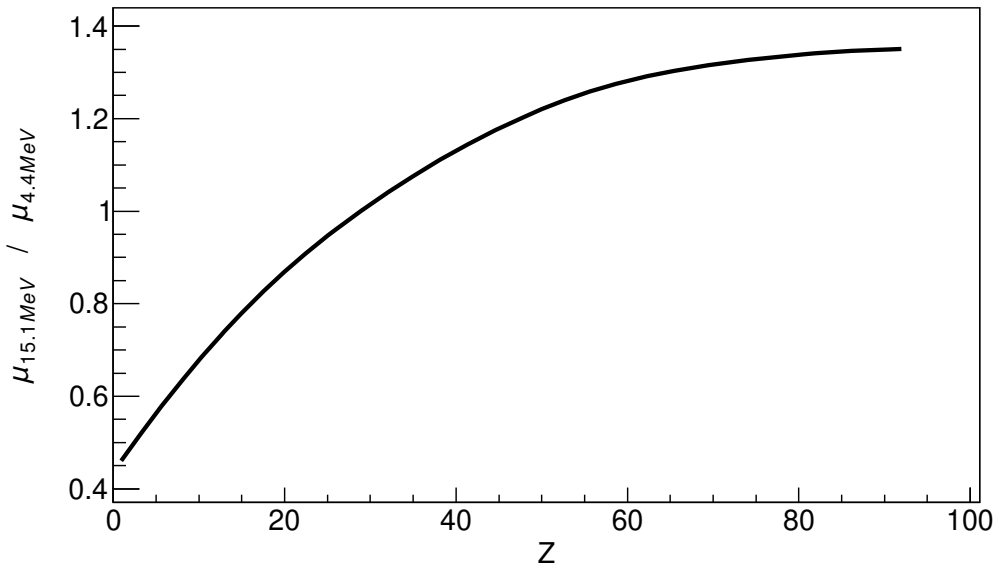

Figure 4.3: Ratio of 15.1 to 4.4 MeV attenuation coefficients [58]

areal density, κ_i, is written as

$$T = \Pi_i \exp(-\mu_i/\rho_i\kappa)_i = \exp(-\Sigma_i\mu_i/\rho_i\kappa_i) = \exp\left(-\left(\frac{\mu}{\rho}\right)_{eff}\kappa\right) \tag{4.4}$$

A deficiency of a simple two-energy approach for material identification is that it cannot easily distinguish a combination of elements from a pure material as it only determines $Z_{effective}$. Such is the case for detection of shielded SNM, where the SNM object may be shielded by a combination of high- and low-Z materials. The two-energy approach is also limited in its ability to distinguish between materials with similar attenuation coefficients as in distinguishing between lead and uranium. Techniques have been developed that attempt to overcome this limitation by using more than two photon energies and tomographic techniques [34, 93–95]. Such a technique could be employed here using other characteristic photon or neutron energies from the ^{11}B(d,nγ)^{12}C reaction and is the subject of chapter 5.

4.2 Materials and methods

Measurements were conducted at the MIT Research and Engineering Center and utilized 2- and 3-inch EJ-309 liquid scintillators. An Accsys Technologies DL-3 RFQ accelerator was used to accelerate deuterons to 3 MeV and direct them onto a thick natural-boron target containing 80.1% ^{11}B. The boron target was 2-mm thick and mounted to the output port of the accelerator's RFQ. The accelerator operated with a duty factor of 0.6% at 300 Hz and an average deuteron current of 6 µA. The total estimated fast neutron flux was on the order of 10^9 µA^{-1}sr^{-1}, and the gamma flux was estimated at 10^7 µA^{-1}sr^{-1} and 10^6 µA^{-1}sr^{-1} for 4.4 MeV and 15.1 MeV, respectively [31]. Neutron and gamma transmission measurements were conducted with objects consisting pure elements.

A diagram of the experimental setup is shown in Fig. 4.4. Two sets of concrete collimators focused the AI source to a vertical fan beam approximately 5 cm wide. EJ-309 liquid scintillators were used to measure the transmission of photons and neutrons in two different experimental configurations. Figure 4.4 shows the placement of the detector(s) in those two experimental configurations. The circled letters in Fig. 4.4 correspond to the matching circled letters on the photographs in Fig. 4.5.

In the first configuration, a single 7.62 cm (height and diameter) cylindrical EJ-309 detector was placed 8 m from the natural-boron target. The transmission objects were placed approximately 1 m from the natural-boron target and had an approximate areal density of 20 g/cm^2. The dimensions of the test objects were chosen such that they subtended the full solid angle of the detector. Six different objects were tested; the detector and test object remained in a fixed position for an exposure time of 2700 s per object. A simplification of the 1D Beer-Lambert law was applied, where any interaction (including scattering) was assumed to remove the particle outside the solid angle of the detector. Due to the large distance between the transmission object and the detector and the detector's small size, this simplification is valid and renders the effects of buildup for

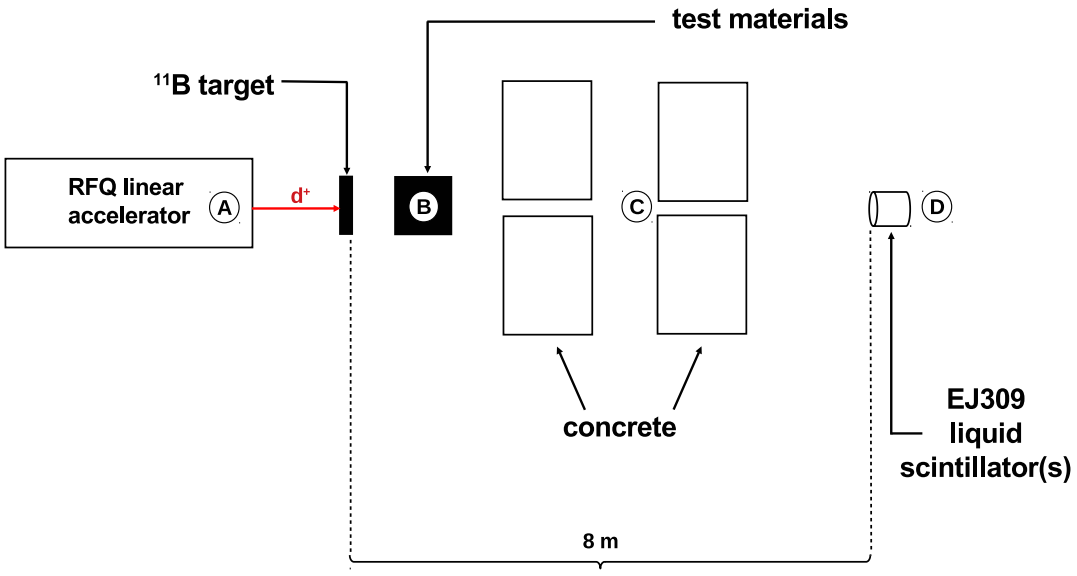

Figure 4.4: Diagram of experimental setup at MIT Research and Engineering Center (not to scale). (A) RFQ linear accelerator, (B) location of material objects for transmission measurements, (C) location of radiographic imaging object, and (D) location of both detector configurations for each of the two experiments

this specific experimental configuration negligible. Table 4.1 lists the measured properties of the test objects used in the experiment using known densities of the materials shown.

Table 4.1: Properties of objects used in experiments at the MIT Research and Engineering Center.

Material	Atomic Number	Density (g cm^{-3})	Areal Density (g cm^{-2})
Al	13	2.7	19.17
Fe	26	7.87	19.68
Cu	29	8.96	18.82
Sn	50	7.3	19.71
Pb	82	11.34	21.87
U	92	19.1	19.4

In the second configuration, a vertical array of eight 5.08 cm (height and diameter) cylindrical EJ-309 detectors was placed 8 m from the boron target. The detector-to-object distance was 4 m. The vertical detector array is shown in Fig. 4.5 (D). The total

Figure 4.5: Photographs from MIT Research and Engineering Center showing the experimental setup of (A) the RFQ accelerator, (B) location of transmission objects, (C) location of radiographic object measured with vertical array, and (D) location of detector placement.

height of the array, measured from centerline-to-centerline between the top and bottom detectors, was 70 cm. The detectors were evenly spaced with a 10 cm distance measured centerline-to-centerline.

A single, combined heterogenous object was tested in the detector array experiment. The dimensions of the combined-material object were chosen to fully subtend the inner six

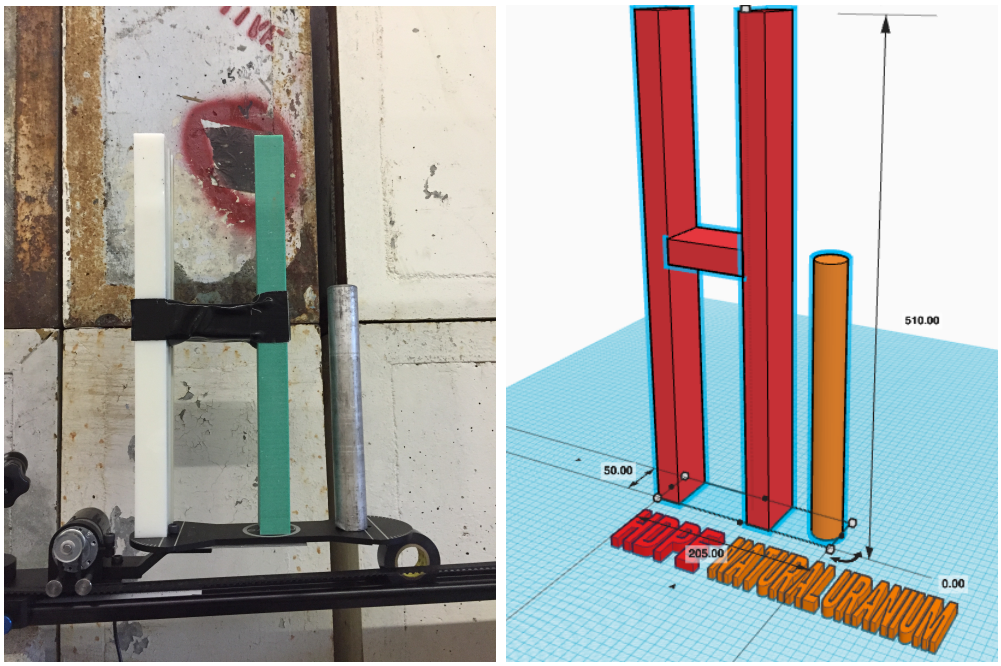

(a) (b)

Figure 4.6: Transmission object used in the vertical detector array experiment showing (a) a photograph and (b) a computer aided design of the object

detectors at the object's maximum height. These dimensions allowed the top and bottom detectors to measure the unattenuated mixed AI beam. The combined object consisted of two types of materials and was in the shape of a letter H and letter i made from high-density polyethylene and depleted uranium, respectively. This object is referred to as the *Hi* object in the remainder of the dissertation. Figure 4.6 shows a photograph and computer-aided design of the object used in the vertical detector array experiment.

The *Hi* object was translated across the beam while the accelerator and detector array remained in a fixed position. The object was moved in 5-mm increments and measured for 300 s at each position over a total of 48 increments. The accelerator beam was interrupted while the object was being moved and restarted once the next position is reached.

In both experimental configurations, CAEN's DPP PSD Control Software was used to measure two preset integral regions, Q_{long} and Q_{short}, for each event [96]. The waveform

integration bounds were set to [t_s, t_s+64 ns] and [t_s, t_s+180 ns] for Q_{short} and Q_{long}, respectively, where t_s is the location of the start of the waveform (trigger position minus gate offset). The short integration region is fully contained within the long integration region for this choice of bounds.

4.3 Results and Discussion

Figure 4.7 shows the response of the 7.62-cm EJ-309 detector in the PSP–light output parameter space when exposed to the 3-MeV deuteron-boron AI source. A fiducial cut was placed around PSP ∼0.21 to select the photon interactions, and a cut around PSP ∼0.27 to select the neutron interactions. A light-output threshold cut was applied at 50 keVee during post-processing.

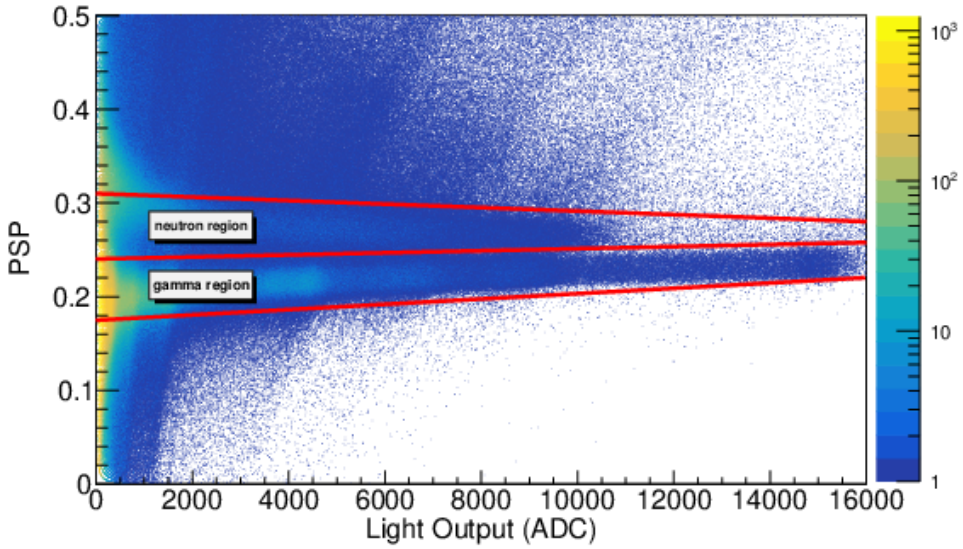

Figure 4.7: Response of the EJ-309 scintillation detector exposed to the accelerator source inducing the ^{11}B(d,nγ)^{12}C and the ^{11}B(d,pγ)^{12}B reaction with a fiducial cut on photon and neutron regions shown in red.

Figure 4.8 (a) and (b) shows the measured photon and neutron transmission spectra obtained by selecting the events within their respective fiducial cuts. The measured

light output distributions are calibrated to electron equivalent using the unattenuated AI beam measurement. Figure 4.9 shows the measured gamma transmission spectra through various materials.

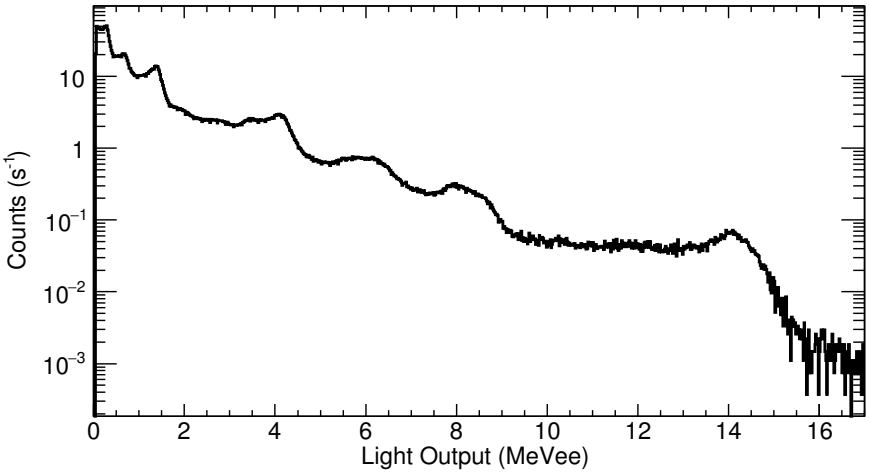

(a)

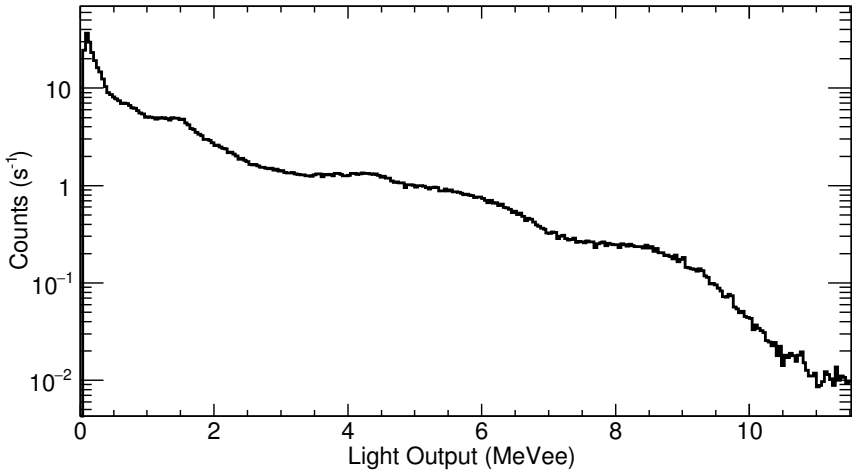

(b)

Figure 4.8: (a) Photon and (b) neutron light output spectrum of ^{11}B(d,nγ)^{12}C AI source measured with EJ-309 liquid scintillator.

Simulation models for four of the primary characteristic photon energies (4.4, 6.7, 8.9, and 15.1 MeV) from the AI source were built to match the measured light output spectra. The origins and yields of the gamma rays produced by the source in this specific

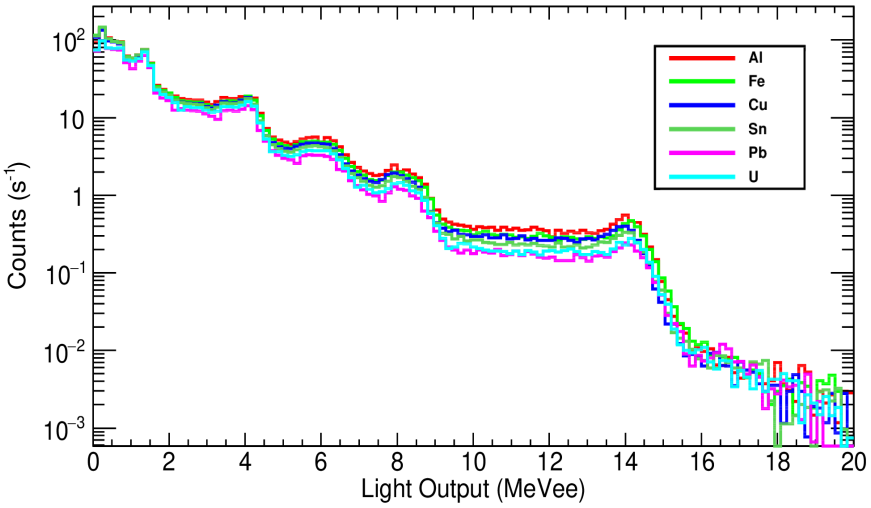

Figure 4.9: Transmitted light output distributions through various materials measured with a 7.62 cm EJ-309 liquid scintillation detector normalized to time and deuteron beam charge.

experimental setup are discussed in greater detail in Refs. [33, 97]. The model was built using the `Geant4` toolkit utilizing the standard EM physics package.

The determination of the individual contributions of the four photon energies was completed in steps. First, an exponential background term is fit to the total light output distribution and subtracted. By removing the contribution of background, the high edge of the light output distribution is solely due to the highest energy photon from the AI source, which is 15.1 MeV. Next, the simulated detector response to the 15.1 MeV photon is fit to the background-subtracted experimental light output spectrum. Analogous to the background subtraction, the simulated 15.1 MeV fit is then subtracted from the background-subtracted experimental light output distribution. The total number of counts in the 15.1-MeV photon simulated-fit light-output distribution is the total number of 15.1-MeV photons detected. The next highest photon energy of 8.9 MeV is then selected and the same steps performed as for the 15.1-MeV photon. In this way, each time the light output spectrum for one photon energy is subtracted, the response at the high

edge of the experimental light-output distribution is exclusively due to the next photon energy descending down the spectrum. This also accounts for the downscatter and partial energy depositions of the higher-energy photons contributing to the total measured light output distribution. Figure 4.10 shows the individual contributions of the four highest gamma-ray energies observed in the experiment.

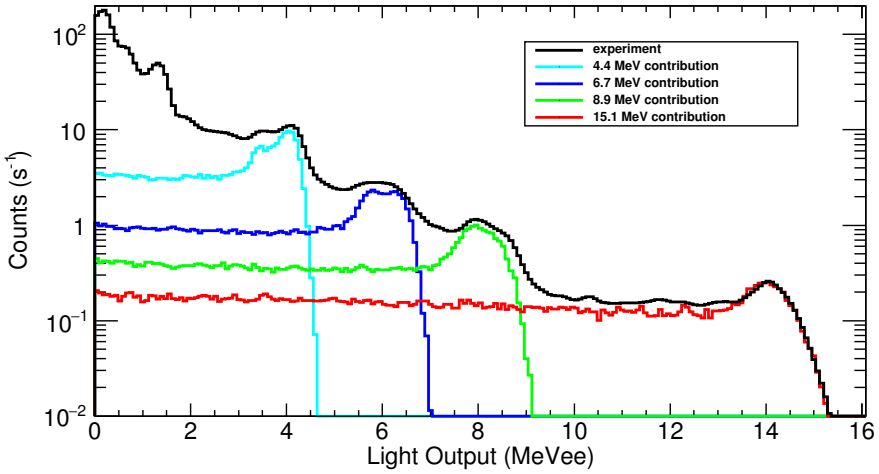

Figure 4.10: Open beam measurement compared to the simulated individual best fit contributions of 4.4-MeV, 6.7-MeV, 8.9-MeV, and 15.1-MeV gamma rays for a 7.62-cm EJ-309 liquid scintillation detector.

Figure 4.11 shows the sum of the individual photon contributions compared to the measured light-output distribution for the 7.62-cm EJ-309 liquid scintillation detector. Minor discrepancies are evident due to disparities in the simulation model with the physical experiment. The model did not include background from physical room components such as surrounding objects, the concrete floor, or the collimators.

The ratio of attenuations of 15.1 and 4.4 MeV gamma rays was experimentally measured for six pure elements – Al, Fe, Cu, Sn, Pb, and U. Figure 4.12 shows a good agreement between the measured transmission and transmission calculated using the 1D model and tabulated photon attenuation coefficients [58].

For higher atomic numbers ($\gtrsim$74), where elemental discrimination becomes critical for

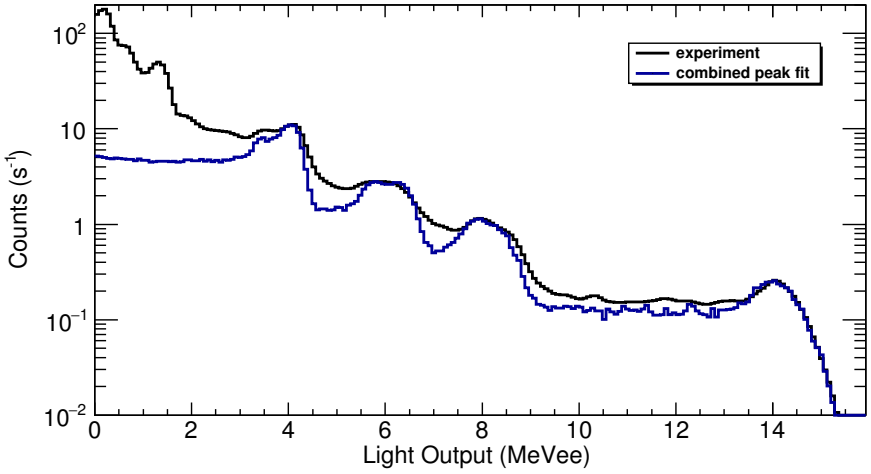

Figure 4.11: Open-beam measurement compared to the simulated combined contribution from the four highest gamma-ray energies from the experiment for a 7.62-cm EJ-309 liquid scintillation detector.

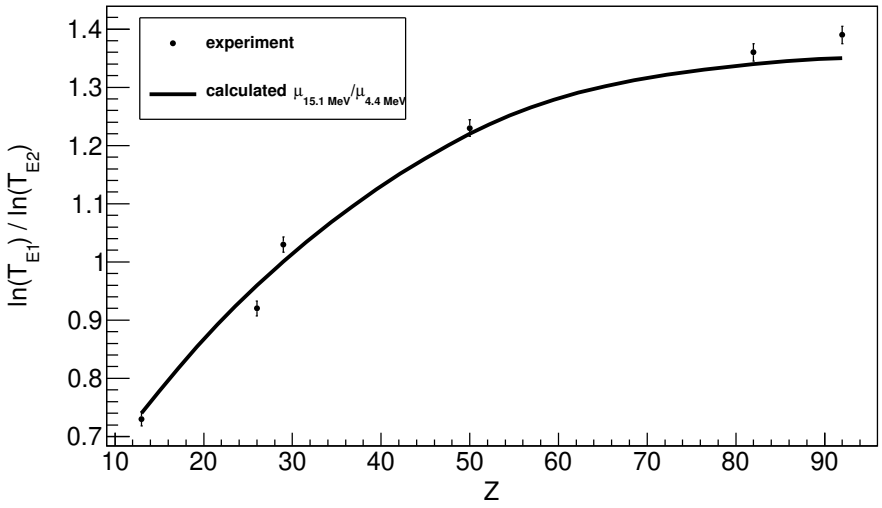

Figure 4.12: The ratio of the natural log of the measured transmission (T) of 15.1 to 4.4 MeV photons (E1 = 15.1 MeV and E2 = 4.4 MeV) compared to the ratio of the mass attenuation coefficients at those energies. The solid black line in not a fit but is calculated from tabulated nuclear data.

SNM identification, the differences in the ratio of attenuation, R, are inadequate when other logistical concerns are taken into consideration. If the experiment were conducted over a sufficiently long time, sufficient statistics would eventually build up to accurately distinguish between Pb and U [32]. The available time in which a material must be identified and the imparted radiation dose, however, are not infinite. There are significant operational concerns when inspecting cargo containers and performing time-sensitive treaty verification measurements. A more sensitive method is desired to perform material identification for these types of applications.

Figure 4.13 shows the neutron and gamma-ray integral transmission image using an array of eight 5.08 cm cylindrical EJ-309 detectors in (c) and (d), respectively. A photograph (a) and computer-aided design (b) of the object are also included in Fig. 4.13 for reference.

The integral transmission image reconstruction was completed post-irradiation. Figure 4.14 shows the detector alignment and corresponding positions. As already stated, the detector array remained stationary, while the object was translated in 5-mm increments. Neutron and photon events are selected based on their pulse shapes and the total number of counts in each particle's fiducial cut (defined in Fig. 4.7) region are tallied. An low light output cut was employed at 500 keVee. Each of the points in the 2D histogram in Fig. 4.13 (c) and (d) is normalized using the unattenuated beam neutron or photon counts measured at that position. The unattenuated integral neutron and photon counts are measured at detector position 7 for each of the horizontal steps.

A qualitative inspection of Fig. 4.13 as expected shows a distinct difference between the neutron and gamma-ray transmission image. In the gamma-ray image, high attenuation is evident in the high-Z material, whereas the low-Z material displays a much lower attenuation. Conversely, the neutron image shows high attenuation in the low-Z material and moderate attenuation in the high-Z material. The disparity in the neutron-

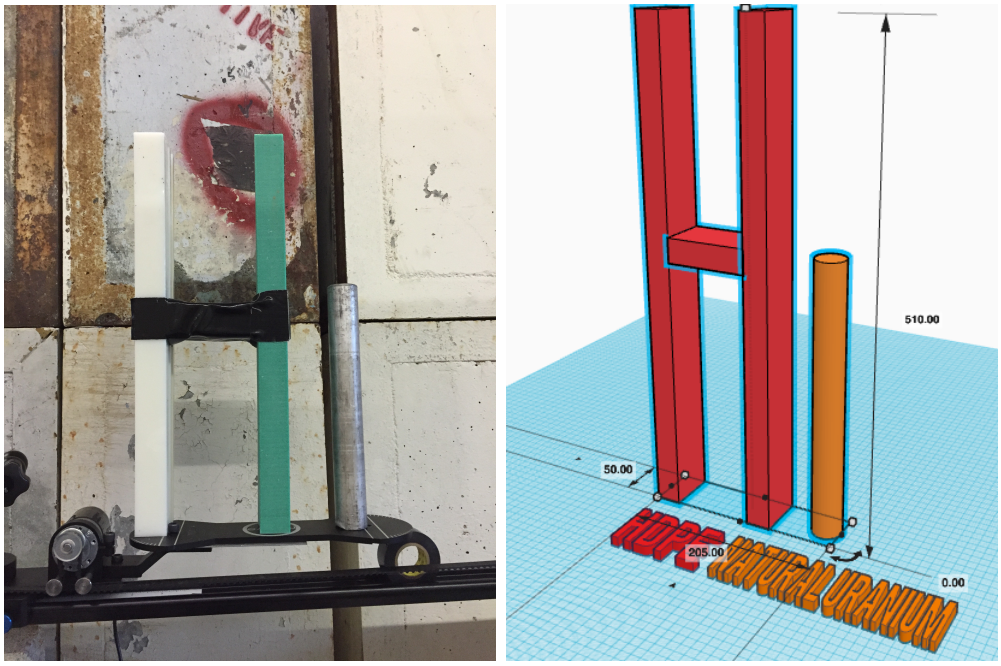

(a) (b)

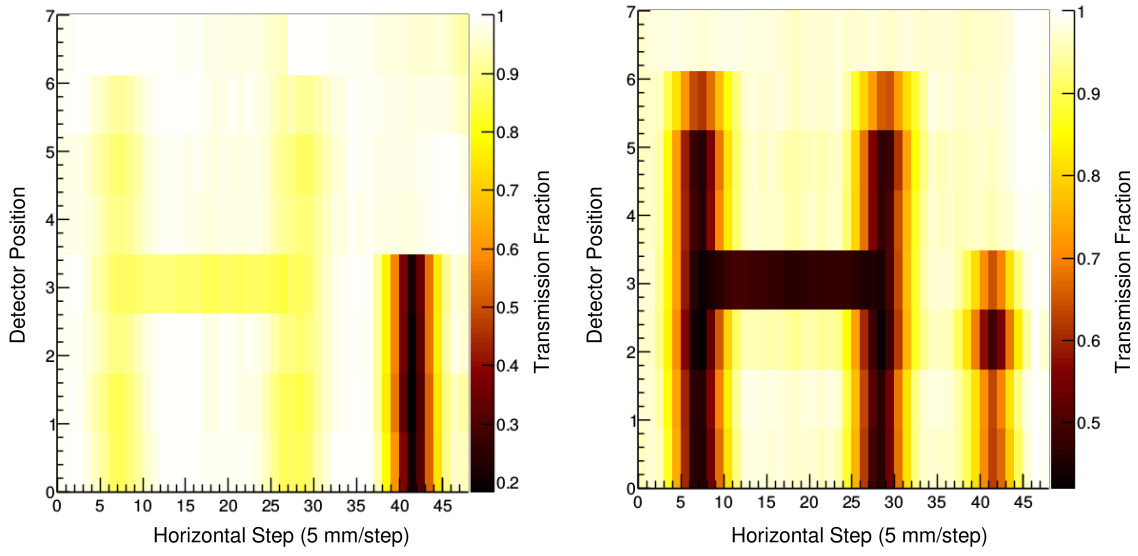

(c) (d)

Figure 4.13: *Hi* object used in the vertical detector array experiment showing (a) a photograph, (b) a computer-aided design, (c) gamma-ray integral image of the object, and (d) neutron integral image of object.

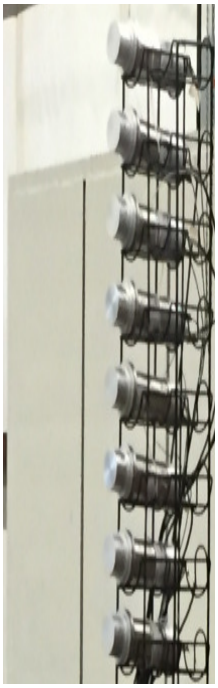

7.1	7.2	7.3	7.4	7.5	7....
6.1	6.2	6.3	6.4	6.5	6....
5.1	5.2	5.3	5.4	5.5	5....
4.1	4.2	4.3	4.4	4.5	4....
3.1	3.2	3.3	3.4	3.5	3....
2.1	2.2	2.3	2.4	2.5	2....
1.1	1.2	1.3	1.4	1.5	1....
0.1	0.2	0.3	0.4	0.5	0....

Figure 4.14: Photograph (left) of a side view of radiography detectors array aligned with (right) the numbered row-column matrix used to indicate the detector positions associated with the neutron and gamma-ray integral images shown in Fig. 4.13.

and gamma-ray-integral transmission images indicates that there is useful complementary information that can be gained if both types of particle attenuation are taken into account. While the integral transmission images offers a simple intuitive view of the material composition, a more complete spectroscopic analysis could offer additional benefits and should be possible because of the spectroscopic nature of the measurement. In this way, it may be possible to overcome simple shielding configurations in which the shield is designed for either photons or neutrons. Because the available experimental time was limited, it was not possible to collect adequate statistics for the results in Fig 4.13; $Z_{effective}$ determination using the ratio of attenuation of 15.1 to 4.4 MeV photons was not performed.

Neutron TOF experiments were not possible with the operational configuration of the DL-3 accelerator, thus not allowing an accurate measurement of the neutron spectrum

produced by the source. Although more general information regarding the elemental composition or content of an unknown object can be obtained using the light output spectrum produced by neutrons [37], accurate material identification using neutron transmission requires that the incident neutron spectrum be known.

Chapter 5

Dual-mode multiple-energy transmission radiography

This chapter discusses the accelerator-based measurements conducted at the Institute for Structure and Nuclear Astrophysics (ISNAP) at the University of Notre Dame (UND). In an effort to improve the performance of material identification using gamma-ray (single-mode) dual-energy transmission radiography, dual-mode transmission radiography is used to more finely differentiate between similar materials. Here, the term *dual-mode* refers to two types of particles and radiation – neutrons and photons. The technique presented in this chapter uses multiple neutron energies combined with a single photon energy. Here, elemental identification is performed by measuring both the neutron and photon transmission through an object. EJ-309 liquid scintillators were used to measure the transmission of both neutrons and photons, and 3-MeV deuterons drove a suitable AI source. The accelerator target used to stop the deuterons at INSAP was boron nitride (BN). It will be shown that the use of dual-mode transmission radiography makes it possible to measure smaller changes in elemental composition of objects in comparison to single-mode radiography presented in the previous chapter.

5.1 Introduction

Photons and neutrons interact differently with matter – photons interact primarily via atomic processes, whereas neutrons interact primarily via nuclear processes. The probability of a neutron interacting with matter depends not only on its element and the isotope. Interactions of a beam of monoenergetic neutrons with an absorber may be described similar to that for photons:

$$I = I_0 \exp(-\Sigma_t x), \tag{5.1}$$

where Σ_t is the total macroscopic cross section of the absorber, x is the absorber thickness, and I and I_0 are the measured intensities of the transmitted neutrons with and without the absorber present, respectively.

Unlike photon interaction probabilities, which exhibit a simple dependence on Z for Compton scattering and pair production, the neutron interaction cross sections can vary strongly with energy and isotope. Figure 5.1 shows the total neutron microscopic cross sections for select materials. Using the unique dependence of neutron interaction properties that depend on both atomic and nucleon number, a ratio (R) that is highly correlated to material type, can be determined using energy-dependent neutron and photon cross sections. Rearranging equation 5.1 to solve for Σ_t and taking the ratio of μ_t (from equation 4.2) and Σ, removes the dependence of material mass and thickness and yields the following equation:

$$R = \frac{\mu_t}{\Sigma_t} = \frac{\ln(I_{E_\gamma}/I_{E_\gamma,0})}{\ln(I_{E_n}/I_{E_n,0})} = \frac{\ln(T_{\gamma,E1})}{\ln(T_{n,E2})}. \tag{5.2}$$

Using Equation 5.2, R-values equal to the attenuation of monoenergetic photons and neutrons can be established. These R-values are experimentally determined by measuring the attenuation of each particle through the objects.

Several different photon and neutron sources have been suggested for use in a material

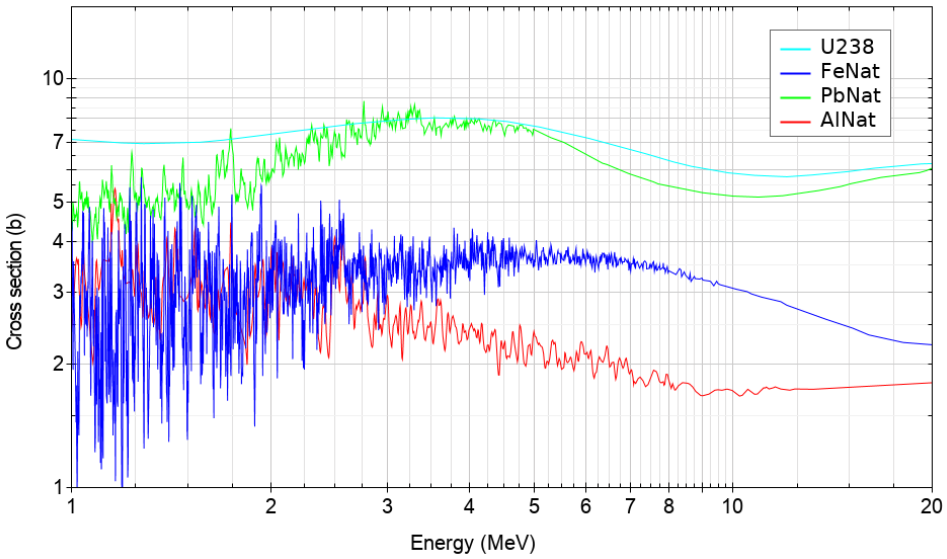

Figure 5.1: Total neutron microscopic cross sections for select materials

identification FNGR system [27]. In Ref. [98], FNGR was implemented by combining a small, compact DT neutron generator with a radioisotope gamma-ray source. The system was able to produce highly resolved radiographic images of air-freight containers. There is a commercial-scale FNGR system based on the work in Ref. [98] installed at Brisbane International Airport in Australia [99]. FNGR may also be performed using a DT neutron source in combination with a continuous higher-energy X-rays, but no substantial work exists utilizing this specific combination [100, 101]. Another FNGR system uses a high-energy accelerator to accelerate deuterons into a gold or an aluminum target producing neutrons and photons [102]. Here, a broad range of photon energies was measured with an endpoint close to 10 MeV. Neutrons at an approximate energy of 8.5 MeV were also produced. However, no robust material identification was reported.

In Ref. [103], it has been suggested that FNGR could be used to detect SNM in cargo containers. In that work, deuterons were accelerated into a boron target to produce both neutrons and photons. FNGR was, however, not pursued, nor there was any material discrimination using FNGR attempted. To date, no work has been reported using a

single source to perform material identification using FNGR. Further, no single type of detector has been used to simultaneously measure neutron- and photon- spectroscopic attenuation to support the FNGR material identification technique. Also, no work has been conducted that combines multiple spectroscopic FNGR signals to perform material identification. In this chapter, a method that uses four spectroscopic FNGR signals originating from a single AI source is presented to accurately identify pure materials and detect mixtures of material such as shielded SNM.

5.2 Materials and methods

Experiments were conducted using the 10-MV FN tandem accelerator at the ISNAP located at the UND. Neutrons and gamma rays produced from a 3-MeV deuteron incident onto a thick boron nitride target were measured with a 7.62-cm EJ-309 liquid scintillator in two experimental configurations. Two rooms – the West and East Target rooms – were used for the experiments at INSAP. Figure 5.2 shows the experimental rooms, placement of detectors in the two experimental configurations, and accelerator location at UND INSAP.

The detector was coupled to a 7.62 cm to 5.08 cm conical acrylic light guide and mounted to a Hamamatsu PMT, model number R6321. The PMT was powered using a CAEN DT5533N desktop high-voltage power supply. The PMT signals were digitized using a CAEN DT5730 14-bit, 500-MS/s digitizer and saved to data files for post-processing. The digitizer was connected to a Linux computer via USB with a transfer rate of 30 MB/s. The digitizer used the DPP PSD CAEN firmware package and a `ROOT`-based graphical interface for data acquisition and display [104].

The objective sought in the first experimental configuration was to measure the TOF of neutrons from the deuteron-BN source. The detector was placed in the West Target

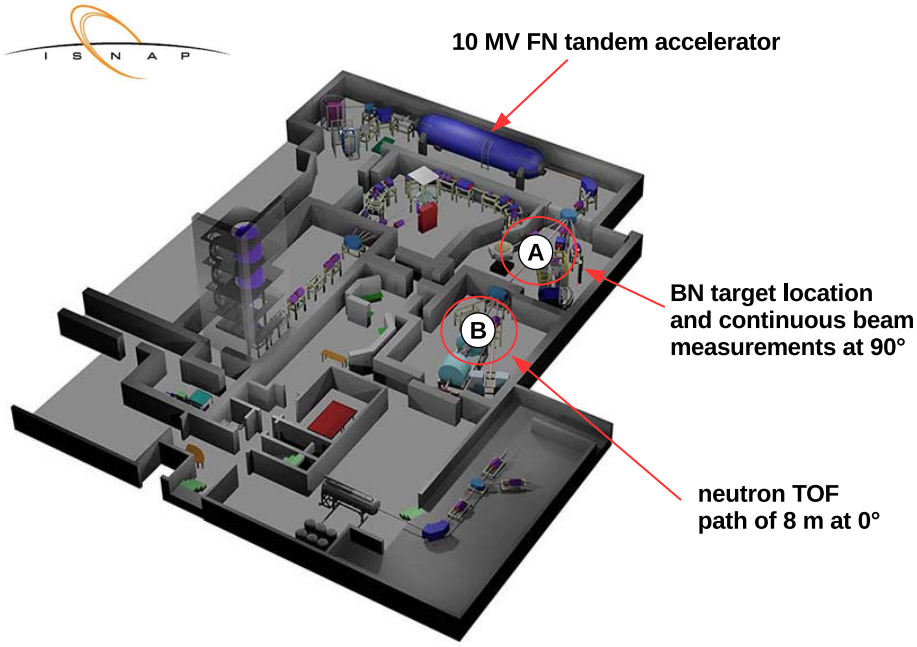

Figure 5.2: Layout of the UND ISNAP laboratory and locations of experiments: (A) East Target Room (B) West Target Room

Room, 7.3 m from the boron-nitride target. Figure 5.3 shows a photograph of the detector in place for the neutron TOF experiment. The detector was placed on beam axis, ∼1.8 m from the floor and 4 m from surrounding walls.

Due to the lack of a shielded neutron TOF tunnel at the UND facility, special considerations were taken into account when designing the experiment. The boron nitride target was placed in an experimental room adjacent to the room with the neutron TOF detector, providing a long TOF distance (∼8 m). Separating the two rooms was a 1.3-m thick concrete wall, which collimated the neutron/gamma-ray AI source to an approximate beam diameter of 5 cm and reduced the abundance of room-scattered neutrons.

The accelerator was operated to deliver a deuteron pulse every 600 ns. A beam buncher and sweeper were utilized to reduce the duration of the deuteron pulse from the accelerator to less than 2 ns. Fourier convolution was used to study the effects of the

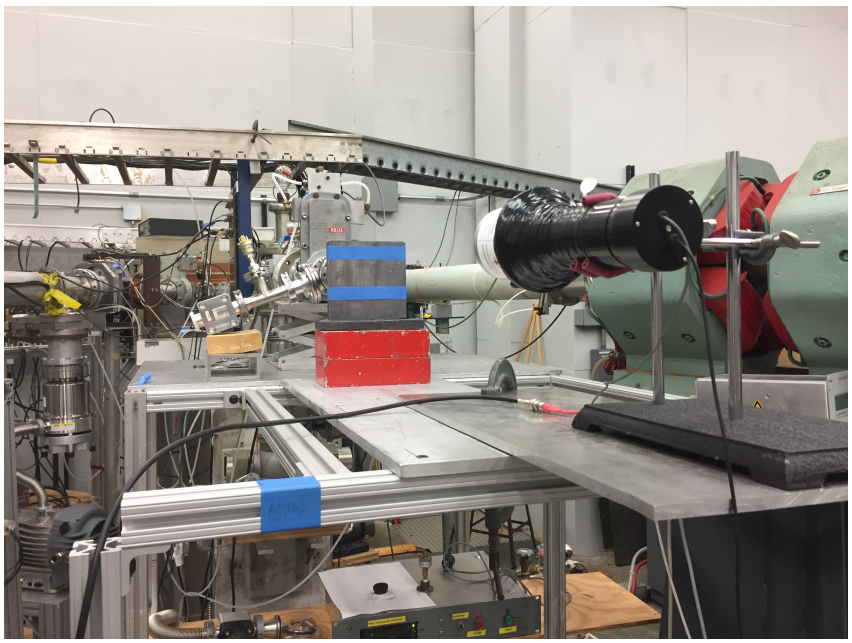

Figure 5.3: Photograph of neutron detector at the UND ISNAP laboratory in position for the neutron TOF experiment

broadening of the resulting neutron TOF spectrum based on the duration of the deuteron pulse. It was found that a deuteron pulse shorter than 2 ns did not significantly broaden the TOF spectrum. A 3-mm thick BN target with a composition of 95% boron nitride and 5% boron trioxide was used to fully stop the 3-MeV deuterons.

The accelerator signal and detector signal were recorded by one digitizer. A valid trigger signal in the detector channel prompted the recording of both the detector and accelerator signal with an accurate time stamp provided by the digitizer. The accelerator signal alone did not result in any recorded data. The record length was 1.2 µs, such that that two accelerator signals were captured along with each detector pulse. The post trigger for events occurring on the detector digitizer's channel was set to 50%.

Neutron and photon events were identified based on the observed pulse shape in the EJ-309 detector and analyzed on an event-by-event basis. The waveform data were processed using a custom analysis code to calculate and subtract the waveform baseline and subsequently determine the pulse height, pulse-peak position, and the PSP of individual

events within the collected waveforms. The event integration bounds were set to [t_s, t_p+22 ns] and [t_s, t_s+200 ns] for Q_{short} and Q_{long}, respectively, where t_s is the location of the start of the waveform (peak position minus 16 ns) and t_p is the location of the peak. The short integration region is fully contained within the long integration region for this choice of bounds.

Figure 5.4 shows PSP as a function of light output measured with the EJ-309 liquid scintillation detector. The neutron and photon events were separated by placing fiducial cuts on their corresponding regions above and below the PSP value of 0.22 for neutrons and photons, respectively.

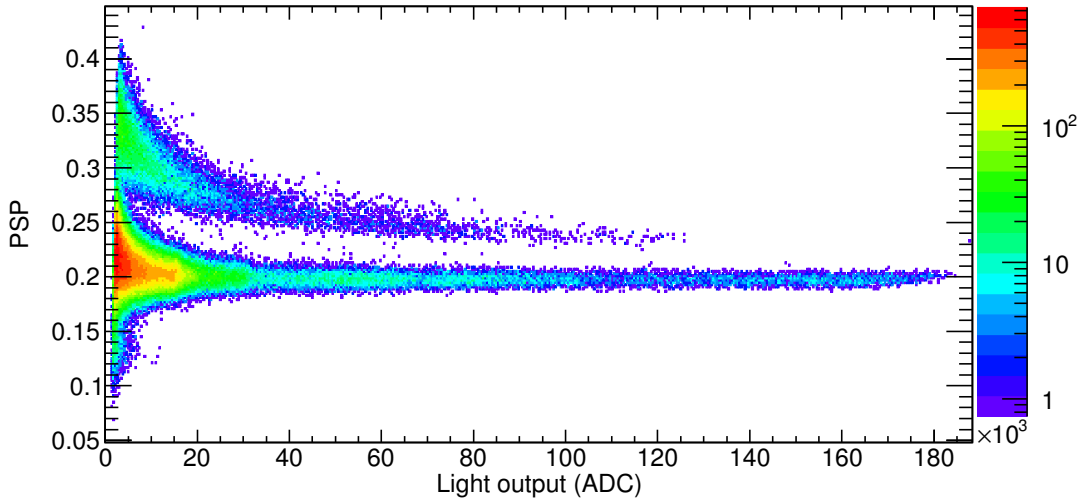

Figure 5.4: PSP as a function of light output recorded by the EJ-309 liquid scintillation detector for 3-MeV deuterons incident on a thick BN target

Each accelerator pulse established a start signal, t_{start}, to mark the time the deuteron struck the BN target. The particle detector was fixed at some measured distance, d, from the BN target. For each registered pulse in the detector, the threshold trigger time gives the time of detection, t_{stop}. The difference of $t_{start} - t_{stop}$, or the TOF, is tabulated.

The photons measured in the liquid scintillator were used to measure the "gamma flash" from a deuteron striking the BN target. The gamma-ray TOF spectrum, showing

the gamma flash and the gamma-ray background is shown in Fig. 5.5. The width of

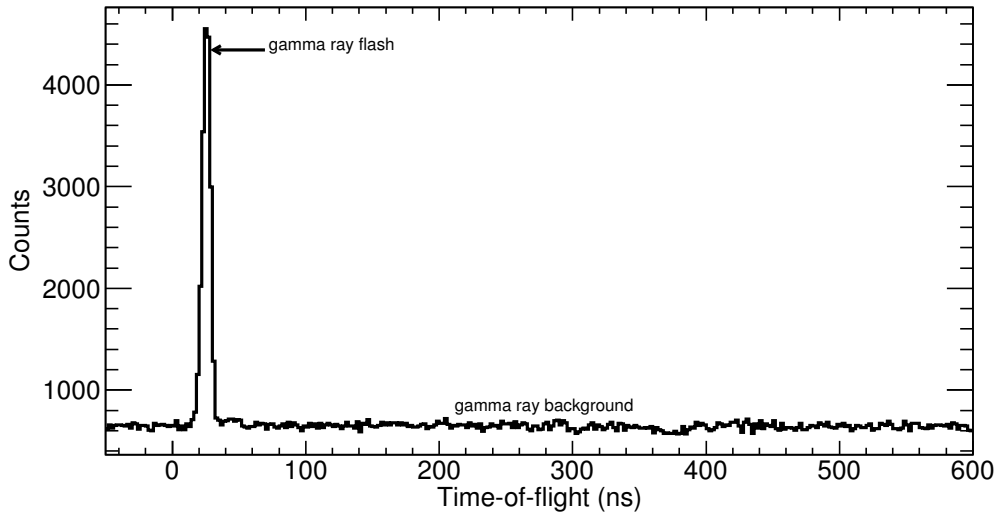

Figure 5.5: Full gamma-ray TOF spectrum measured at UND INSAP with an EJ-309 liquid scintillation detector

the prompt gamma-ray peak was 5.85 ns (Fig. 5.6). This width includes contributions from the detection system (scintillator, light guide, PMT, digitizer, and cabling) and the beam-bunching system, and results in a neutron energy resolution of approximately 1 MeV for 14.5-MeV neutrons and about 20 keV for 4-MeV neutrons.

The TOF was used to calculate neutron energy on an event-by-event basis. Figure 5.7 shows the neutron TOF spectrum from the unattenuated mixed-particle AI beam produced from a 3-MeV deuteron striking the thick BN target. As the deuteron loses energy in the BN target, neutrons are produced at decreasing energies correlated to the different excited states and kinematics of the various reactions occurring the target. Neutrons are continuously produced until the deuteron energy drops below the Coulomb threshold of the lower of the two target nuclei – 1.7 MeV for ^{11}B or 2.3 MeV for ^{14}N. Table 5.1 lists the two main neutron-producing reactions from the deuteron-BN AI source and the resulting gamma rays [105, 106].

The measured neutron energy spectrum is shown in Fig. 5.8. These results are in

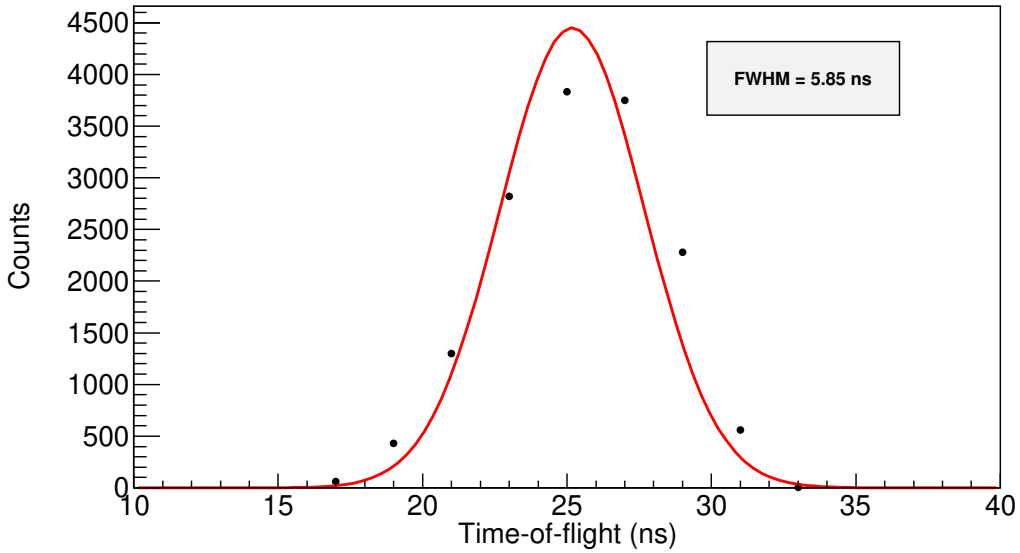

Figure 5.6: Gamma-ray peak in the TOF spectrum with background subtracted. A Gaussian distribution is fit (red) to the peak yielding a full width half maximum of 5.85 ns.

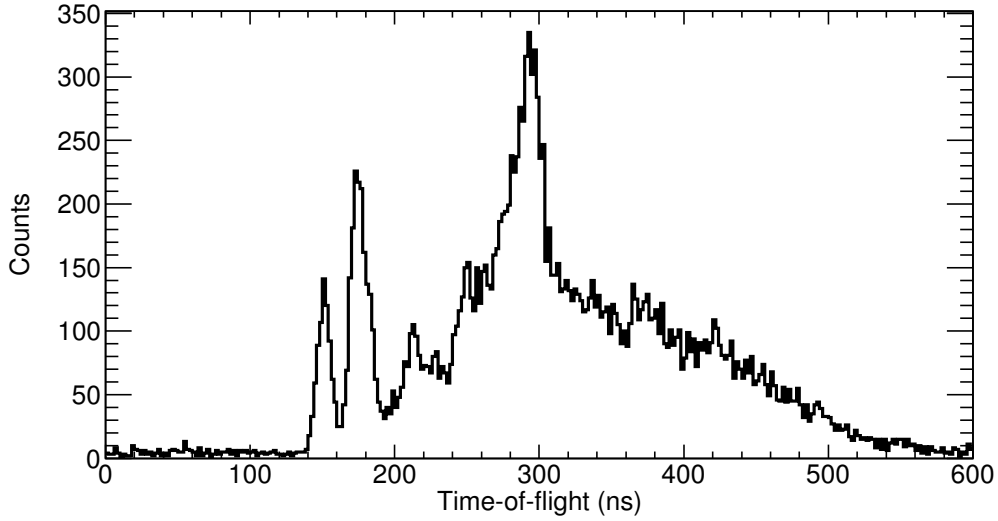

Figure 5.7: Neutron TOF spectrum measured with an EJ-309 detector at UND INSAP from a pulse of sub-2 ns bunched 3-MeV deuterons striking the thick BN target

agreement with neutron energies measured in similar experiments with the ^{11}B(d,nγ)^{12}C reaction conducted in Refs. [46, 103]. In the figure, a broad distribution of neutron energies is observed and caused by the slowing down of the deuteron in the BN target.

Table 5.1: Excited nuclear states for selected reactions of deuteron bombardment of BN and their associated gamma-ray energies [105, 106].

Reaction	Q-value (MeV)	Gamma-ray Energies (MeV)
^{11}B(d,nγ)^{12}C	13.73	4.44, 9.64, 15.1
^{14}N(d,nγ)^{15}O	5.07	5.18, 5.24, 6.18, 6.79. 7.28, 7.56

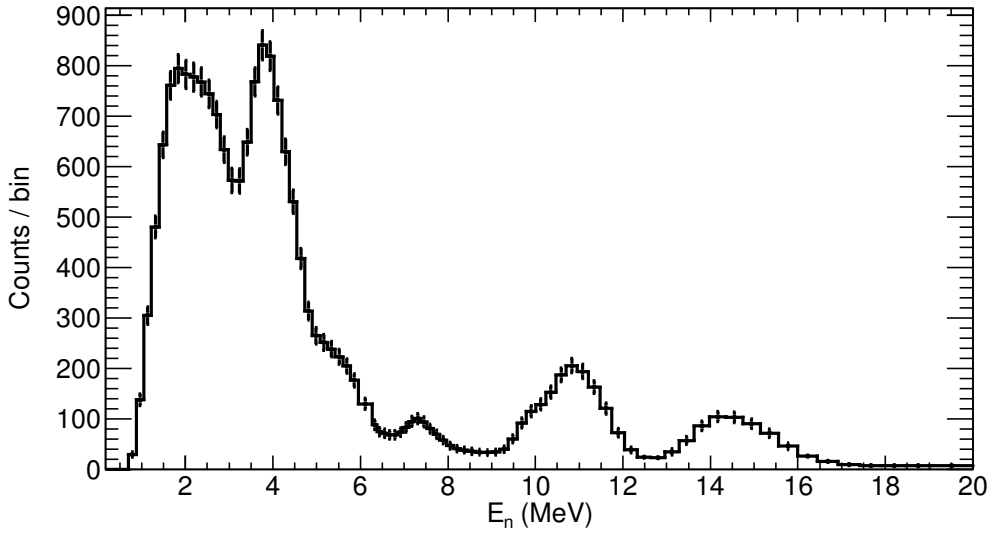

Figure 5.8: Measured neutron energy spectra at 0 degrees for a 3 MeV deuteron incident onto a 3 mm thick BN target

Five different pure-elemental test objects (Al, Cu, Sn, Pb, and Bi) and one metal alloy test object were placed in the beam path, and the particle transmission was measured with the liquid scintillator for two hours per object. The pure-elemental objects had natural isotopic abundance, and the tungsten alloy consisted of 6% Ni, 4% Cu, and 90% W. The effective atomic number for the W-alloy was calculated using a custom open-source software, Auto-Z_{eff} [107]. All transmission objects were placed 60 cm from the face of the detector. Figure 5.9 shows a diagram of the experimental setup.

Monte Carlo simulations were performed in `Geant4` using the principal neutron energies produced (Fig. 5.8) in the d-BN reaction (4, 7.5, 11, and 14.5 MeV) with exact dimensions and materials of the experiment to study the effects of build up in the detector. For each of the materials listed in Table 5.2, 10^5 neutrons at each of four principal

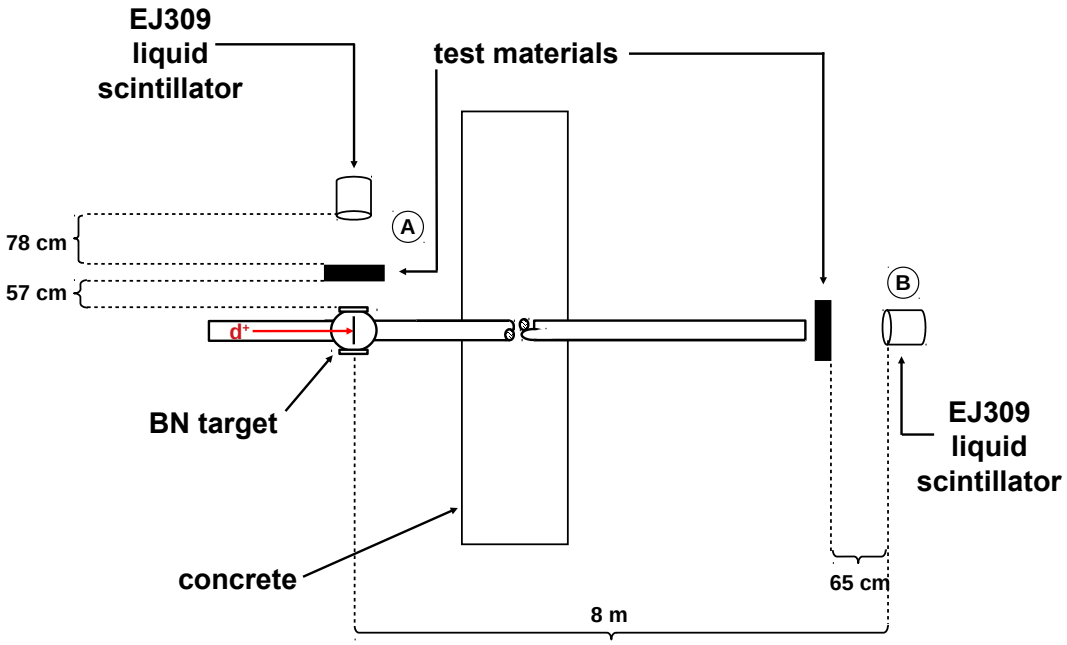

Figure 5.9: Layout of the UND ISNAP laboratory and locations of components: detector placement for (A) continuous beam photon measurements and (B) for neutron TOF experiment.

neutron were individually simulated. The exact experimental dimensions of the objects are listed in Table 5.2 and distances listed in Fig. 5.9 for the neutron-TOF experiment. All neutrons less than the initial source neutron energy that deposited energy in the detector were tallied. The buildup effects were found to be negligible with <1% of neutrons reaching the detector with less than the source neutron energy. Therefore, the simplification of the Beer-Lambert law using the total neutron cross-section was used in the neutron-transmission calculations.

Due to the limited experimental time, the experimental configuration was altered to achieve sufficient counting statistics when measuring the 15.1 MeV gamma rays from the d-BN source. In this second experimental configuration, the detector was transferred to the same room as the BN target (East Target Room). The detector was placed at an angle of approximately 90 degrees with respect to beam axis, with the face of the detector

Table 5.2: Properties of objects used in particle transmission experiment at UND ISNAP.

Material	Atomic Number	Density (g cm^{-3})	Areal Density (g cm^{-2})
Al	13	2.7	18.1
Cu	29	8.96	17.1
Sn	50	7.3	25.1
W alloy	64.7	17	25.3
Pb	82	11.34	22.5
Bi	83	9.78	30.3

78 cm from the BN target. The accelerator was operated in continuous mode. The same six objects were inserted between the BN target and the detector, and the particle transmission was measured for 30 minutes per object. The dimensions and placement of the objects were selected to cover the full solid angle of the detector. Figure 5.9 shows a diagram of the experimental setup used for the continuous beam experiment.

As in the neutron TOF experiment, neutron and photon events were categorized based on their pulse shape. Figure 5.10 shows the pulse shape parameter, PSP, as a function of light output measured with the EJ-309 liquid scintillation detector for the second experimental configuration. When compared to Fig. 5.4, event pile-up is evident in the lower light output region. Only the response to 15.1-MeV gamma rays was relevant for material determination. In the range of the light output distribution corresponding to 15.1-MeV gamma-rays (1.9×10^5 ADC), event pile-up was negligible.

Photon events in the detector were selected within a fiducial cut centered at a PSP value of $\sim$0.22 in Fig. 5.10. Fig. 5.11 shows the experimental photon light-output spectrum measured with the EJ-309 detector from the d-BN source, with a distinct 15.1-MeV region displayed in the inset. Other features are observable in the spectrum from other prominent gamma rays from the source, but are difficult to identify due to the modest detector resolution.

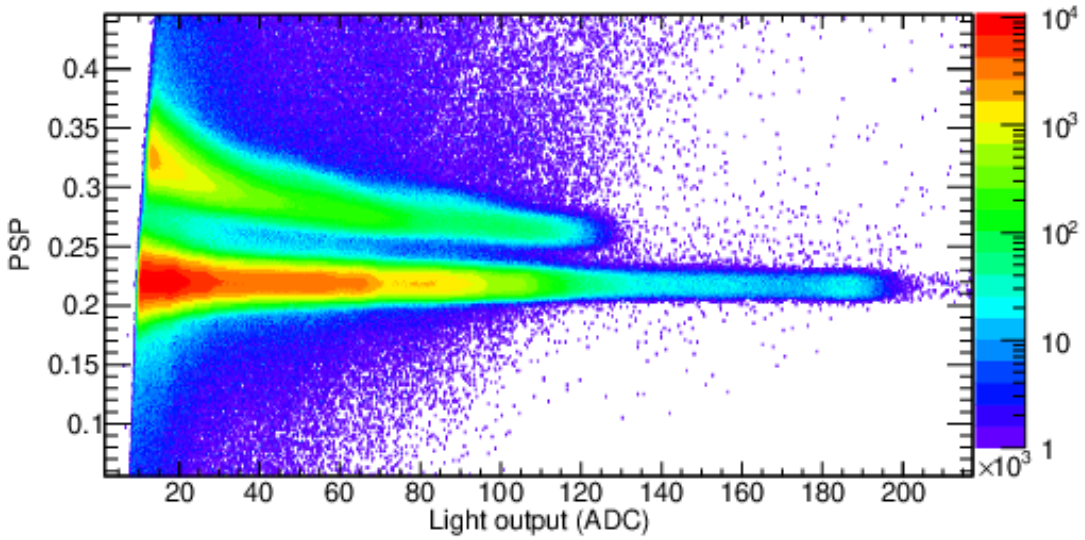

Figure 5.10: PSP as a function of light output from the EJ-309 liquid scintillation detector for a 3 MeV deuteron incident on a thick BN target with the accelerator operating with a 100% duty cycle.

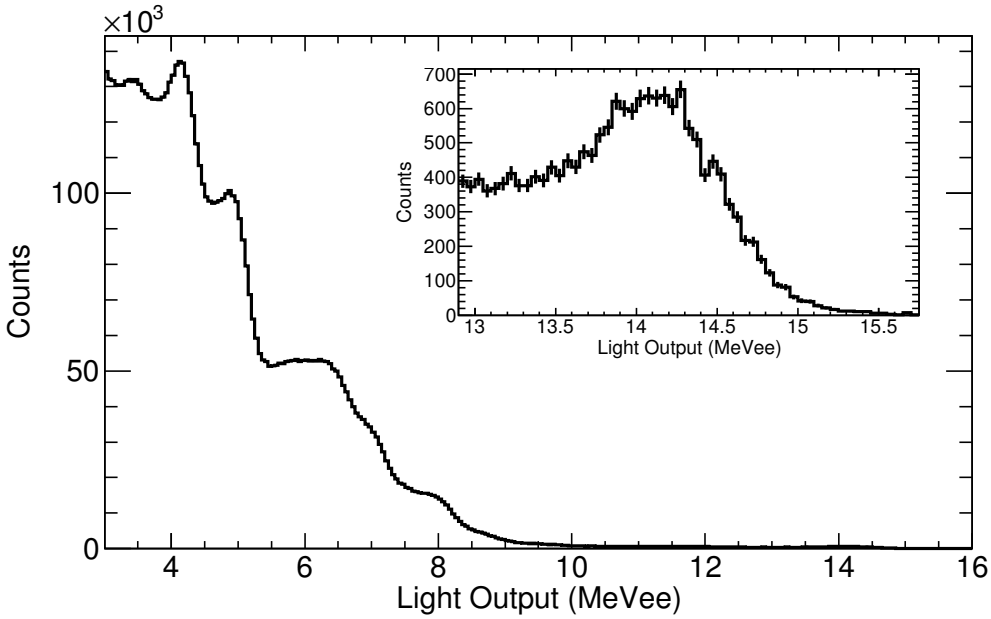

Figure 5.11: Sample gamma spectrum measured in the EJ-309 detector for the unattenuated beam.

In addition to the gamma-ray energies listed in table 5.1, other gamma-ray energy lines originate from different reactions occurring in the BN target. Table 5.3 lists the

Table 5.3: Excited nuclear states for selected reactions of deuteron bombardment of BN and their associated gamma-ray energies.

Reaction	Q-value (MeV)	Gamma-ray Energies (MeV)
^{14}N(d,$\alpha\gamma$)^{12}C	13.57	4.44, 9.64, 15.1
^{14}N(d,pγ)^{15}N	8.609	5.29, 6.32, 7.16, 7.30, 8.31, 9.15, 10.8

other reactions involving ^{14}N and their respective gamma-ray energies.

With the distances (target-to-object and object-to-detector) of the continuous beam experiment, a significant number of photons undergo small-angle scatter and contribute to the light-output distribution. Photon spectroscopy via spectrum stripping depends on having a well-understood simulated detector response. If the simulated response does not include the contributions from small-angle photon scatter, then the 1D attenuation law alone cannot fully describe the experimental reality.

A `Geant4` simulation was performed to study the build up of 15.1 MeV photons when passed through an object and then into an EJ-309 liquid scintillator. The simulation accounted for the exact experimental dimensions and distances. Figure 5.12 shows two simulated EJ-309 light output distributions, one from an unattenuated beam of 15.1 MeV photons, and one from a 15.1 MeV photon beam attenuated by a Pb object with dimensions as described in Table 5.2. Below 2 MeVee, the two spectra diverge, which is attributed to a 15.1 MeV photon undergoing an interaction that does not remove it or its secondary particle fully from the beam path. These scattered or secondary photons are detected, which is contrary to the assumption of the 1D model. These photons have energy below 15.1 MeV and thus contribute more to the low end of the spectrum. Spectrum stripping relies on an accurate fit of the simulated response to prominent features in the experimental data. The unattenuated simulation does not account for the secondary photons from the 15.1 MeV feature results in an overestimate of the transmission.

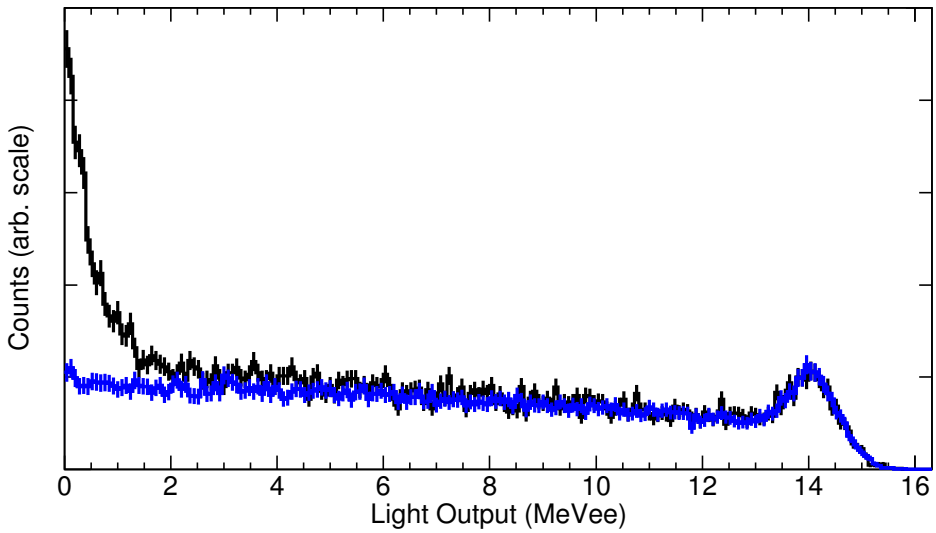

Figure 5.12: Two simulated EJ-309 light output distributions: an unattenuated beam of 15.1-MeV photons (blue) and a 15.1-MeV photon beam attenuated with the exact dimensions of the Pb object (black) described in Table 5.2.

Figure 5.13 shows two simulated EJ-309 light output distributions of a 15.1-MeV photon beam attenuated with the exact dimensions of the Pb object described in Table 5.2. The distribution in black shows all events depositing energy in the detector, while the distribution in red included only events that interact in the Pb object before reaching the detector. Figure 5.13 indicates that a significant number of source 15.1-MeV photons undergo an interaction before detection. The percent of photons that deposit energy in the detector that are less than 15.1 MeV is approximately 10% (buildup percent) for all objects listed in Table 5.2; the gamma-ray transmission results were corrected for small angle scatter events by reducing the total number of 15.1 MeV events for each of the materials by its respective buildup percent.

A separate liquid scintillation detector was used to monitor any accelerator beam-current fluctuations and normalize the individual object transmission measurements. The detector was located in the East Target Room (Fig. 5.2) approximately 4 m from the BN target. Photon events located in the high-edge of the light output distribution–10 MeVee

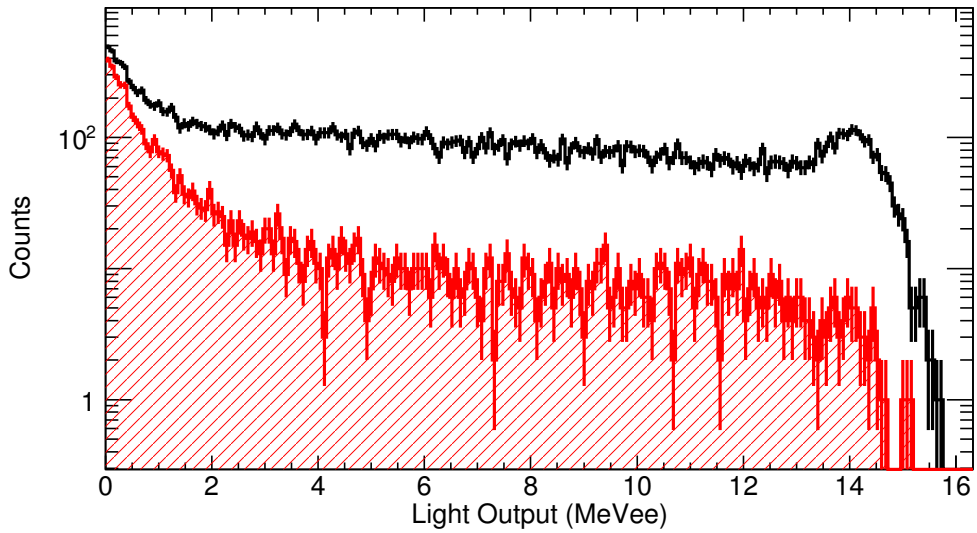

Figure 5.13: Two simulated EJ-309 light output distributions of a 15.1-MeV photon beam attenuated with the exact dimensions of the Pb object (black) described in Table 5.2: all events depositing energy in the detector (black) and events which first undergo an interaction before reaching the detector (red).

to 15 MeVee– were selected, and the average detected photon rate calculated. A normalization factor was calculated by dividing the measured photon rates observed during each of the objects experiments by the photon rate observed during the unattenuated AI source measurement. The calculation of the neutron and photon transmission used the unattenuated number of counts at each energy measured with the TOF detector increased by its corresponding normalization factor. Figure 5.14 shows the calculated normalization factors for the individual neutron transmission measurements during the neutron-TOF (pulsed-beam) experiment. This was completed for both the pulsed- and CW-beam experiments, with the CW-beam experiment yielding similar results.

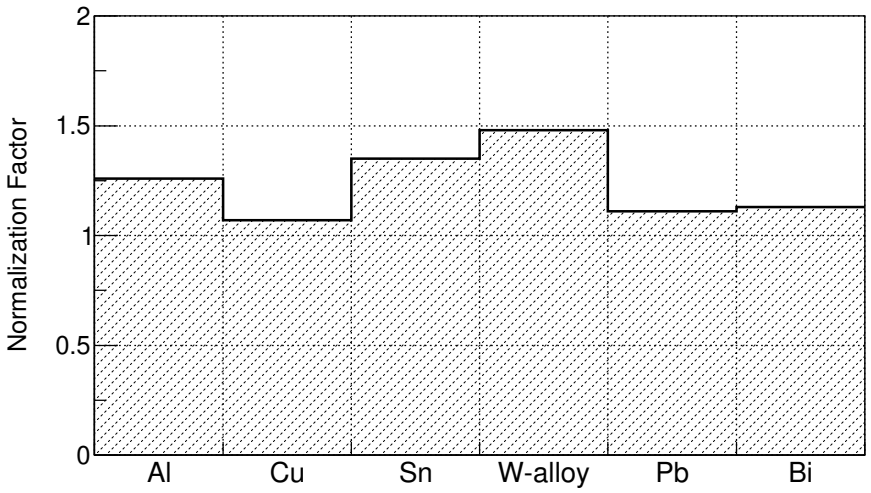

Figure 5.14: Object normalization factor for neutron-TOF experiment, where the normalization factor is equal to the ratio of the measured photon rate corresponding to the time during which the object's was measured and the unattenuated photon rate.

5.3 Results and discussion

The transmission of 15.1-MeV gamma rays through objects listed in Table 5.2 was experimentally measured. The total number of gamma rays transmitted through the object was obtained in accordance with the *spectrum stripping* procedure outlined in chapters 2 and 4. Each measurement was corrected for buildup and deuteron beam current. Figure 5.15 shows the experimental results, which are in good agreement to analytically calculated values based on tabulated nuclear data [58].

Four prominent energies (4, 7.5, 11, and 14.5 MeV) were identified in the neutron energy spectrum for material transmission studies. Figure 5.16 shows the unattenuated neutron energy spectrum from the d-BN ($E_d = 3$ MeV) source with arrows indicating the peaks.

The neutron transmission at each of the four energies was measured by summing the counts under the peak and the neighboring energy bins (one below and one above). This is carried out for the unattenuated neutron beam and the measurements with the

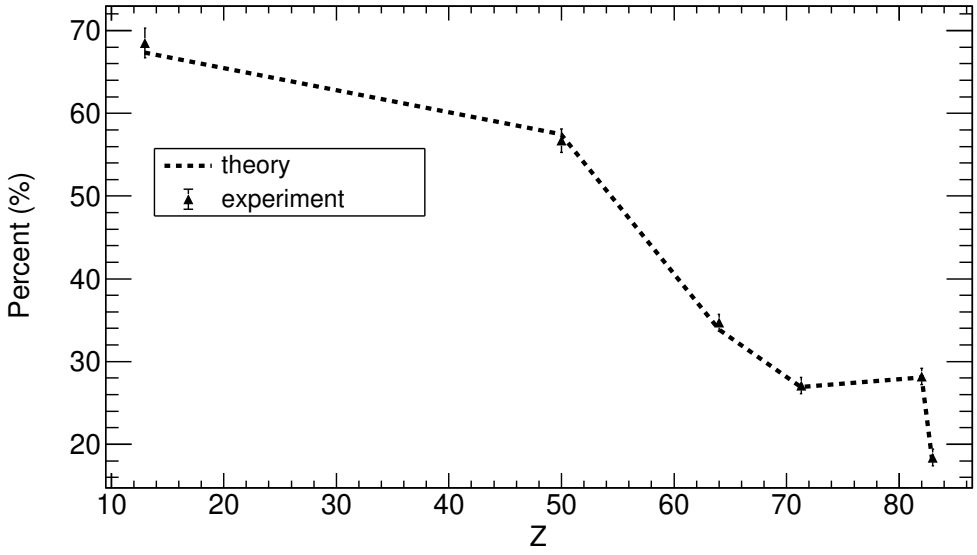

Figure 5.15: Measured 15.1 MeV gamma-ray transmission through various objects compared to analytically-calculated values based on tabulated nuclear data [58].

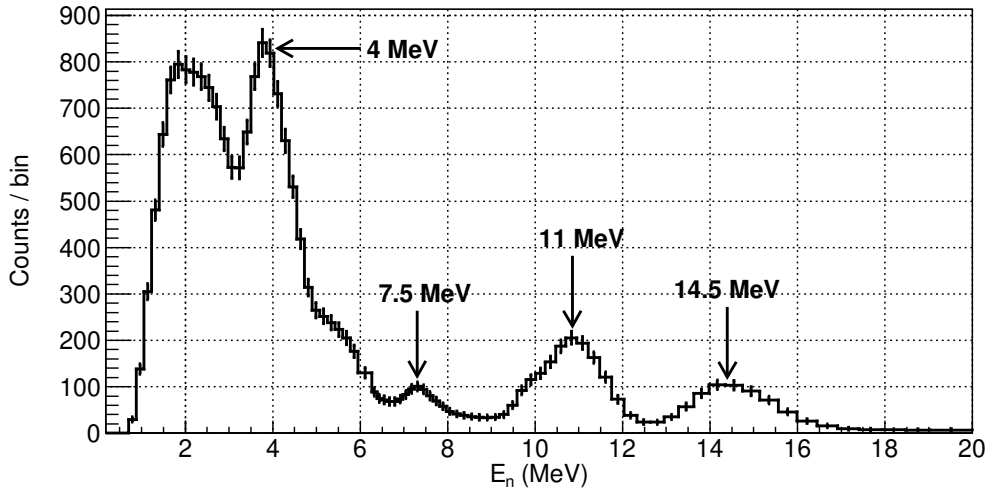

Figure 5.16: Measured neutron energy spectra at 0 degrees for a 3 MeV deuteron incident onto a 3 mm thick BN target indicating four neutron energies that can be used for material identification.

beam attenuated by each of the objects. Figure 5.17 shows the experimental results for each of the materials, which are in good agreement to calculated values based on tabulated nuclear data [58]. The transmission values are analytically calculated using the

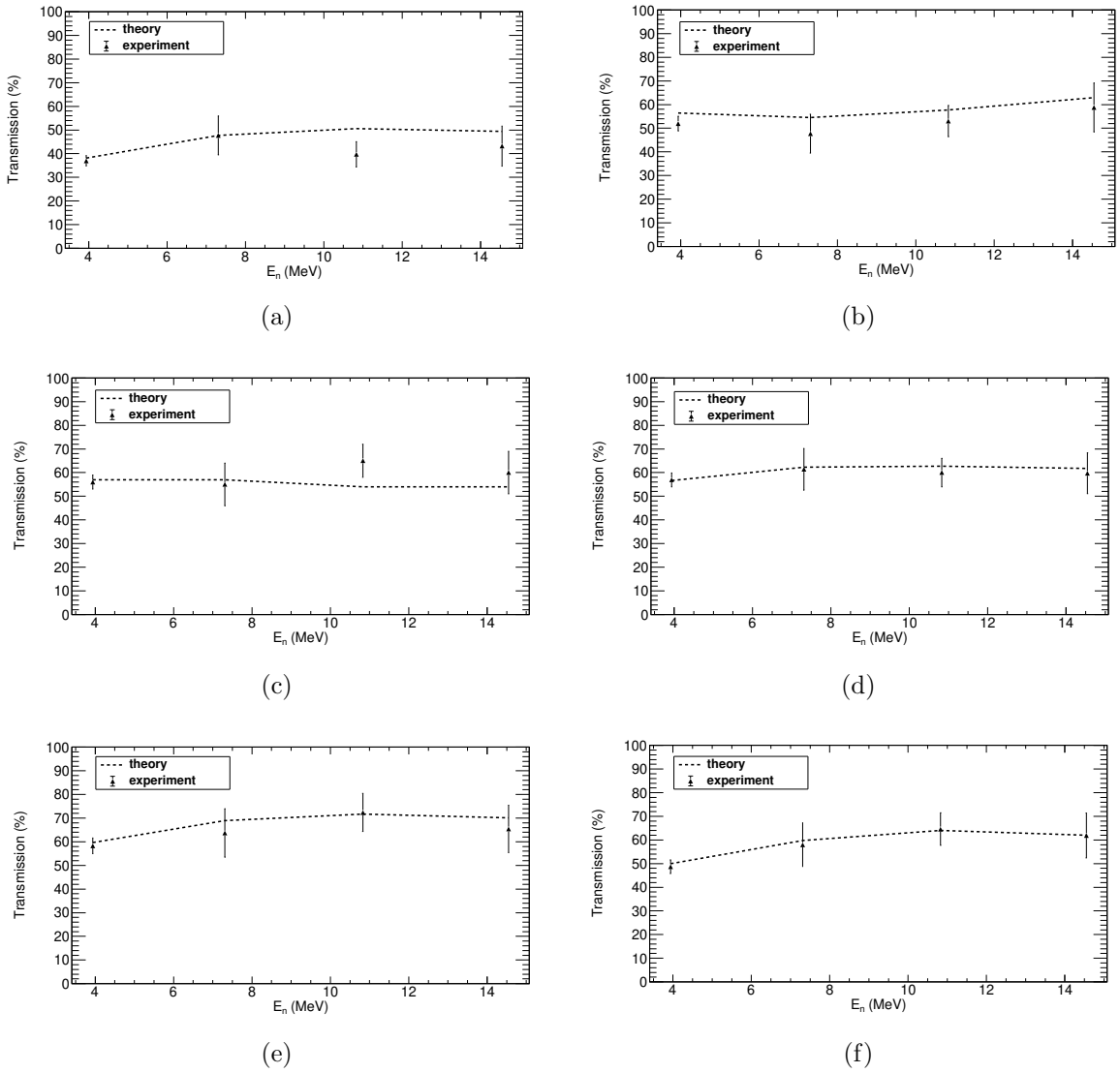

Figure 5.17: Measured neutron transmission at 4, 7.5, 11, and 14.5 MeV through (a) Al, (b) Cu, (c) Sn, (d) W alloy, (e) Pb, and (f) Bi objects, compared to analytically-calculated values.

total macroscopic cross-sections and the measured thicknesses of the elements listed in table 5.2 [59, 108, 109]. Natural isotopic fractions of the corresponding elements are assumed.

For all remaining figures and tables in this chapter, natural isotopic fractions of the corresponding element are assumed for each listed value of Z.

Using Equation 5.2, four R-values can be established, where each R-value is equal to the ratio of attenuation of neutrons at different energy and 15.1-MeV photons. The analytical calculation of the R-values assumes natural isotopic abundance for the pure-elemental objects. Figures 5.18 through 5.21 show the experimentally measured R-values compared to the analytically calculated values. The dashed lines in the figures do not represent a function of Z, but a simple interpolation between points. As stated earlier, neutron attenuation is nonuniform across the periodic table and is not a direct function of atomic number.

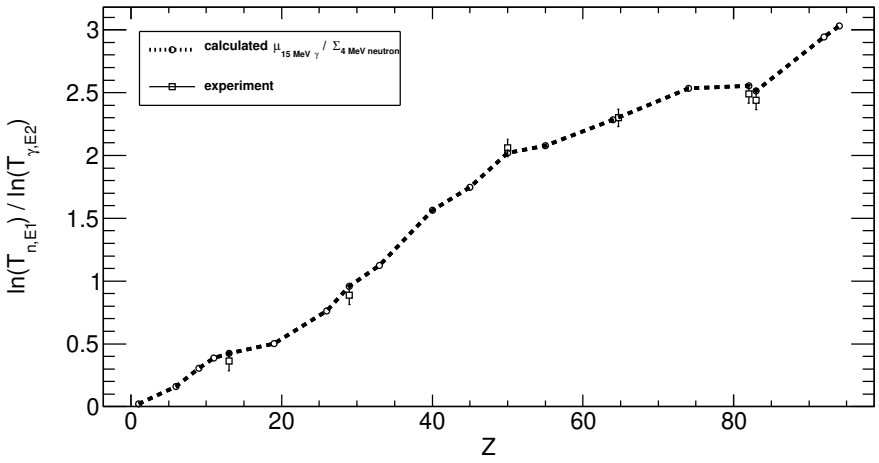

Figure 5.18: R_1: the ratio of the natural log of the measured transmission (T) of 15.1 to 4 MeV neutrons compared to the ratio of the mass-attenuation coefficient to the macroscopic cross section at those energies.

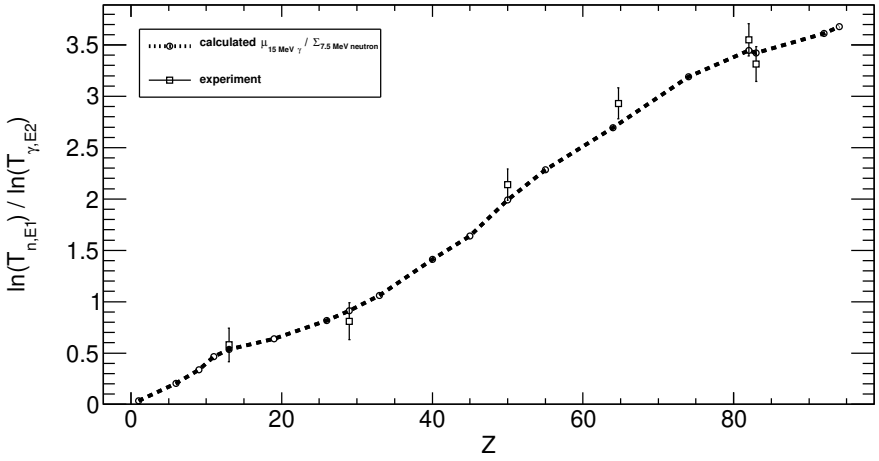

Figure 5.19: R_2: the ratio of the natural log of the measured transmission (T) of 15.1 to 7 MeV neutrons compared to the ratio of the mass-attenuation coefficient to the macroscopic cross section at those energies.

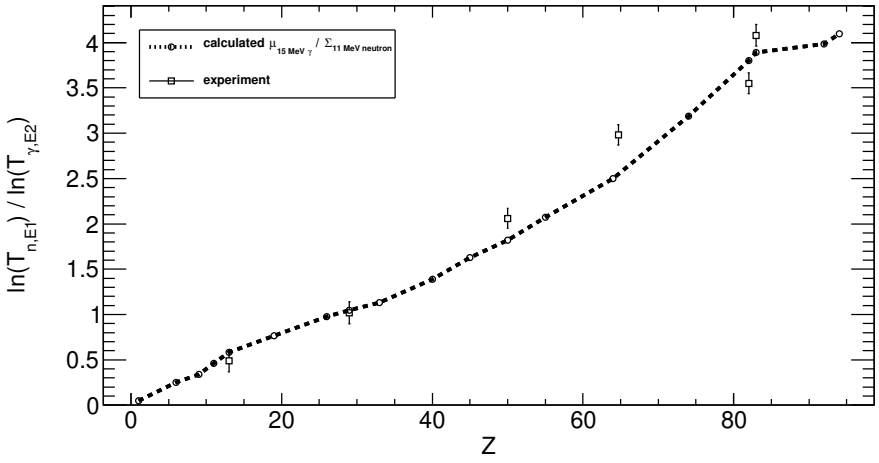

Figure 5.20: R_3: the ratio of the natural log of the measured transmission (T) of 15.1 to 11 MeV neutrons compared to the ratio of the mass-attenuation coefficient to the macroscopic cross section at those energies.

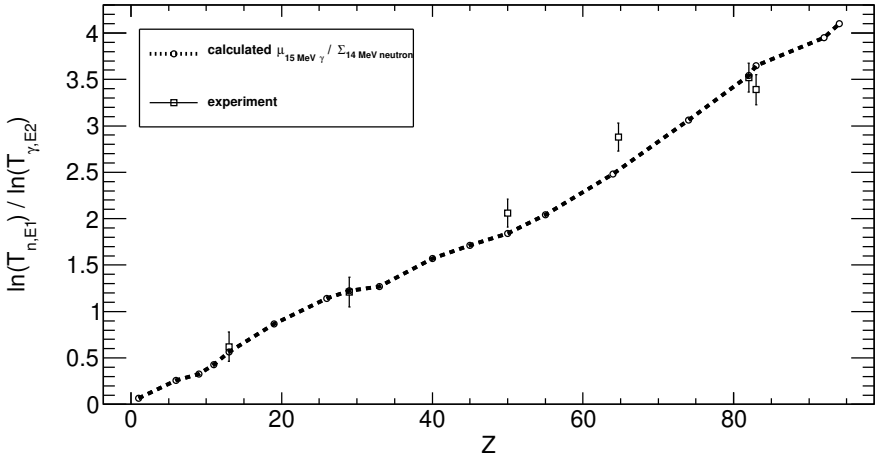

Figure 5.21: R_4: the ratio of the natural log of the measured transmission (T) of 15.1 to 14.5 MeV neutrons compared to the ratio of the mass-attenuation coefficient to the macroscopic cross section at those energies.

Each of the calculated R-values are assumed to be normally (Gaussian) distributed, where the mean and σ of each of the distributions are equal to the measured R-value and its respective σ. Take, for example, the measured R_1 for the Al object. The Gaussian distribution for this R would have values of 0.362 and 0.08 for the mean and sigma, respectively. Table 5.4 lists the means and uncertainties for each of the R-values. The calculated

Table 5.4: Measured R-values for all materials, where R_1 through R_4 is the ratio of μ/Σ for the following energies: $^{15.1\ \mathrm{MeV}}/_{4\ \mathrm{MeV}}$, $^{15.1\ \mathrm{MeV}}/_{7.5\ \mathrm{MeV}}$, $^{15.1\ \mathrm{MeV}}/_{11\ \mathrm{MeV}}$, and $^{15.1\ \mathrm{MeV}}/_{14.5\ \mathrm{MeV}}$.

Elememt	R_1	R_2	R_3	R_4
Al	0.36±0.08	0.58±0.16	0.49±0.12	0.62±0.16
Cu	0.89±0.07	0.81±0.18	1.02±0.122	1.2±0.16
Sn	2.0±0.07	2.15±0.15	2.06±0.11	2.06±0.15
W alloy	2.3±0.07	2.93±0.15	2.98±0.11	2.88±0.15
Pb	2.49±0.07	3.55±0.16	3.55±0.11	3.52±0.16
Bi	2.44±0.08	3.31±0.17	4.08±0.12	3.5±0.16

R-values are not continuous functions but are a series of discrete points. To determine Z, from a measured R, interpolation between discrete points is required. The projection of each of the R-values onto the horizontal axis gives a corresponding Z. Although the

uncertainty in R is symmetric, the corresponding uncertainty in Z is asymmetric and caused by the inconsistent variation of neutron attenuation across the periodic table.

To determine Z and its associated uncertainty from the discrete analytical R-values, Monte Carlo sampling is employed. A value is randomly sampled from the normal distribution of a single R. From the sampled value, a range (0–25, 25–50, 50–75, or 75–100) of Z is isolated. Then, Z is ascertained from the sampled R-value and a predetermined linear fit in the isolated Z-range and histogrammed. The sampling is repeated N times (N= 10^7). This Monte Carlo sampling is completed for each of the four R-values for each of the materials. An example of the results of the Monte Carlo sampling for the Z estimation of lead is shown in Fig. 5.22. A summary of the Z estimation for each of the R-values for all materials is listed in table 5.5; across all R-values agreement to the expected Z was within 3σ of the expected value.

Table 5.5: Estimation of element, denoted with its atomic number, for each $R_{n,\gamma}$.

Elememt	True Z	$Z(R_1)$	$Z(R_2)$	$Z(R_3)$	$Z(R_4)$
Al	13	12.1±2.76	15.7±4.6	11.9±3.0	14.4±3.6
Cu	29	28.0±1.4	26.9±3.7	28.5±3.4	29.2±5.3
Sn	50	49.4±1.4	54.6±3.2	57.3±3.1	57.5±5.0
W alloy	64.7	63.5±3.8	68.7±3.4	70.8±2.1	70.6±3.2
Pb	82	81.8±1.7	88.3±7.8	67.5±5.9	80.9 ±3.7
Bi	83	80.6±1.8	76.6±8.3	94.7±6.1	79.4±3.9

If the material is pure, an accurate weighted average of the four estimated atomic numbers can be calculated. The individual Z estimates are weighted with their corresponding uncertainty in R (σ_{R_i}), and the average Z is calculated using the following equation:

$$\overline{Z} = \frac{\sum_{n=1}^{4} \sigma_{R_i} Z_i}{\sum_{n=1}^{4} \sigma_{R_i}}. \tag{5.3}$$

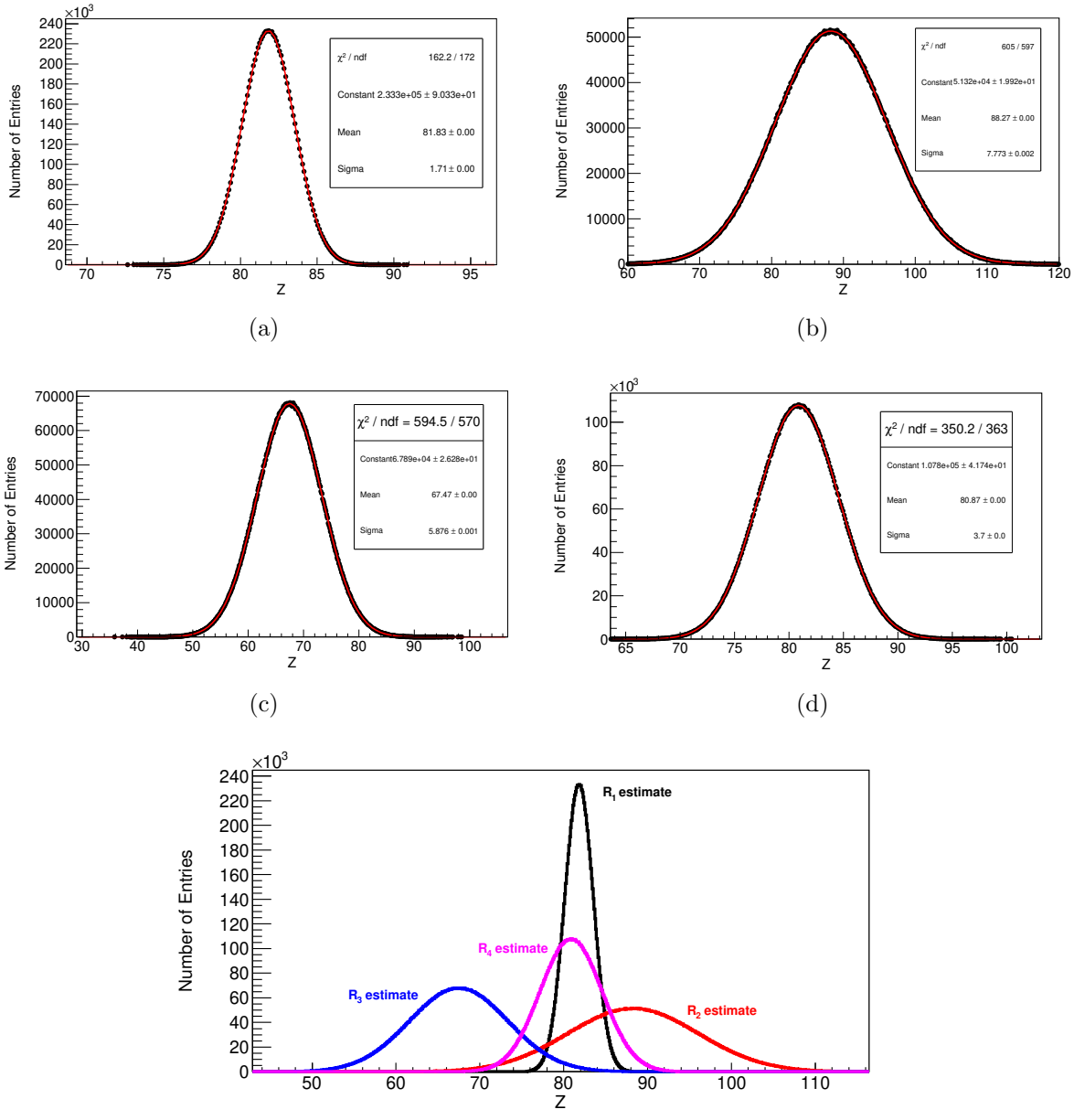

Figure 5.22: Estimations for lead, indicated by Z, using (a) R_1 (b) R_2 (c) R_3 (d) R_4 (Gaussian fit shown in red) and (d) all estimations overlaid.

The four Gaussian distributions corresponding to each of the R-values are sampled as previously discussed. The average of the four Z-estimates is calculated using equation 5.3 and histogrammed. This process is repeated for 10^7 times. The average Z estimation results for all materials are shown in Fig. 5.23 and demonstrate good agreement to the expected values. All objects return Z-values within 2σ of the expected element's atomic number. Table 5.6 summarizes the average Z estimate, where Z corresponds to the natural isotopic abundance of the element.

Table 5.6: Estimation of material, indicated by Z, using the weighted average of the four dual-mode material-discrimination factors.

Material	True Z	Measured Z
Al	13	12.79±1.77
Cu	29	28.17±1.31
Sn	50	51.77±1.62
W alloy	64.6	66.53±2.21
Pb	82	79.82±1.89
Bi	83	83.16±1.94

Some of the preliminary metrics are constructed based on a mixed (dual-mode) probe and show promise for improved material discrimination. Reconstruction of the elemental composition for various materials using dual-mode transmission radiography is successful. Figure 5.24 shows the calculated single- and dual-mode material discrimination metrics (R).

The improved discrimination capability of the $R_{n,\gamma}$-values compared to the pure gamma-ray ratio, R_γ, is qualitatively evident on Fig. 5.24. The total variation in the dual-mode R-values across the periodic table from H to U, is a factor of three or greater when compared to the single-mode R_γ. Table 5.7 lists the increase in variation for each of the dual-mode $R_{n,\gamma}$-values compared to R_γ. In each case, the combined neutron-γ ratios have a higher degree sensitivity compared to R_γ.

A closer examination of high-Z elements (Z>74) shows an order of magnitude im-

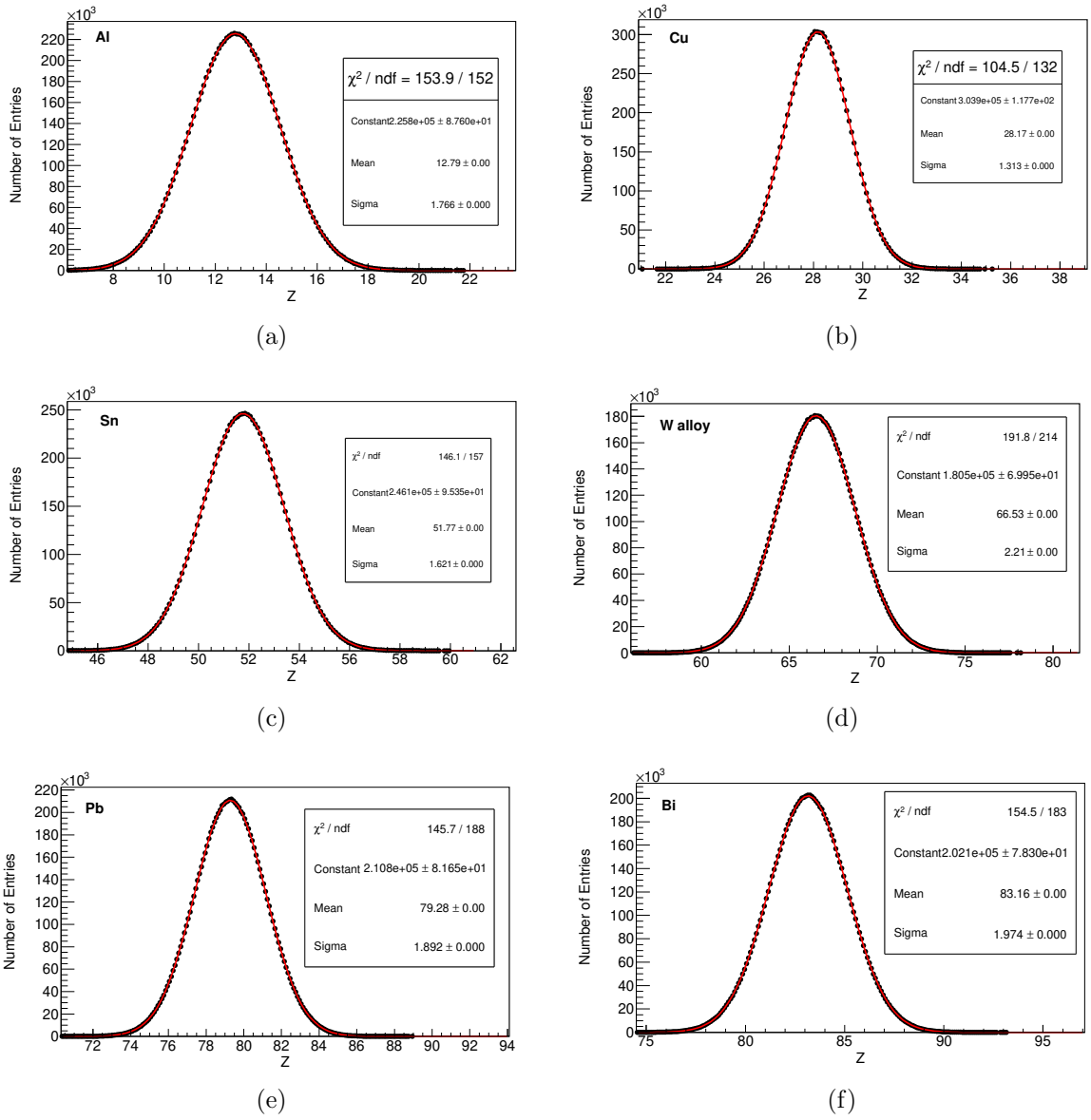

Figure 5.23: Estimation of element, indicated by Z, using the weighted average of four dual-mode R-values: (a) Al, (b) Cu, (c) Sn, (d) W-alloy, (e) Pb, and (f) Bi. Gaussian fit shown with solid line (red).

Table 5.7: Increase in variation of $R_{n,\gamma}$ over R_{γ} from hydrogen to uranium.

R-value (μ/Σ)	factor
$^{15.1\ \text{MeV}}/_{4\ \text{MeV}}$	3.28
$^{15.1\ \text{MeV}}/_{7.5\ \text{MeV}}$	4.04
$^{15.1\ \text{MeV}}/_{11\ \text{MeV}}$	4.47
$^{15.1\ \text{MeV}}/_{14.5\ \text{MeV}}$	4.44

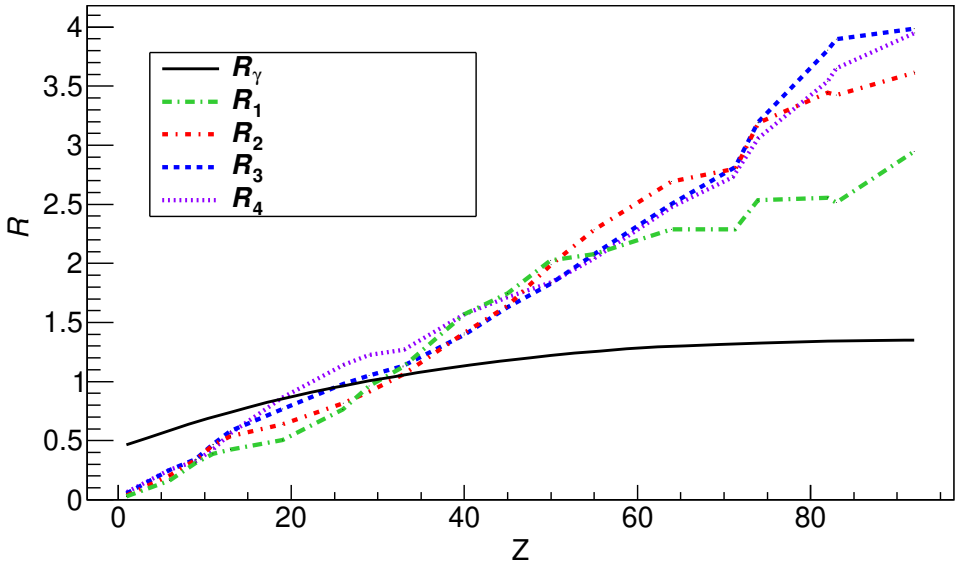

Figure 5.24: Single- versus dual-mode R-values.

provement of discrimination capability of the $R_{n,\gamma}$-values compared to the pure gamma-ray ratio, R_γ. Table 5.8 lists the increase in variation for each of the dual-mode $R_{n,\gamma}$-values compared to R_γ measured from tungsten to uranium.

Table 5.8: Increase in variation of $R_{n,\gamma}$ over R_γ for high-Z materials (tungsten to uranium).

R-value (μ/Σ)	factor
$^{15.1\ \mathrm{MeV}}/_{4\ \mathrm{MeV}}$	13.7
$^{15.1\ \mathrm{MeV}}/_{7.5\ \mathrm{MeV}}$	14.1
$^{15.1\ \mathrm{MeV}}/_{11\ \mathrm{MeV}}$	26.5
$^{15.1\ \mathrm{MeV}}/_{14.5\ \mathrm{MeV}}$	29.6

5.4 Summary

In previous work, fast-neutron (14.1 MeV) and gamma-ray (^{60}Co) radiography are combined to produce high resolution images [110]. The ^{60}Co gamma-ray energies (1.17 and 1.33 MeV), however, are not highly penetrating through dense objects. When performing

transmission radiography with any radiation, be it neutron or photon, there is an optimal transmission arrangement that gives the best material identification in a fixed time.

Attenuation of monoenergetic photons increases as a function of Z. At the right combination of thickness and density, any element can appear either opaque or transparent. The range of attenuation which can be accurately measured increases by probing with more neutron or photon energies. Further, due to the time-sensitive nature of certain nuclear security and nonproliferation applications, by performing multiple simultaneous measurements, shorter counting times are possible.

There is not one universal probe suited to neutron or photon radiography. There are instances where one type of probe or specific energy is more suited than another. This is evident in the in Table 5.9, where the estimated Z-values determined by the four individual $R_{n,\gamma}$-values, as well as their weighted average are listed. Some of the individual

Table 5.9: Summary of material estimation, denoted with its atomic number, for each $R_{n,\gamma}$.

Elememt	True Z	$Z(R_1)$	$Z(R_2)$	$Z(R_3)$	$Z(R_4)$	$\langle R \rangle$
Al	13	12.1±2.76	15.7±4.6	11.9±3.0	14.4±3.6	12.8±1.8
Cu	29	28.0±1.4	26.9±3.7	28.5±3.4	29.2±5.3	28.2±1.3
Sn	50	49.4±1.4	54.6±3.2	57.3±3.1	57.5±5.0	51.8±1.6
W alloy	64.6	63.5±3.8	68.7±3.4	70.8±2.1	70.6±3.2	66.5±2.2
Pb	82	81.8±1.7	88.3±7.8	67.5±5.9	80.9 ±3.7	79.8±1.9
Bi	83	80.6±1.8	76.6±8.3	94.7±6.1	79.4±3.9	82.2±1.9

R-values give a more accurate estimation of Z as compared to the $\langle R \rangle$. When element identification is judged across all objects, $\langle R \rangle$ is superior in both precision and accuracy for pure materials. $\langle R \rangle$ has a residual sum of squares (RSS) which is a factor of two or more lower than any other R-value and a mean absolute error (MAE) which is the lowest of all R metrics. Table 5.10 lists the RSS and MAE values for each of the R discriminants. If, however, the material is a mixture, the $\langle R \rangle$ may be misleading to the actual combination of the object.

Table 5.10: RSS values for each of the R-factors.

R-value	RSS	MAE
R_1	68.8	2.14
R_2	120.3	5.2
R_3	402.1	3.9
R_4	72.9	4.1
$\langle R \rangle$	32.4	1.8

Probing an object with multiple particles and energies provides a wealth of information. Figure 5.26 and Fig. 5.25 show the calculated single-mode and dual-mode material determination R-values and the calculated R-values for two shielded uranium scenarios. The uranium (1.1-cm thick) is shielded with 10 cm of low density polyethylene (LDPE) (Fig. 5.25) and then with 10 cm of iron (Fig. 5.26). For an object consisting of a single element with natural isotopic abundance, all R-values would lie on (near) the same vertical line. Any deviation from a vertical line indicates that the object does not consist of a single element in natural isotope concentration, or that multiple layers of different elements are present. In each of the shielded uranium cases, the R values indeed do not fall on a vertical line. The spread in the R-values for the shielded uranium therefore successfully provides an indication that the object does not consists of a pure element, but is rather a mixture or multiple elements or layers of pure elements. This result could aid in anomaly detection and indicate information about possible shielding in the AI beam's path. By using multiple metrics – multiple R-values – these combinations of materials and shielding are easily discernible. As a natural extension of this method, it is possible to form hypotheses of the composition of materials and thicknesses of shielded objects and check for their consistency with multiple discriminants R, arriving with the best interpretation.

The deuteron-BN source may offer advantages over the natural boron target used in Refs.[31–33]. The additional gamma-ray energies of 10.8, 9.2, 8.3, 6.3, and 5.3 MeV,

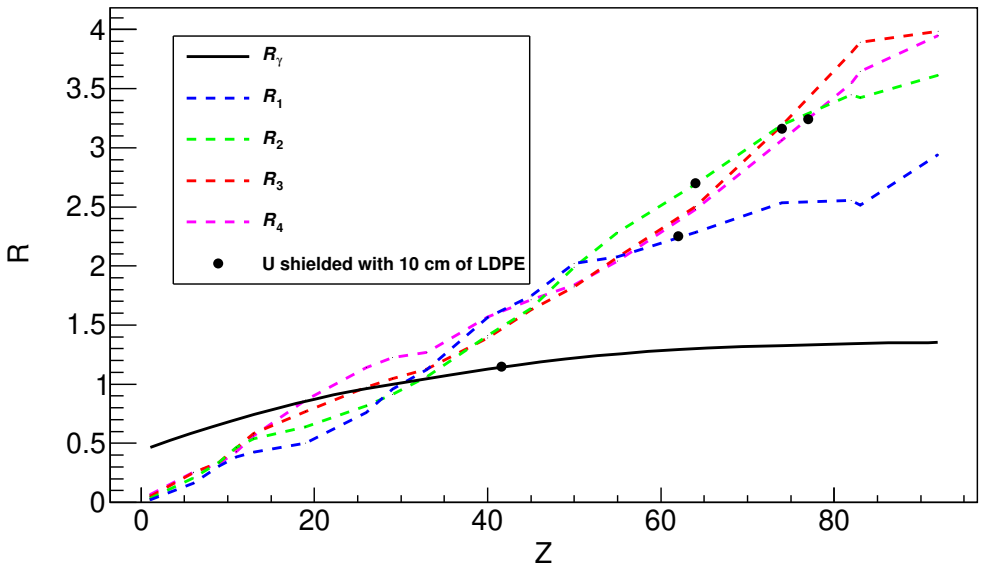

Figure 5.25: Single-mode versus dual-mode R-values and the R-values calculated uranium shielded by 10 cm of LDPE.

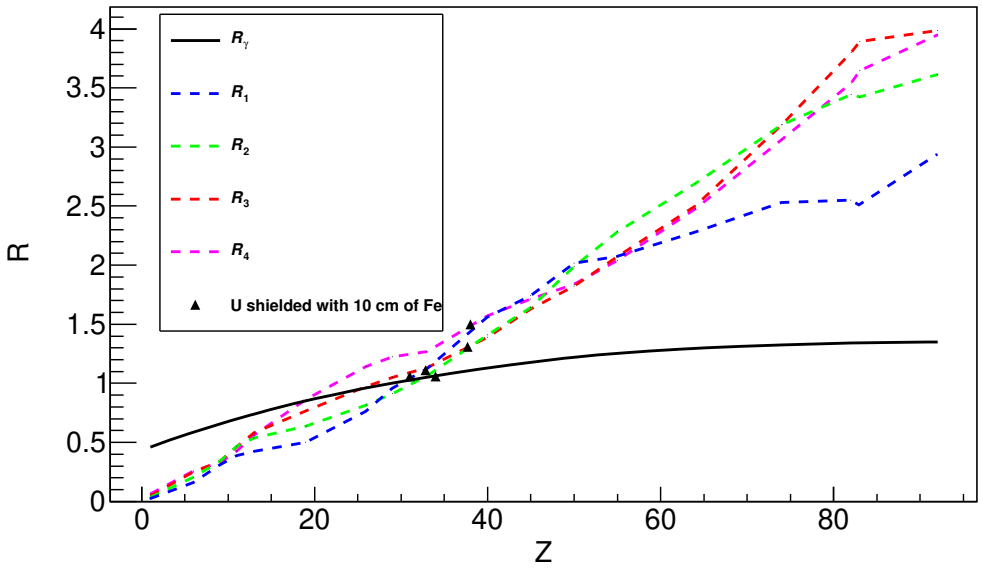

Figure 5.26: Single-mode versus dual-mode R-values and the R-values calculated uranium shielded by 10 cm of iron.

provide more energies to probe a larger range of attenuation. Figure 5.27 shows the analytically calculated ratio of attenuation coefficients for gamma-ray energies produced

by the deuteron-BN source. Similar to the multiple dual R-values established, multiple single-mode gamma-ray radiography attenuation ratios could be used to probe a broader ranges of material-thickness compositions. One could imagine 92 different equations based on particle attenuation, which would give one absolute material characterization. This would be particularly useful when applied to composite objects, where the particle beam passes through multiple different materials of varying thicknesses.

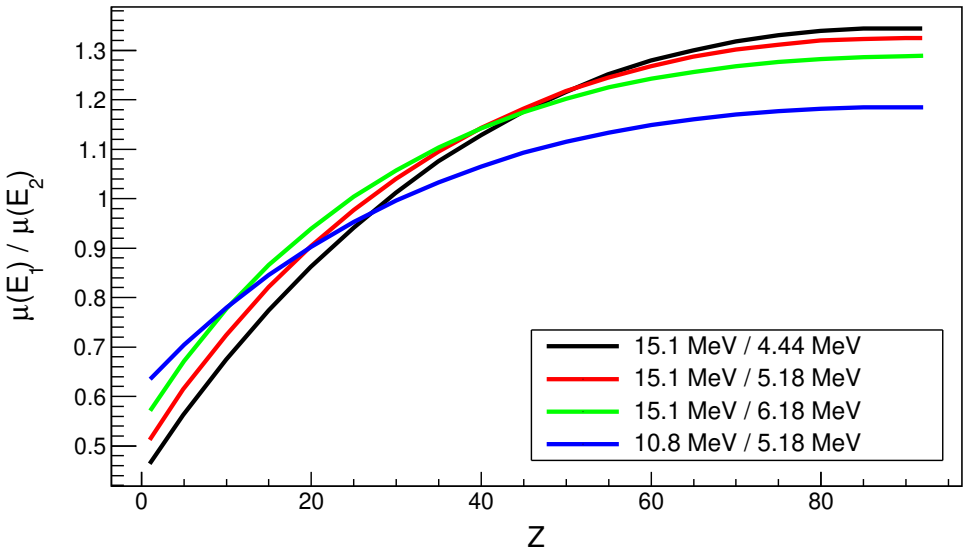

Figure 5.27: Analytically calculated attenuation ratios based on tabulated nuclear data for various photon pairs produced during deuteron-BN source.

By measuring the neutron TOF, the incident neutron energy spectrum can be determined. If the neutron light output distribution contains sufficient features, unfolding algorithms can be utilized to perform neutron spectroscopy without TOF. This would be very advantageous to time-constrained applications by potentially reducing experimental time. The EJ-309 detector may not be the ideal detector to use for neutron spectrum unfolding. Detectors that deliver more prominent features in their respective light output distributions such as deuterated liquids or solids[111–113] or capture-based detectors [114] could result in improved neutron spectrum deconvolution.

Chapter 6

Fissionable material identification

Up to this point, two radiography methods have been discussed as a means to penetrate different types of shielding and identify unknown materials. These approaches have their limitations and are sensitive to varying combinations of material types and thicknesses, but are adequate to detect the presence of high-Z materials such as SNM. The most dependable signature of SNM in an AI system, however, is the emission of characteristic neutrons and photons from induced fission with expected energy and time characteristics and correlations. The existence of neutrons and gamma rays, however, does not necessarily indicate the presence of SNM, since they may be produced by other energetic processes in an AI system. In contrast, the time structure of neutrons and photons emitted from induced fission provides a clear, unique indicator of SNM.

In this chapter, the measurement of the buildup and decay of the β-delayed neutron rate during and following the pulsing of an AI source is presented as a method to confirm the presence of SNM. The technique can be used in conjunction with either single- or dual-mode radiography as the final decision point to determine the presence of SNM. Additionally, a new method is presented to categorize fissionable material by determining the uranium enrichment. The method uses a custom-designed scintillation detector as an alternative to ^{3}He for β-delayed neutron detection and requires no calibration stan-

dards. This method exploits the differences in yield and lifetimes of long-lived delayed neutron groups to determine uranium enrichment. While the experiment used capture-based neutron detectors and a compact neutron generator, the described technique is independent of the detector type and AI source. This chapter includes edited portions of the 2018 publication in the journal Physical Review Applied, *Discriminating uranium isotopes using the time-emission profiles of long-lived delayed neutrons* [115].

6.1 Introduction

Fission neutrons are produced in two time domains, prompt and delayed. The observation of delayed neutrons from fission is a well-established means for detecting fissionable materials [31, 116–119]. Decay of fission products results in emission of delayed neutrons on a distinct, predictable characteristic decay timescale ranging from hundreds of milliseconds to tens of seconds. An important drawback of the delayed neutron signature is its low intensity, significantly below prompt neutron and γ-ray emission [42]. To establish the necessary signal time structure and increase the delayed neutron signal intensity, pulsed AI sources are needed.

Characteristic β-delayed neutrons are commonly classified into several groups based on their respective precursors' lifetimes. These groups exhibit characteristic absolute yields and energy spectra, unique to the isotope and the inducing particle's type and energy. Methods used to date have exploited the short-lived delayed neutron groups to perform isotopic identification [117]. In other prior work, isotopic concentrations in pure uranium and mixed Pu-U samples were determined through the measurement of the decay of long-lived β-delayed neutron rate following irradiation [120–122]. When using a pulsed AI source, measurement of the delayed neutron time emission during irradiation is also possible, which we refer to as buildup, and provides complementary information

regarding the interrogated material. Figure 6.1 illustrates the two delayed-neutron rate signatures induced by a repetitively pulsed AI source.

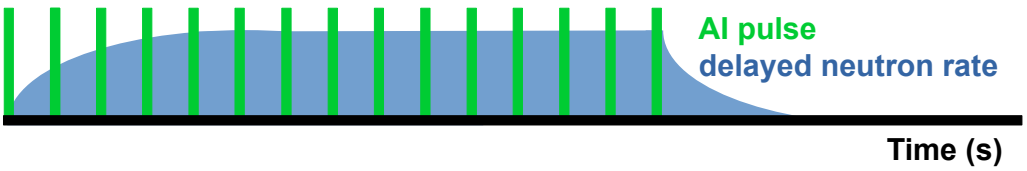

Figure 6.1: Depiction of the buildup and decay of the delayed neutron rate when using a pulsed AI source.

However, to date measurement of the long-lived buildup of β-delayed neutron emission has not yet been used to determine the isotopic concentration of uranium or any other mixed fissile material sample. Further, no other detector types other than ^{3}He have been used for fissile isotopic determination based on long-lived delayed neutron emission. Additionally, with the dwindling supply of ^{3}He [123] there is a significant interest in developing alternative neutron detectors and understanding their performance in nonproliferation applications.

In our prior work, we reported on the observation of β-delayed neutrons from fission of uranium induced by a dual radiation AI source based on the ^{11}B(d,nγ)^{12}C stripping reaction [118]. In those experiments, the characteristic buildup and decay of delayed neutron emission from ^{238}U was measured. A radiofrequency quadrupole accelerator drove the source, producing a quasi-monoenergetic mixed neutron/gamma radiation. We demonstrated the detection of fissionable material based on the measurement of delayed neutron emission, which uses a method that may be also be suitable for reliable isotopic identification. Figure 6.2 shows the delayed neutron buildup between the accelerator pulses and its fit to nuclear data using the characteristic six delayed neutron groups. The

subsequent β-delayed neutron decay following accelerator operation is shown in Fig. 6.17.

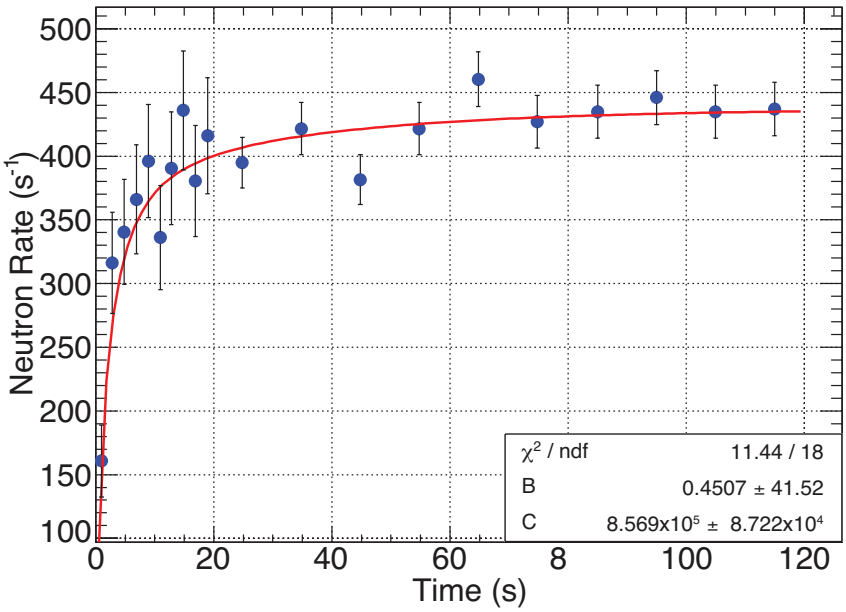

Figure 6.2: Delayed neutron buildup between accelerator pulses with fit to nuclear data shown in red [118].

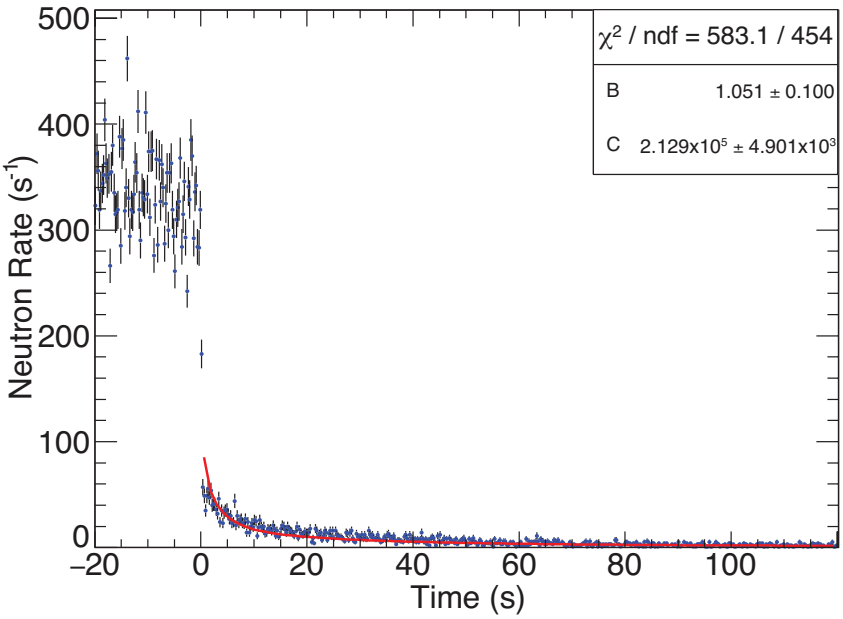

Figure 6.3: Delayed neutron decay after 300 seconds of accelerator operation with fit to nuclear data shown in red [118].

This chapter extends those measurements to HEU, with a goal to demonstrate a capability

to also measure the isotopic composition of the material from the differences in the shape of the delayed neutron time-emission profile.

6.2 Materials and methods

The experiment was performed over a two-day period at the Device Assembly Facility (DAF), Nevada National Security Site. Measurements were performed on three different spherical metal objects: tungsten, DU, and HEU. The object masses were 14.7 kg, 12.8 kg, and 13.8 kg, respectively. Due to constraints on the available materials and possible geometric configurations, it was not possible to use the same masses for all test objects.

The HEU object was a series of connecting concentric hemispheres of HEU known as the Rocky Flats shells, which have a bulk density of 18.664 g/cm^3 and an isotopic content of 93.16% ^{235}U, 5.35% ^{238}U, and less than 2% of other isotopes of uranium [124]. The HEU object consisted of shells 01–24 arranged in a spherical configuration. A photograph of the HEU object is shown in Fig. 6.4.

The HEU, DU, and tungsten objects were interrogated with 14.1-MeV neutrons produced by a DT generator (Thermo Scientific model P211), with an approximate isotropic yield of 10^8 neutrons/s. Each object was placed at a distance of 13 cm, as measured from the center of the object to the neutron-generating target in the DT generator. The detector was placed on the side of the object opposite from the neutron source. The front face of the detector was located 12 cm from the center of the object. The DT generator was operated at a pulse rate of 100 Hz for all measurements with a beam-bunch width of approximately 10 µs.

The detector used in these measurements was the custom-built heterogeneous composite scintillator described in Chapter 2. The detector is solid-state which is often preferred over liquid or gaseous detectors. The intrinsic efficiency was calculated by Monte Carlo

(a) (b)

Figure 6.4: (a) The interconnecting hemispheres and (b) full spherical configuration of the HEU object constructed from the Rocky Flats shells placed atop an aluminum hollow cylinder.

simulation for delayed neutrons from ^{235}U and ^{238}U fission, similar to method described in Ref. [118], and yielded approximately 15% for each isotope. Additionally, the detector has a simulated intrinsic efficiency of 7.8% for ^{252}Cf fission neutrons.

Based on Monte Carlo simulation, the composite scintillator discussed here has a higher intrinsic efficiency for fission neutrons from ^{252}Cf at 8% versus 6%, a typical value for a ^{3}He detector [125]. Additionally, the detector has approximately double the intrinsic efficiency for delayed neutrons from the fast fission of ^{235}U and ^{238}U compared to a traditional ^{3}He detector.

Another benefit of the detector used in this work compared to ^{3}He is the average time it takes for a neutron to capture in the detector. In a ^{3}He detector, the innermost volume containing the ^{3}He gas is typically surrounded by hydrogenous material that thermalizes incident neutrons, resulting in certain distribution of neutron time-to-capture on ^{3}He. When measuring the delayed neutron buildup from fission, such as in the AI experiment described in this chapter, an ideal detector would have the shortest average time-to-capture. The time-to-capture dictates the maximum operating repetition rate

of the AI source. An increase of the repetition rate typically results in a higher overall induced fission rate and thus a stronger delayed neutron signature. Figure 6.5 shows the Monte Carlo simulation of the neutron time-to-capture distribution for fission neutrons from a ^{252}Cf source for the composite detector and the ^{3}He capture detector described in Ref. [126]. The average time-to-capture is 22 and 12 µs for the ^{3}He detector and composite detector, respectively. An AI system designed to detect long-lived delayed neutrons using the composite detector would permit a higher repetition rate AI source in comparison to a system that employs traditional ^{3}He detectors.

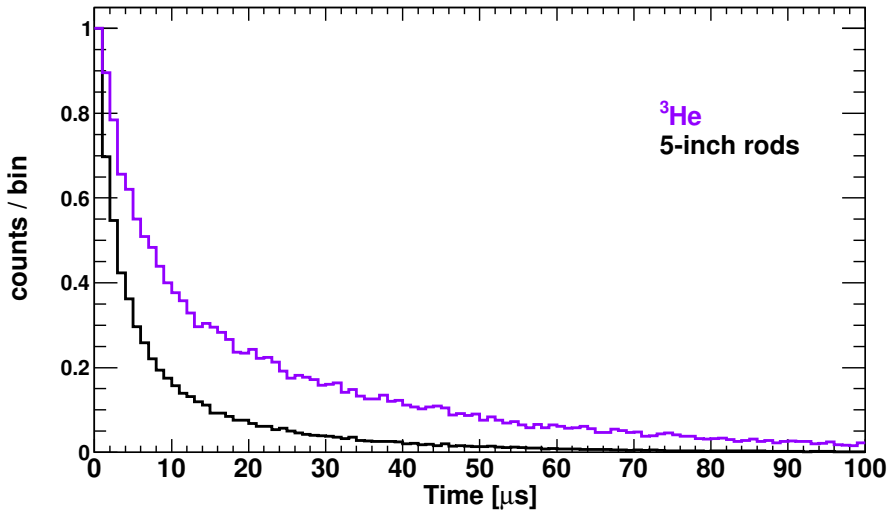

Figure 6.5: Monte Carlo Simulation of the time-to-capture for the 12.7 cm composite neutron detector (5 in. rods) and a ^{3}He capture detector.

The composite detector was coupled to a Hamamatsu R6527 photomultiplier tube (PMT) and powered using a CAEN DT5533 high-voltage power supply. The PMT anode output signals were collected and digitized using a CAEN DT5730 14-bit 500 MHz desktop waveform digitizer. CAEN's DPP PSD Control Software and DPP PSD firmware were used to collect and store data on a computer for post-processing [96]. A short-gate integral (Q_{short}) and a long-gate integral (Q_{long}) are recorded for each waveform as the basis for pulse-shape discrimination. The integration bounds were optimized prior to the

experiment at t_s=34 ns for Q_{short} and t_s=150 ns for Q_{long}, where t_s is the start time of the waveform as identified by the trigger from CAEN DPP PSD firmware. The t_s was offset by 6 ns prior to the trigger on the leading edge of the pulse. Figure 6.6 shows a typical pulse shape from a neutron-capture event on ^{6}Li-glass and an event occurring in the PVT of the composite scintillation detector. The two distinct pulse shapes are readily visible and easily distinguished.

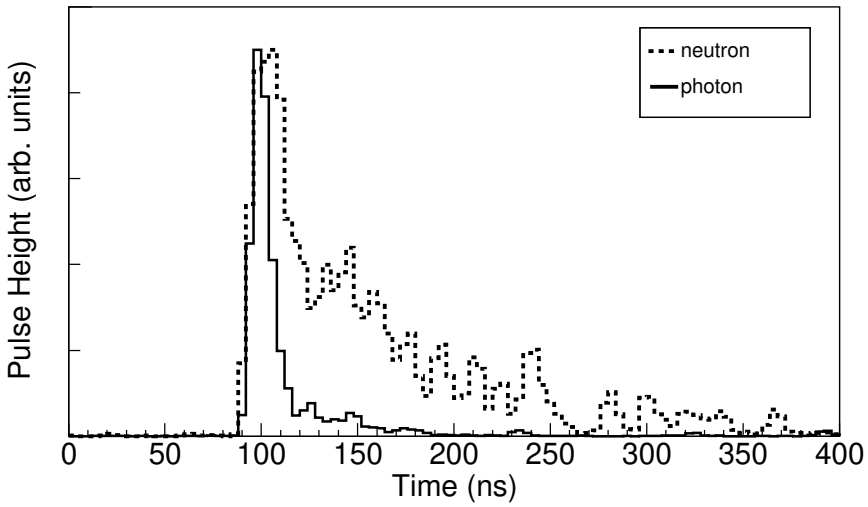

Figure 6.6: Representative pulse shapes from a neutron-capture event on ^{6}Li-glass and an event occurring in the PVT of the composite scintillation detector.

To measure the delayed neutron time profile for each object, detector data were recorded during a series of on-off cycles of the neutron generator. In each cycle, the generator was turned on for 30 seconds, then turned off for one minute. One measurement run consisted of ten on-off cycles, lasting about 15 minutes in total. Three such measurements were taken for both the HEU and DU targets, and one was taken for tungsten. The on-off cycles were summed for final analysis. Two five-minute background measurements were also recorded, one with the HEU target in place, and the other with the DU target. Calibration measurements were performed using ^{137}Cs and Am-Be sources. A photograph of the experimental setup is shown in Fig. 6.7.

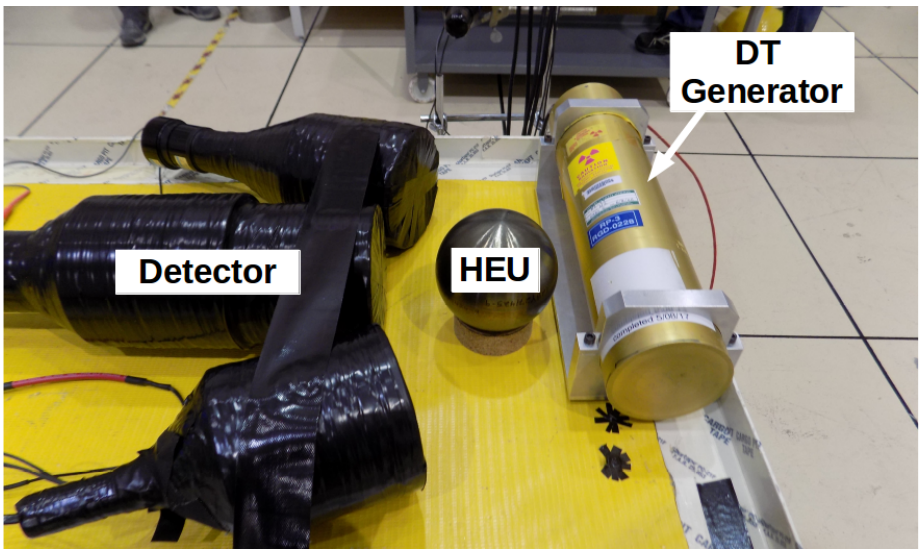

Figure 6.7: Experimental setup including the composite detector coupled to the PMT, the HEU object, and the DT generator.

6.3 Results & Discussion

Figure 6.8 shows the PSP-light output distribution for 15 minutes of on/off cycles of the DT generator interrogating a HEU object. The charge integration method is used to obtain the pulse-shape parameter (PSP) as follows:

$$PSP = (Q_{long} - Q_{short})/Q_{long}. \tag{6.1}$$

Neutron capture events are localized near PSP=0.55 and light output of approximately 0.28 MeVee. A calibration measurement using a Pu-Be source are used to establish a cut around the neutron-capture region, where events within the cut were accepted as neutrons. A Gaussian function is fit in both dimensions to the neutron region centered at a PSP of 0.55 and light output of 0.28 MeVee in Fig. 6.8, and a 3σ cut used to establish the neutron capture region.

Two different long-lived β-delayed neutron signatures were measured. The first was the buildup of delayed neutron emission measured between the generator pulses; the

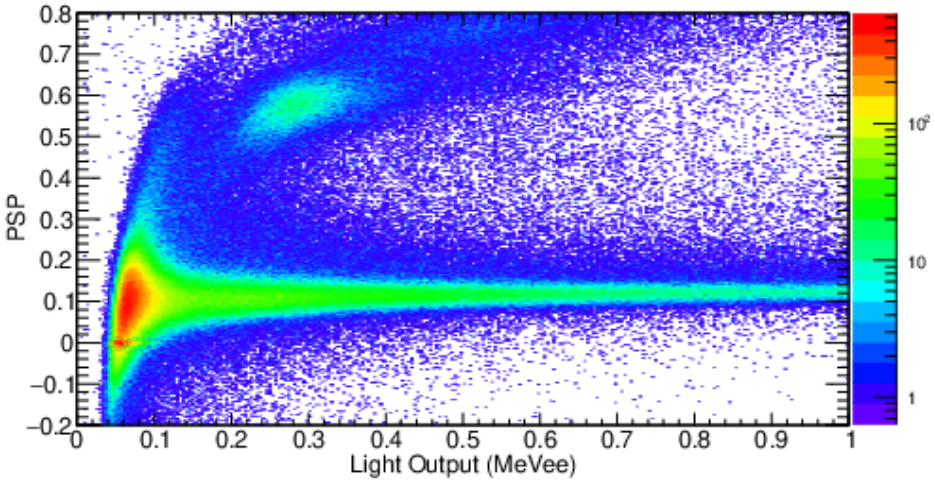

Figure 6.8: PSP versus light output from the composite detector for the HEU object interrogated by 14.1 MeV neutrons.

second was the decay of the delayed neutron emission measured immediately after the generator had been turned off. The time profile of these two delayed neutron signatures is parametrizable in analytic form using the available nuclear data and depends on the enrichment of the uranium sample. The buildup of delayed neutron emission is described in the framework of six delayed neutron groups by

$$R_b(t) = B + C \sum_{i=1}^{2} \sum_{j=1}^{6} f_i P_i Y_{i,j} \epsilon_{i,j} \left[1 - \exp(-t/\tau_{i,j})\right], \tag{6.2}$$

where $R_d(t)$ is the detected buildup of delayed neutron emission, B is the constant neutron background rate, C is a scaling constant, index i corresponds to the uranium isotope (^{235}U or ^{238}U), index j represents the delayed neutron group number, f_i is the 14-MeV neutron-induced fission probability of uranium isotope i, P_i is the isotopic percentage of uranium isotope i, $\epsilon_{i,j}$ is the detector efficiency for delayed neutron group j of uranium isotope i, $\tau_{i,j}$ is the decay constant for delayed neutron group j of uranium isotope i, and $Y_{i,j}$ is the delayed neutron yield per fission for group j of uranium isotope i. Similarly, the decay

Table 6.1: ^{235}U delayed neutron parameters.

Group	$Y(\%)$	ϵ_C	$T_{1/2}$ (s)
1	0.063	0.163	54.5
2	0.351	0.151	21.8
3	0.310	0.150	6.00
4	0.672	0.149	2.23
5	0.211	0.149	0.496
6	0.043	0.148	0.179

of delayed neutron emission can be expressed as

$$R_d(t) = B + C \sum_{i=1}^{2} \sum_{j=1}^{6} f_i P_i Y_{i,j} \epsilon_{i,j} \\ [\exp(t_b/\tau_{i,j}) - 1] \exp(-t/\tau_{i,j}), \tag{6.3}$$

where t_b is the period over which the constant-intensity AI beam is turned on [118].

A Monte Carlo simulation was performed using `Geant4` version 10.4 to estimate the intrinsic delayed neutron detection efficiency for the composite detector [70]. The energy spectra for the individual groups for ^{235}U and ^{238}U were simulated and intrinsic neutron detection efficiencies calculated on a group-by-group basis. Prior reported energy spectra for the six delayed neutron groups of ^{235}U and ^{238}U in Ref. [127] were used in the simulation.

The yields (Y), efficiencies (ϵ_C), and the half-lives ($T_{1/2}$) for the six delayed neutron groups are listed in Table 6.1 and Table 6.2 for ^{235}U and ^{238}U, respectively [128]. These efficiencies were used in the parameterizations of the buildup and decay delayed-neutron rate.

`MCNP` was used to simulate the build up and decay of the delayed-neutron rate from neutron-induced fission of ^{235}U and ^{238}U to validate the parameters used in Equations (6.2) and (6.3). An isotropic 14.1-MeV neutron source of 10^8 neutrons per second was evenly distributed over 10 µs. A series of connecting concentric hemispheres of uranium with

Table 6.2: ^{238}U delayed neutron parameters.

Group	$Y(\%)$	ϵ_C	$T_{1/2}$ (s)
1	0.054	0.163	52.4
2	0.564	0.148	21.6
3	0.667	0.153	5.00
4	1.599	0.151	1.93
5	0.927	0.151	0.490
6	0.309	0.150	0.172

a geometric dimensions equal to that of the HEU object used in the experiment served as the interrogated objects. A simulation of a pure ^{235}U object and then a pure ^{238}U object was conducted. The neutrons leaving the uranium sphere after 11 µs were then tallied. The time offset ensured that only delayed neutrons were counted. The 11 µs was selected based on the observed neutron die-away in the simulation. The results from the simulation are shown in Fig. 6.9.

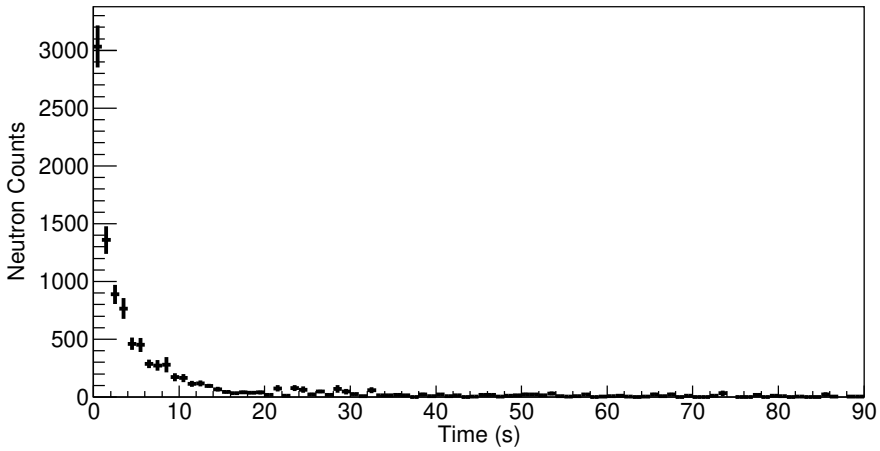

Figure 6.9: `MCNP` result of tallied neutron counts after 11 µs resulting from an isotropic 14.1-MeV neutron source of 10^8 neutrons per second was evenly distributed over 10 µs bombarding pure ^{235}U concentric hemispheres.

To build the model for 30 s of irradiation, the time distribution was from Fig. 6.9 is assumed to be produced at every second for 30 s and added. Figure 6.10 displays a visual aide as to how the full neutron time distribution was calculated. Figure 6.11 shows the

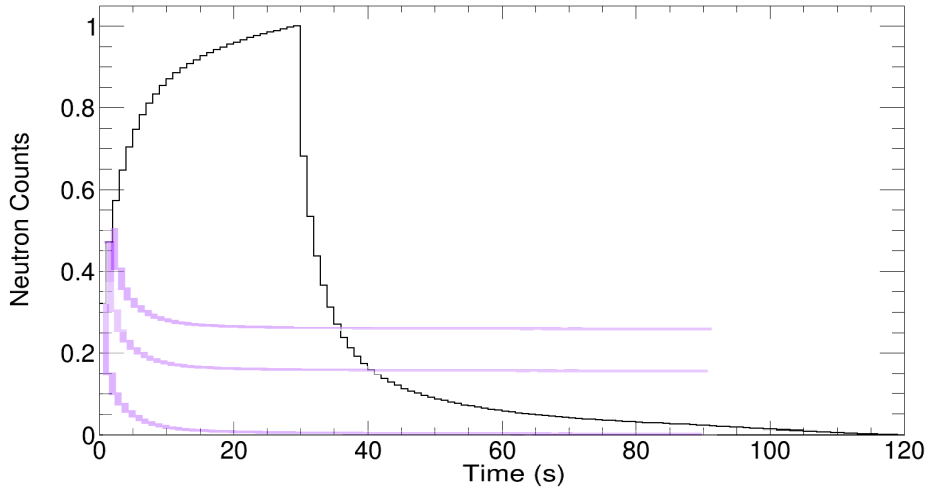

Figure 6.10: Visual aide to demonstrate the calculation of the full neutron time distribution during 30-s, 14.1-MeV neutron irradiation and following irradiation. The purple line is the neutron rate from the MCNP simulation in Fig. 6.9 and the black line is neutron time distribution by adding the individual neutron time distribution in increments of 1 second.

simulated delayed neutron buildup and decay for 30 s of 14.1 MeV neutron irradiation of ^{235}U and ^{238}U.

Equations (6.2) and (6.3) provide an analytical means to explore the enrichment-dependent time behavior of the two delayed neutron signatures. Figure 6.12 shows the simulated buildup and decay time emission of delayed neutrons for a pure sample of ^{235}U and a pure sample of ^{238}U with $t_b = 30$ s. A qualitative inspection of Figure 6.12 reveals an exploitable difference between the shapes of the two pure samples of uranium for both the delayed neutron buildup and decay time distributions.

A simple metric can be defined on the basis of the difference in the delayed neutron emission profile for ^{235}U and ^{238}U and used to quantify the enrichment. The metric is based on the ratio of the total number of detected neutrons in two separate time periods over which the delayed neutron emission is measured and may be applied to both

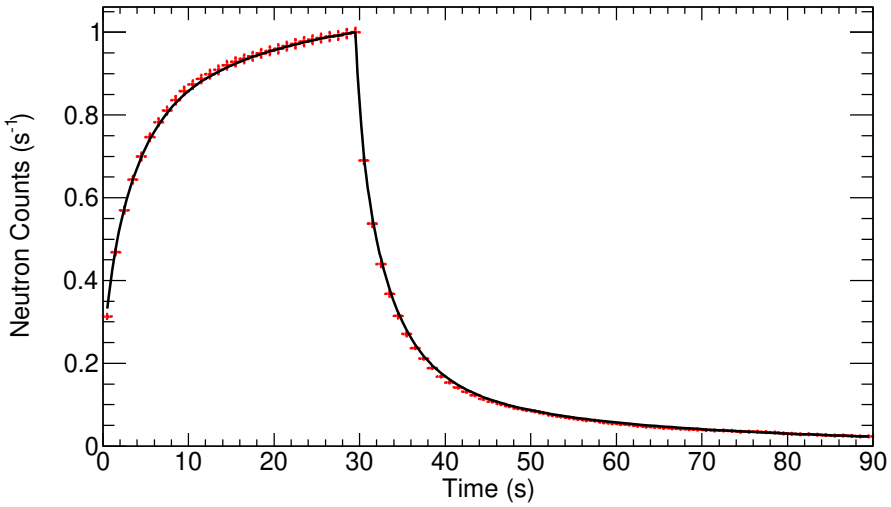

(a)

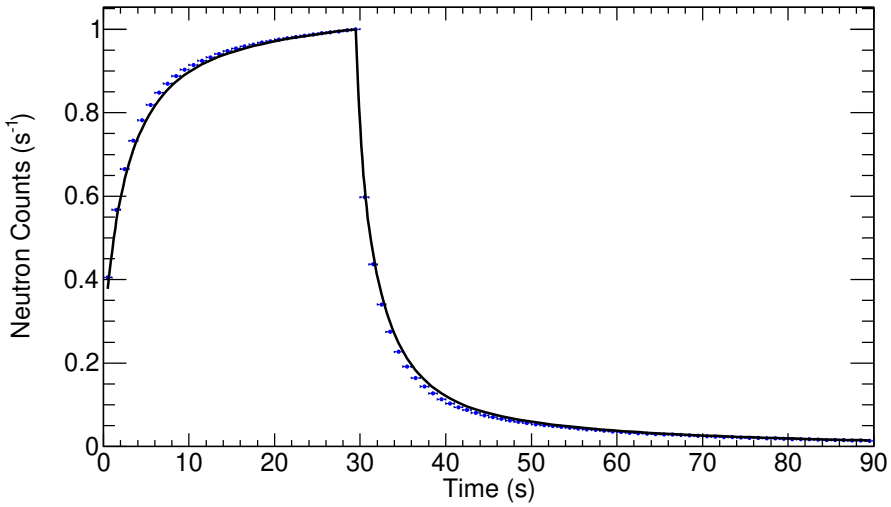

(b)

Figure 6.11: Simulated full time distribution of delayed neutrons during 30 s 14.1-MeV neutron irradiation and following irradiaiton for (a) for a pure ^{235}U sample (red) and (b) a pure ^{238}U sample (blue). The black line is not a fit to simulated data but is the analytically calculated rate based on equations (6.2) and (6.3).

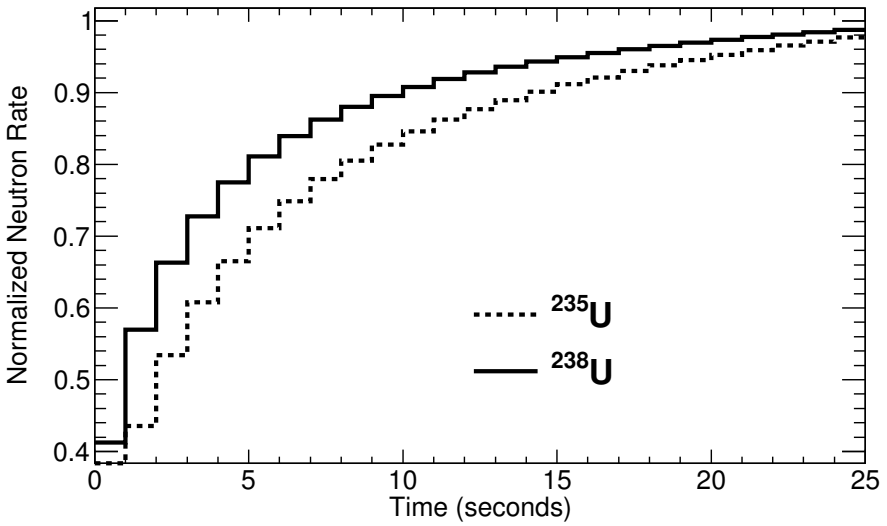

(a)

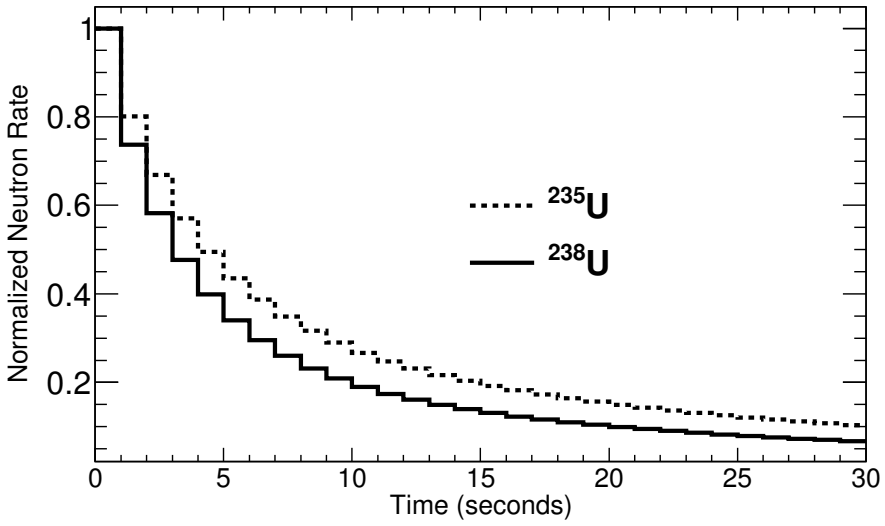

(b)

Figure 6.12: Analytically-calculated long-lived (a) buildup and (b) decay of delayed neutrons for a pure ^{235}U sample and a pure ^{238}U sample.

the buildup and the decay time distribution. The metric is denoted by F and can be calculated using the following relationship:

$$F = N_1/N_2, \tag{6.4}$$

where N_1 and N_2 are the total number of counts within two chosen time periods, A_1 and A_2, as illustrated in the example shown in Fig. 6.13, where decay time profiles for pure samples of ^{235}U and ^{238}U immediately after the neutron generator is turned off are shown. The same methodology is applicable to the buildup of long-lived delayed neutron emission.

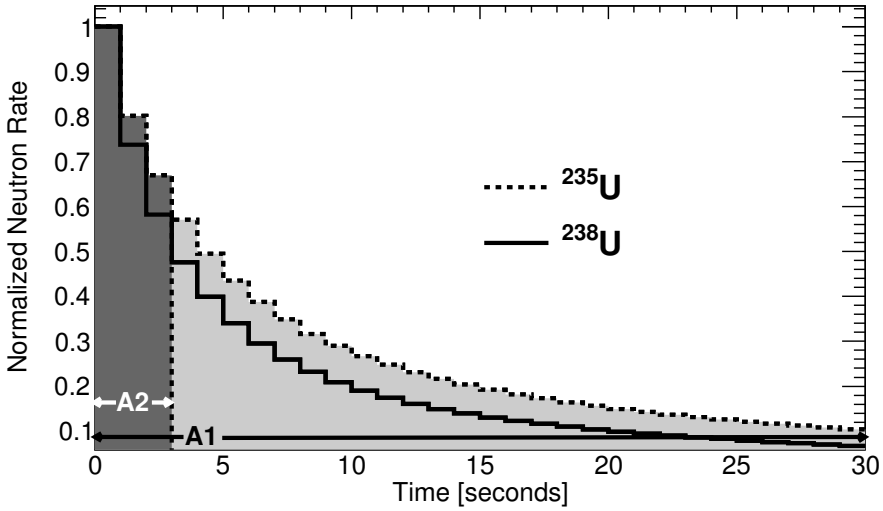

Figure 6.13: The use of A_1 and A_2 limits for calculation of the ratio F. Long-lived delayed neutron decay from neutron induced fission after accelerator operation for pure samples of ^{235}U and ^{238}U is shown.

A measure of distinguishability, D, can be defined that takes into account the mean values of the detected neutron counts in two time periods (F) and their standard deviations (σ):

$$D = \frac{|F_{235} - F_{238}|}{\sigma_{235} + \sigma_{238}}, \tag{6.5}$$

where F is defined by Eq. (6.4) and σ is the standard deviation of F, while subscripts denote the two major isotopes of U. Since D depends not only on the characteristics of delayed neutron emission, but also on the counting statistics, the optimum start and stop times for A_1 and A_2 depend on the number of detected neutron counts, which is affected by system efficiency and measurement time.

Figure 6.14 shows the buildup of delayed neutrons between accelerator pulses for HEU and DU. The six-group delayed neutron buildup model defined in Equation (6.2) is fitted to the measured buildup data for each isotope, and is shown as a red line in Figure 6.14.

The period during which neutrons were produced by the DT generator was determined from the event rate recorded by the detector. The total event rate was monitored in 10-µs increments. When the total number of events in a 10-µs increment increased above twenty, the start of a new neutron generator pulse was marked. The twenty-event threshold was set empirically, based on the average number of counts observed in 10-µs increments when the generator was operating. The 10-µs increment was chosen to match the pulse duration of the generator.

To allow for neutron die-away, events occurring within 4.5 ms following a generator pulse were disregarded. The neutron events occurring in the remaining 5.5 ms preceding the next generator pulse were used to measure the delayed neutron buildup. Figure 6.15 shows the summed neutron rate for approximately fifteen minutes of generator operation with a HEU test object. The neutron die-away is apparent in the approximate period of 0–4.5 ms. Figure 6.16 illustrates the period between generator pulses within which neutron events were selected to measure the delayed neutron buildup and the prompt die-away region, where events were rejected.

Figure 6.17 shows the decay of delayed neutrons after the accelerator is turned off for HEU and DU. The six-group delayed neutron decay model defined in Eq. (6.3) is fitted

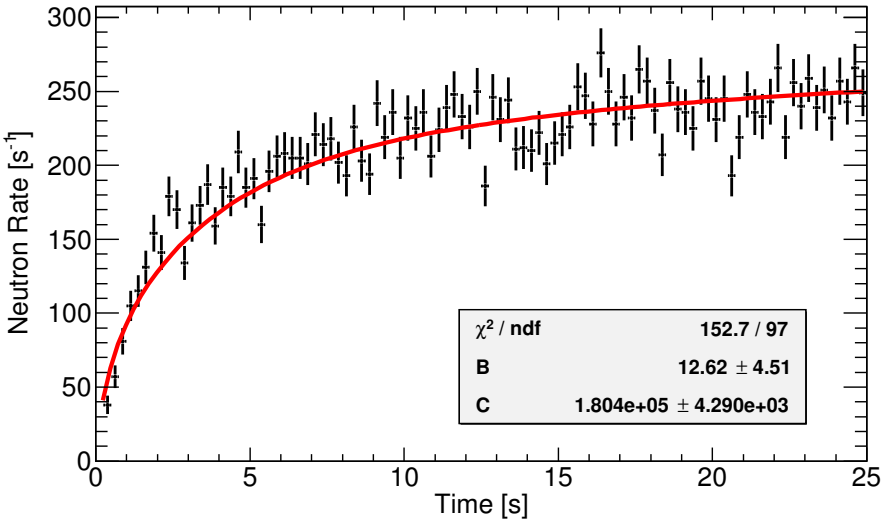

(a)

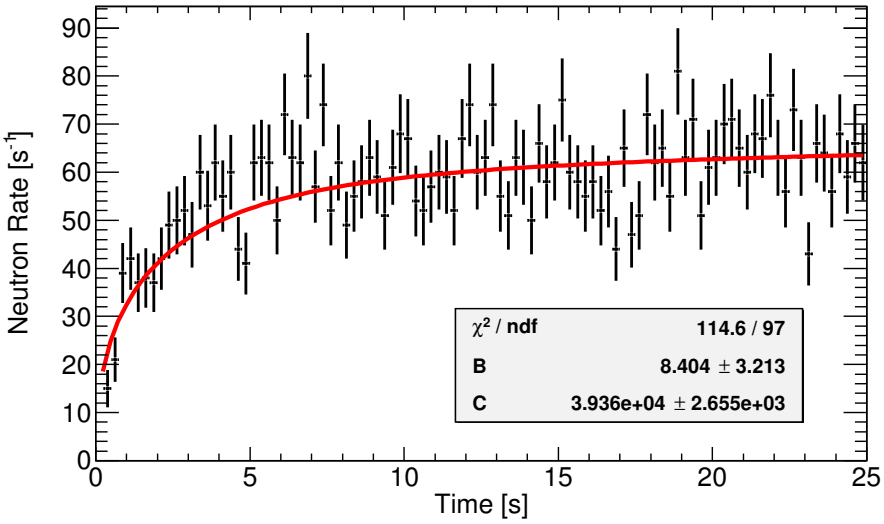

(b)

Figure 6.14: β-delayed neutrons detected between AI pulses for (a) HEU and (b) DU when the beam is turned on ($t = 0$). The fit to the model in Eq. (6.2) is shown in red.

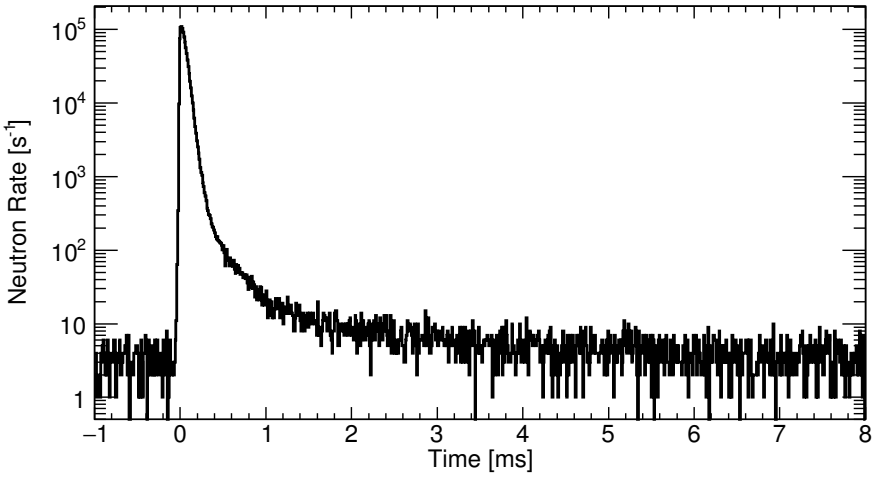

Figure 6.15: Summed neutron rate determined from approximately 15 minutes of DT generator operation.

to the measured decay data for each isotope, and similarly shown in Fig. 6.17. Higher delayed neutron count rates are observed for HEU in both the buildup and decay time distributions. This is expected due to the greater HEU object mass and higher delayed neutron microscopic fission cross-section of the HEU sample for 14.1 MeV neutrons.

In addition to HEU and DU objects, a tungsten object was also measured. The neutron buildup and decay rates were measured in the same manner as for the uranium objects and are shown in Fig. 6.18. As expected, there was no appreciable neutron rate observed in either the buildup or decay time periods.

An optimization of D was performed for the measured delayed-neutron buildup and decay rates. The start and stop times for A_1 were fixed to 0 and 25 s for the buildup time distribution and 0 and 30 s for the decay-time distribution. The value of D for all combinations of the start and stop times of A_2 was then calculated. Figure 6.19 shows a 2D histogram of different start and stop times for A2 and the resulting D for the buildup of delayed neutrons. The maximum value of D in Fig. 6.19 represents the greatest degree of differentiability between ^{235}U and ^{238}U. A start time of 0 s and a stop time of 4 s corresponding to the maximum value of D was selected for A_2 for the buildup

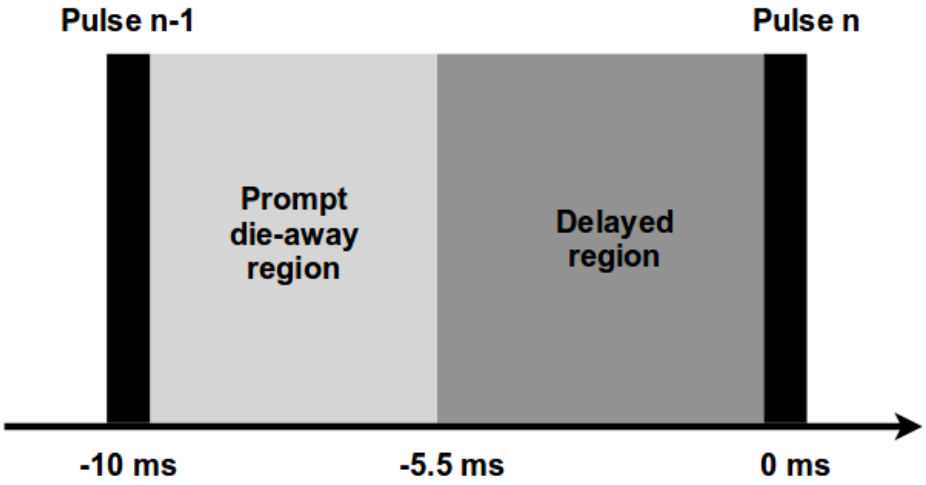

Figure 6.16: Graphical representation of the prompt die-away and delayed region for neutron event selection.

of delayed neutrons. Similarly, an optimization of D for the decay of delayed neutrons was performed, resulting in an A_2 start time of 0 s and stop time of 3 s.

The F values for the buildup and decay are unique for a given enrichment. Using the optimized limits of A_2 for both the buildup and decay of delayed neutrons, experimental F values were calculated for the HEU and DU samples. The experimental results are shown in Fig. 6.20 along with the simulated F values for the buildup and decay of delayed neutrons for enrichment levels ranging from 0 to 100%.

The F values calculated from the experimental results are used to establish a range of enrichment for the interrogated object. Table 6.3 shows the calculated range of enrichment based on the measurement. The uncertainty in the calculated enrichment is smaller for the HEU sample due to its higher neutron rates. Even with the relatively low statistics available in this experiment in which the detector subtended only a small solid angle, important conclusions can be quickly drawn about the interrogated objects. First, the presence of HEU can be confirmed by measuring either the buildup or the decay neutron emission rate. The enrichment of the DU object had an upper bound of 25%, which is well below weapons-grade HEU levels. Finally, the control tungsten object was

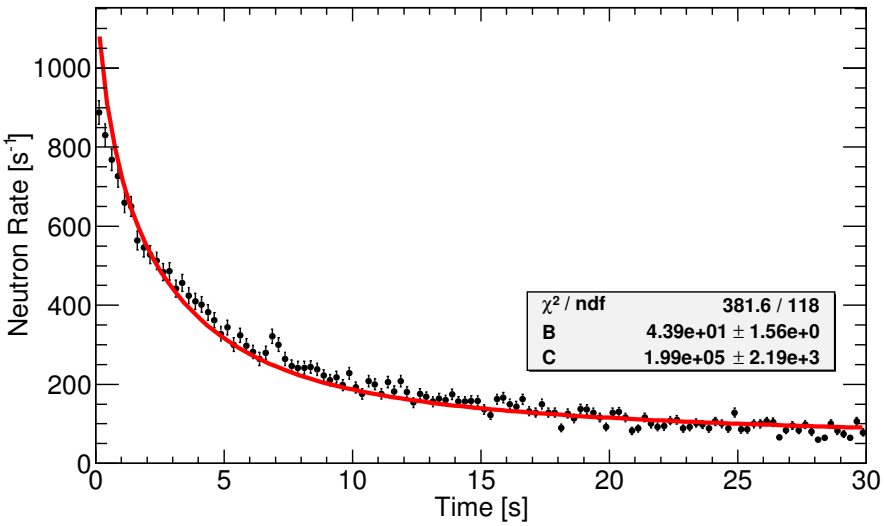

(a)

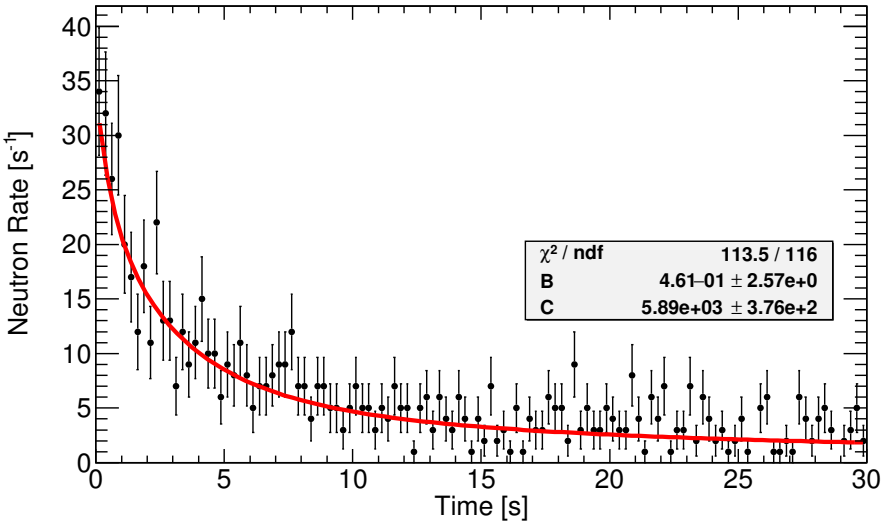

(b)

Figure 6.17: β-delayed neutrons observed after AI beam is turned off (t_b = 30 s) for (a) HEU and (b) DU. The fit to model in Eq. (6.3) is shown in red.

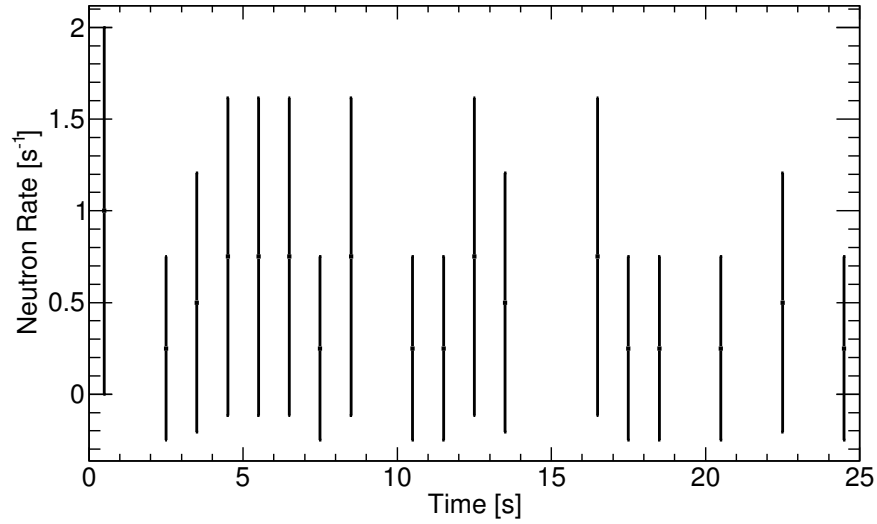

(a)

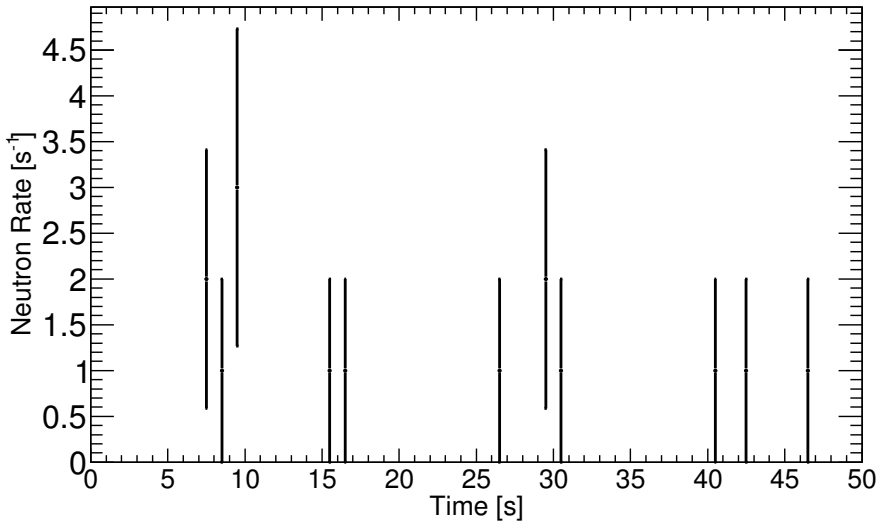

(b)

Figure 6.18: Detected neutron rate observed (a) between AI pulses, with the generator turned on ($t = 0$) and (b) after the generator has been turned off ($t = 0$) for the tungsten object.

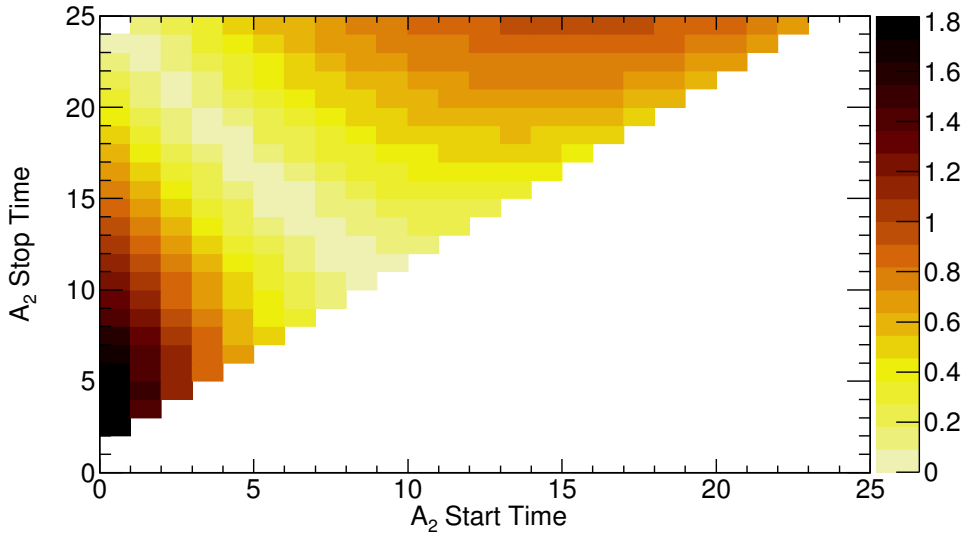

Figure 6.19: Optimization of D based on varying start and stop times of area A_2 for the buildup of delayed neutrons.

Table 6.3: Uranium enrichment 1σ range inferred from the experiment and comparison with the actual enrichment.

Sample	Actual	Buildup	Decay	Combined
HEU	93.2%	$92.7^{+7.3}_{-3.3}\%$	$100^{+0}_{-14}\%$	$96.3^{+3.7}_{-7.1}\%$
DU	0.7%	$0^{+35}_{-0}\%$	$7^{+28}_{-7}\%$	$3.5^{+21.3}_{-3.5}\%$

confirmed not to contain appreciable quantity of fissionable material. Accuracy of these measurements could be greatly improved with longer counting times and larger detector coverage area.

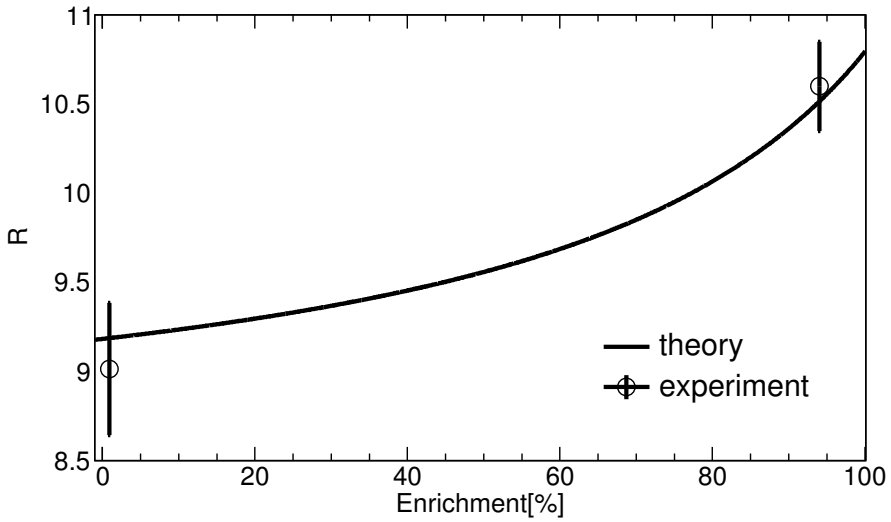

(a)

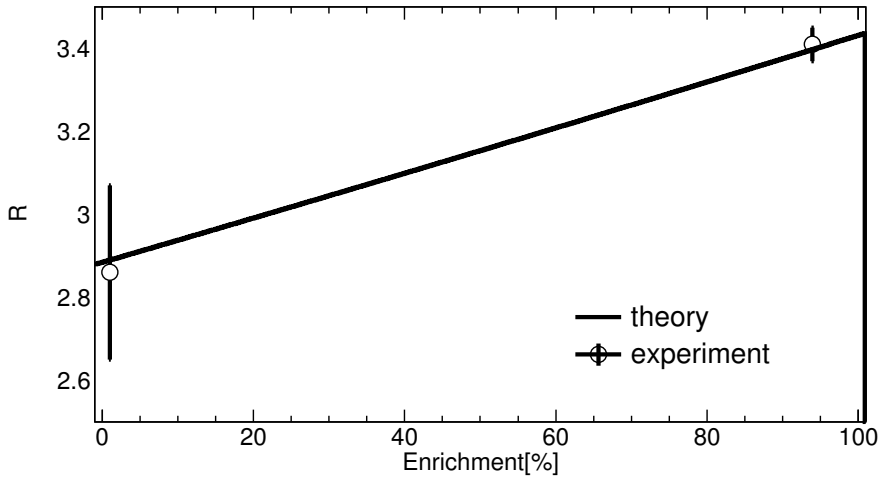

(b)

Figure 6.20: Simulated and measured F values for the (a) buildup and (b) decay of delayed neutrons for varying levels of enrichment.

6.4 Summary

A technique was demonstrated that can be used to verify the presence of SNM. Further, a method to determine uranium enrichment using both the delayed neutron buildup or the decay time emission profile was presented. The shape of the delayed neutron time profile, and thus the enrichment metric used, are not expected to be sensitive to shielding and self-shielding , as is the case with the alternative method that employs the intensities of characteristic gamma rays. With greater detector coverage and longer counting times, this technique could prove to be a powerful tool for uranium enrichment determination in various nonproliferation applications. By employing capture-gated composite scintillation detectors similar to the one employed in this proof-of-concept study, large coverage could be realized at a cost that is low to moderate and employs no ^{3}He detectors. Measuring enrichment values over the full range of enrichment would further validate the performance of this technique, which is one of the future experimental goals.

Chapter 7

Conclusions and future work

7.1 Summary and conclusions

The ever-changing nuclear nonproliferation and security climate calls for new, innovative approaches to detect and characterize nuclear materials. These applications range from spent nuclear fuel characterization to screening cargo containers for shielded SNM. The key components – radiography and the induced fission signature – of AI systems are well-suited to penetrate dense shielding and increase fission signatures to detectable levels. In this work a non-traditional AI system has been demonstrated that utilizes dual-mode multiple-energy transmission radiography to readily distinguish high-Z materials. The AI source consists of MeV neutrons and gamma rays, which provide complementary information. Neutrons are more easily shielded by low-Z materials, whereas high-Z materials more easily shield photons. The difference in these interaction properties means dual-mode AI systems provide broader probing capability as compared to single-mode systems. Further, this work uses multiple neutron energies, thereby increasing the range of attenuation that can accurately be measured compared to a pure gamma-ray attenuation metric.

To enable high-energy photon spectroscopy, a versatile calibration method was devel-

oped, which can be readily applied to any organic scintillator. The method uses many features in the light output spectrum to establish an accurate calibration. By examining how the light output distribution changes as a function of photon energy, prominent features were identified in the light output spectra of an organic scintillator never before used for energy calibration. The method offers a more accurate calibration compared to other traditional organic scintillator calibration methods. This technique provides scientists with an easy method to enable photon spectroscopy for organic scintillators over a much broader energy range.

Material identification using dual-energy photon transmission radiography was performed by measuring two characteristic gamma-ray energies with a liquid scintillation detector from the ^{nat}B(d,nγ)^{12}C reaction. Although this technique is well suited to determine moderate differences in atomic number, material discrimination becomes challenging among high-Z materials or for very small differences atomic number, where the ratio of mass attenuation coefficients displays slight variation for small differences in atomic number.

For the first time, a low-energy nuclear reaction based AI source was used to perform dual-mode multiple-energy transmission radiography. This dissertation also demonstrated the first use of liquid scintillators to simultaneously perform spectroscopic photon and neutron transmission radiography with a single type of detector. Additionally, this was the first experiment to explore the feasibility of a deuteron-BN source for use in an AI system.

A less-exploited transmission radiography technique combining neutron and photon transmission was explored utilizing a deuteron-BN AI source. It has been shown that by using different particles' experimentally measured transmission, a higher sensitivity to changes in elemental composition is achieved across the periodic table. Four preliminary metrics were developed based on neutron and gamma-ray transmission and show

promise for improved material discrimination. Reconstruction of the elemental composition for various materials using combined neutron-photon transmission radiography was successful. A dual-particle, multi-energy radiography technique was demonstrated for the first time based on the deuteron-BN source. This work was the first demonstration of a single-detector type and single-source AI technique.

Next, a method was established that can be used to confirm the presence of fissile material and quantify uranium enrichment. This new technique uses both the buildup and decay of β-delayed neutron emission profile as a means to determine enrichment. The shape of the delayed neutron time profile, and thus the enrichment metric used, is not expected to be sensitive to shielding or self-shielding. This is in contrast with the alternative method based on the intensities of characteristic gamma rays. With greater detector coverage and longer counting times, this technique could prove to be a powerful tool for uranium enrichment determination in various nonproliferation applications. The method may also be adaptive to detection of plutonium. By employing capture-gated composite scintillation detectors like the one used in this proof-of-concept study, large coverage could be realized at a cost that is low to moderate and employs no ^{3}He detectors. A complete material characterization system would include the dual-radiation AI source, particle transmission detectors and delayed-neutron detectors. Although capture-based detectors were used here to detect delayed neutrons, a liquid scintillator could be used as well. As such, a system could be envisioned which measures all signals with only one type of detector. Such a system would likely be more scalable and less complicated than a system which uses various detector types.

7.2 Future work

In the work presented in this thesis as well as prior work using the ^{nat}B(d,nγ)^{12}C reaction for AI [31, 32], large accelerators were used to generate probing radiation. Atomic numbers of various objects are inferred by dual-energy photon radiography or by dual-radiation multi-energy radiography. Other work using using dual-energy transmission radiography combined the use of a small, compact neutron generator and a radioisotope gamma-ray source [110]. In the case of the combined neutron/gamma-ray AI source, the system was able to produce highly resolved radiographic images of air freight containers. The gamma-ray energy was less penetrating than the work conducted in Refs. [31, 32], but had a small overall footprint. The lesser degree of penetration by the AI source could be a limitation in the presence of heavy shielding. In Refs. [31, 32] and in this work, more penetrating AI radiation was available but came at the cost of increased size of the system. Although other AI sources such as superconducting cyclotrons have been suggested, their effective use still needs to be demonstrated in this context. Further, despite the development of an advanced SNM AI detection system capable of producing 3D images of cargo and verifying the presence of fissionable material by detecting prompt neutrons from photofission [129], the required scanning times are still well above what is needed to achieve 100% clearance.

The problem of quickly detecting shielded SNM in the presence of heavy shielding remains without a fully proven solution. Many nuclear reactions and combinations of penetrating radiation sources still have yet to be explored as potential AI sources. Further exploration of combining low-energy nuclear reactions and radioisotope sources is still needed to detect shielded SNM. AI sources that combine multiple signatures could be used to accurately identify the atomic number of unknown material. There is still no existing system that meets all radiation dose and time requirements. More work concentrating on effectively combining signals from radiography and fission is still needed. In

addition, approaches for combining information using reduction techniques such as principal component analysis and machine learning should be investigated for implementation into the AI/detector system.

References

[1] C. Geddes, B. Ludewigt, J. Valentine, B. Quiter, M.-A. Descalle, G. Warren, M. Kinlaw, S. Thompson, D. Chichester, C. Miller, *et al.*, "Impact of monoenergetic photon sources on nonproliferation applications final report," tech. rep., Idaho National Lab.(INL), Idaho Falls, ID (United States), 2017.

[2] D. Eisenhower, *Atomic Power for Peace*. Division of Publications, 1953.

[3] A. C. Association *et al.*, "Nuclear weapons: Who has what at a glance," *Arms Control Association*, 2018.

[4] H. Kristensen and R. Norris, "United States nuclear forces, 2018," *Bulletin of the Atomic Scientists*, vol. 74, no. 2, pp. 120–131, 2018.

[5] C. Meade and R. Molander, "Considering the effects of a catastrophic terrorist attack," 2006.

[6] C. Abt, "The economic impact of nuclear terrorist attacks on freight transport systems in an age of seaport vulnerability," *Report by Abt Associates Inc.*, 2003.

[7] R. Kouzes, "Detecting illicit nuclear materials: The installation of radiological monitoring equipment in the united states and overseas is helping thwart nuclear terrorism," *Am. Sci.*, vol. 93, no. 5, pp. 422–427, 2005.

[8] R. Runkle, L. Smith, and A. Peurrung, "The photon haystack and emerging radiation detection technology," *J. Appl. Phys.*, vol. 106, no. 4, p. 7, 2009.

[9] P. Crist, *Security in maritime transport: risk factors and economic impact*. Organisation for Economic Co-operation and Development, 2003.

[10] C. Grassley, M. Baucus, B. Thomas, and C. Rangel, "Container security: Expansion of key customs programs will require greater attention to critical success factors," in *General Accounting Office, US Congress, GAO-03-770*, 2003.

[11] S. Martonosi, D. Ortiz, and H. Willis, "12. evaluating the viability of 100 per cent container inspection at america's ports," *The economic impacts of terrorist attacks*, vol. 218, 2007.

[12] M. Thibault, M. Brooks, and K. Button, "The response of the us maritime industry to the new container security initiatives," *Transportation Journal*, pp. 5–15, 2006.

[13] U. Congress, "Security and accountability for every port act," *Public Law*, pp. 109–347, 2006.

[14] T. Cochran and M. McKinzie, "Detecting nuclear smuggling," *Sci. Am.*, vol. 298, no. 4, pp. 98–104, 2008.

[15] R. Berndt, E. Franke, and P. Mortreau, "^{235}U enrichment or UF_6 mass determination on UF_6 cylinders with non-destructive analysis methods," *Nucl. Instrum. Methods Phys. Res., Sect. A*, vol. 612, no. 2, pp. 309 – 319, 2010.

[16] R. Runkle, A. Bernstein, and P. Vanier, "Securing special nuclear material: Recent advances in neutron detection and their role in nonproliferation," *J. Appl. Phys.*, vol. 108, no. 11, p. 13, 2010.

[17] T. Reilly, R. Walton, and J. Parker, "Progress report LA-4605-MS," *Los Alamos National Laboratory, NNM (197)*, vol. 19, 1970.

[18] R. Augustson and T. Reilly, "Fundamentals of passive nondestructive assay of fissionable material," *AEC Contract W-740 S-ENG. 36*, p. 1, 1974.

[19] P. Matussek, "Accurate determination of the ^{235}U isotope abundance by gamma spectrometry," *Tech. Rep. KFK–3752 Kernforschungszentrum Karlsruhe G.M.B.H.*, 1985.

[20] I. Jovanovic and A. Erickson, "Active interrogation in nuclear security,"

[21] D. Reilly, N. Ensslin, H. Smith Jr, and S. Kreiner, "Passive nondestructive assay of nuclear materials," tech. rep., Nuclear Regulatory Commission, Washington, DC (United States). Office of Nuclear Regulatory Research; Los Alamos National Lab., NM (United States), 1991.

[22] A. Lavietes, J. Trebes, R. Borchers, J. Dahlburg, J. Donnelly, A. Isles, N. Johnson, G. Knoll, R. Kouzes, R. Lanza, *et al.*, "Technical review of the domestic nuclear detection office transformational and applied research directorate's research and development program," 2013.

[23] S. Fetter, V. Frolov, M. Miller, R. Mozley, O. Prilutsky, S. Rodionov, and R. Sagdeev, "Detecting nuclear warheads," *Science & Global Security*, vol. 1, no. 3-4, pp. 225–253, 1990.

[24] B. Centerfor, "Nuclear terrorism fact sheet," 2010.

[25] B. Jacobson, "Dichromatic absorption radiography. dichromography," *Acta radiologica*, no. 6, pp. 437–452, 1953.

[26] S. Kappadath and C. Shaw, "Dual-energy digital mammography: Calibration and inverse-mapping techniques to estimate calcification thickness and glandular-tissue ratio," *Med. Phys.*, vol. 30, no. 6, pp. 1110–1117, 2003.

[27] Y. Liu, B. Sowerby, and J. Tickner, "Comparison of neutron and high-energy x-ray dual-beam radiography for air cargo inspection," *Appl. Radiat. Isot.*, vol. 66, no. 4, pp. 463–473, 2008.

[28] G. Chen, G. Bennett, and D. Perticone, "Dual-energy x-ray radiography for automatic high-z material detection," *Nucl. Instrum. Methods Phys. Res., Sect. B*, vol. 261, no. 1-2, pp. 356–359, 2007.

[29] B. Quiter, S. Prussin, B. Pohl, J. Hall, J. Trebes, G. Stone, and M. Descalle, "A method for high-resolution x-ray imaging of intermodal cargo containers for fissionable materials," *J. Appl. Phys.*, vol. 103, no. 6, p. 064910, 2008.

[30] J. Jones, J. Sterbentz, W. Yoon, and D. Norman, "Bremsstrahlung versus monoenergetic photon dose and photonuclear stimulation comparisons at long standoff distances," in *AIP Conference Proceedings*, vol. 1194, pp. 43–48, AIP, 2009.

[31] P. Rose, A. Erickson, M. Mayer, J. Nattress, and I. Jovanovic, "Uncovering special nuclear materials by low-energy nuclear reaction imaging," *Sci. Rep.*, vol. 6, 04 2016.

[32] B. Henderson, H. Lee, T. MacDonald, R. Nelson, and A. Danagoulian, "Experimental demonstration of multiple monoenergetic gamma radiography for effective atomic number identification in cargo inspection," *J. Appl. Phys.*, vol. 123, no. 16, p. 164901, 2018.

[33] B. O'Day III, Z. Hartwig, R. Lanza, and A. Danagoulian, "Initial results from a multiple monoenergetic gamma radiography system for nuclear security," *Nucl. Instrum. Methods Phys. Res., Sect. A*, vol. 832, pp. 68–76, 2016.

[34] S. Naydenov, V. Ryzhikov, and C. Smith, "Direct reconstruction of the effective atomic number of materials by the method of multi-energy radiography," *Nucl. Instrum. Methods in Physics Res., Sect. B*, vol. 215, no. 3-4, pp. 552–560, 2004.

[35] P. Hausladen, P. Bingham, J. Neal, J. Mullens, and J. Mihalczo, "Portable fast-neutron radiography with the nuclear materials identification system for fissile material transfers," *Nucl. Instrum. Methods Phys. Res., Sect. B*, vol. 261, no. 1-2, pp. 387–390, 2007.

[36] K. Ogren, J. Nattress, and I. Jovanovic, "Spectroscopic fast neutron transmission imaging in a treaty verification setting," *AIP Advances*, vol. 8, no. 1, p. 015205, 2018.

[37] J. Rahon, A. Danagoulian, T. MacDonald, Z. Hartwig, and R. Lanza, "Spectroscopic neutron radiography for a cargo scanning system," *Nucl. Instrum. Methods Phys. Res., Sect. A*, vol. 820, pp. 141–145, 2016.

[38] N. King, E. Ables, K. Adams, K. Alrick, J. Amann, S. Balzar, P. Barnes Jr, M. Crow, S. Cushing, J. Eddleman, *et al.*, "An 800-mev proton radiography facility for dynamic experiments," *Nucl. Instrum. Methods Phys. Res., Sect. A*, vol. 424, no. 1, pp. 84–91, 1999.

[39] W. Priedhorsky, K. Borozdin, G. Hogan, C. Morris, A. Saunders, L. Schultz, and M. Teasdale, "Detection of high-z objects using multiple scattering of cosmic ray muons," *Rev. Sci. Instrum.*, vol. 74, no. 10, pp. 4294–4297, 2003.

[40] K. Borozdin, G. Hogan, C. Morris, W. Priedhorsky, A. Saunders, L. Schultz, and M. Teasdale, "Surveillance: Radiographic imaging with cosmic-ray muons," *Nature*, vol. 422, no. 6929, p. 277, 2003.

[41] C. Morris, K. Borozdin, J. Bacon, E. Chen, Z. Lukić, E. Milner, H. Miyadera, J. Perry, D. Schwellenbach, D. Aberle, *et al.*, "Obtaining material identification with cosmic ray radiography," *AIP Advances*, vol. 2, no. 4, p. 042128, 2012.

[42] R. Runkle, D. Chichester, and S. Thompson, "Rattling nucleons: New developments in active interrogation of special nuclear material," *Nucl. Instrum. Methods Phys. Res., Sect. A*, vol. 663, no. 1, pp. 75 – 95, 2012.

[43] J. Duderstadt and L. Hamilton, "Nuclear reactor analysis," 1976.

[44] G. Keepin, *Physics of Nuclear Kinetics*. Addison-Wesley Pub. Co., 1965.

[45] A. Antolak, B. Doyle, K.-N. Leung, D. Morse, and P. Provencio, "Active interrogation using low-energy nuclear reactions," in *Penetrating Radiation Systems and Applications VII*, vol. 5923, p. 592303, International Society for Optics and Photonics, 2005.

[46] T. Taddeucci, R. Sheffield, T. Massey, D. Carter, J. ODonnell, C. Brune, D. Ingram, D. Jacombs, and A. DiLullo, "Neutron and gamma-ray production with low-energy beams," *Los Alamos National Laboratories Report LA-UR-07-2724*, 2007.

[47] M. Norsworthy, S. Clarke, C. Miller, S. Pozzi, and T. Antaya, "Active interrogation source based on deuteron reactions," in *Nuclear Science Symposium and Medical Imaging Conference (NSS/MIC), 2011 IEEE*, pp. 1362–1366, IEEE, 2011.

[48] J. Nattress and I. Jovanovic, "Response and calibration of organic scintillators for gamma-ray spectroscopy up to 15-MeV range," *Nucl. Instrum. Methods Phys. Res., Sect. A*, vol. 871, pp. 1–7, 2017.

[49] M. Reginatto, "Overview of spectral unfolding techniques and uncertainty estimation," *Radiation Measurements*, vol. 45, no. 10, pp. 1323–1329, 2010.

[50] A. Enqvist, C. Lawrence, B. Wieger, S. Pozzi, and T. Massey, "Neutron light output response and resolution functions in EJ-309 liquid scintillation detectors," *Nucl. Instrum. Methods Phys. Res., Sect. A*, vol. 715, pp. 79–86, 2013.

[51] C. Bass, E. Beise, H. Breuer, C. Heimbach, T. Langford, and J. Nico, "Characterization of a 6 Li-loaded liquid organic scintillator for fast neutron spectrometry and thermal neutron detection," *Appl. Radiat. Isot.*, vol. 77, pp. 130–138, 2013.

[52] V. Anykeyev, A. Spiridonov, and V. Zhigunov, "Comparative investigation of unfolding methods," *Nucl. Instrum. Methods Phys. Res., Sect. A*, vol. 303, no. 2, pp. 350–369, 1991.

[53] C. Lawrence, A. Enqvist, M. Flaska, S. A. Pozzi, A. Howard, J. Kolata, and F. Becchetti, "Response characterization for an EJ-315 deuterated organic-liquid scintillation detector for neutron spectroscopy," *Nucl. Instrum. Methods Phys. Res., Sect. A*, vol. 727, pp. 21–28, 2013.

[54] J. Birks, *Theory and Practice of Scintillation Counting*. Pergamon Press; distributed in the Western Hemisphere by Macmillan, New York, 1964. 34–35,185–192,384–390.

[55] W. Leo, *Techniques for nuclear and particle physics experiments: a how-to approach*. 2012.

[56] D. Smith, R. Polk, and T. Miller, "Measurement of the response of several organic scintillators to electrons, protons and deuterons," *Nucl. Instrum. Methods*, vol. 64, no. 2, pp. 157–166, 1968.

[57] R. Craun and D. Smith, "Analysis of response data for several organic scintillators," *Nucl. Instrum. Methods*, vol. 80, no. 2, pp. 239–244, 1970.

[58] M. Berger and S. Seltzer, "XCOM photon cross sections," *Version 3.1, NISTIR*, 1999.

[59] M. Chadwick, P. Obložinskỳ, M. Herman, N. Greene, R. McKnight, D. Smith, P. Young, R. MacFarlane, G. Hale, S. Frankle, *et al.*, "ENDF/B-VII. 0: next generation evaluated nuclear data library for nuclear science and technology," *Nucl. Data Sheets*, vol. 107, no. 12, pp. 2931–3060, 2006.

[60] G. Knoll, *Radiation detection and measurement*. John Wiley & Sons, 2010. 99–100,558–560,581–589.

[61] J. Czirr and G. Jensen, "A neutron coincidence spectrometer," *Nucl. Instrum. Methods Phys. Res., Sect. A*, vol. 284, no. 2, pp. 365–369, 1989.

[62] N. Cherepy, R. Sanner, P. Beck, E. Swanberg, T. Tillotson, S. Payne, and C. Hurlbut, "Bismuth-and lithium–loaded plastic scintillators for gamma and neutron detection," *Nucl. Instrum. Methods Phys. Res., Sect. A*, vol. 778, pp. 126–132, 2015.

[63] F. Pino, L. Stevanato, D. Cester, G. Nebbia, L. Sajo-Bohus, and G. Viesti, "Detecting fast and thermal neutrons with a boron loaded liquid scintillator, ej-339a," *Appl. Radiat. Isot.*, vol. 92, pp. 6–11, 2014.

[64] H. Chou and C. Horng, "Integral test of a boron-10 loaded liquid scintillator for neutron detection," *Nucl. Instrum. Methods Phys. Res., Sect. A*, vol. 328, no. 3, pp. 522–525, 1993.

[65] G. Rich, K. Kazkaz, H. Martinez, and T. Gushue, "Fabrication and characterization of a lithium-glass-based composite neutron detector," *Nucl. Instrum. Methods Phys. Res., Sect. A*, vol. 794, pp. 15–24, 2015.

[66] M. Mayer, J. Nattress, V. Kukharev, A. Foster, A. Meddeb, C. Trivelpiece, Z. Ounaies, and I. Jovanovic, "Development and characterization of a neutron detector based on a lithium glass–polymer composite," *Nucl. Instrum. Methods Phys. Res., Sect. A*, vol. 785, pp. 117–122, 2015.

[67] A. Foster, A. Meddeb, K. Wilhelm, J. Nattress, Z. Ounaies, and I. Jovanovic, "Characterization of lithium-glass and polyvinyl toluene heterogeneous composites with varying geometries for fast neutron detection," *Nucl. Instrum. Methods Phys. Res., Sect. A*, vol. 905, pp. 29–32, 2018.

[68] E. N. D. File, B. Part, and V. Version, "National nuclear data center," *Brookhaven National Laboratory*, 1990.

[69] Eljen Technologies, "Neutron/Gamma PSD Liquid Scintillator Data Sheet EJ-301, EJ-309," Date Accessed: Apr 22, 2017.

[70] S. Agostinelli, J. Allison, K. a. Amako, J. Apostolakis, H. Araujo, P. Arce, M. Asai, D. Axen, S. Banerjee, G. . Barrand, *et al.*, "GEANT4 – a simulation toolkit," *Nucl. Instrum. Methods Phys. Res., Sect. A*, vol. 506, no. 3, pp. 250–303, 2003.

[71] J. Ziegler, M. Ziegler, and J. Biersack, "SRIM–the stopping and range of ions in matter (2010)," *Nucl. Instrum. Methods Phys. Res., Sect. B*, vol. 268, no. 11, pp. 1818–1823, 2010.

[72] J. Nattress, "Capture-gated neutron spectroscopy with a novel lithium-glass-polymer composite scintillation detector," 2015.

[73] S. Naeem, S. Clarke, and S. Pozzi, "Validation of Geant4 and MCNPX-PoliMi simulations of fast neutron detection with the EJ-309 liquid scintillator," *Nucl. Instrum. Methods Phys. Res., Sect. A*, vol. 714, pp. 98–104, 2013.

[74] M. Gohil, K. Banerjee, S. Bhattacharya, C. Bhattacharya, S. Kundu, T. Rana, G. Mukherjee, J. Meena, R. Pandey, H. Pai, *et al.*, "Measurement and simulation of neutron response function of organic liquid scintillator detector," *Nucl. Instrum. Methods Phys. Res., Sect. A*, vol. 664, no. 1, pp. 304–309, 2012.

[75] Z. Su-Ya-La-Tu, C. Zhi-Qiang, H. Rui, L. Xing-Quan, R. Wada, L. Wei-Ping, J. Zeng-Xue, X. Yin-Yin, L. Jian-Li, and S. Fu-Dong, "Study on gamma response function of EJ301 organic liquid scintillator with Geant4 and FLUKA," *Chin. Phys. C*, vol. 37, no. 12, p. 126003, 2013.

[76] Z. Hartwig and P. Gumplinger, "Simulating response functions and pulse shape discrimination for organic scintillation detectors with Geant4," *Nucl. Instrum. Methods Phys. Res., Sect. A*, vol. 737, pp. 155–162, 2014.

[77] S. Pozzi, E. Padovani, and M. Marseguerra, "MCNP-PoliMi: a Monte-carlo code for correlation measurements," *Nucl. Instrum. Methods in Physics Res., Sect. A*, vol. 513, no. 3, pp. 550–558, 2003.

[78] S. Pozzi, J. Mullens, and J. Mihalczo, "Analysis of neutron and photon detection position for the calibration of plastic (BC-420) and liquid (BC-501) scintillators," *Nucl. Instrum. Methods in Physics Res., Sect. A*, vol. 524, no. 1-3, pp. 92–101, 2004.

[79] A. Enqvist and I. Pázsit, "Calculation of the light pulse distributions induced by fast neutrons in organic scintillation detectors," *Nucl. Instrum. Methods in Physics Res., Sect. A*, vol. 618, no. 1-3, pp. 266–274, 2010.

[80] A. Tomanin, J. Paepen, P. Schillebeeckx, R. Wynants, R. Nolte, and A. Lavietes, "Characterization of a cubic EJ–309 liquid scintillator detector," *Nucl. Instrum. Methods Phys. Res., Sect. A*, vol. 756, pp. 45–54, 2014.

[81] S. Pozzi, M. Flaska, A. Enqvist, and I. Pázsit, "Monte carlo and analytical models of neutron detection with organic scintillation detectors," *Nucl. Instrum. Methods in Physics Res., Sect. A*, vol. 582, no. 2, pp. 629–637, 2007.

[82] R. Brun and F. Rademakers, "Root–an object oriented data analysis framework," *Nucl. Instrum. Methods Phys. Res., Sect. A*, vol. 389, no. 1-2, pp. 81–86, 1997.

[83] P. Sparrman, J. Lindskog, and A. Marelius, "An electron scintillation detector with good energy resolution," *Nucl. Instrum. Methods*, vol. 41, no. 2, pp. 299–304, 1966.

[84] G. Dietze, "Energy calibration of NE-213 scintillation counters by δ-rays," *IEEE Trans. Nucl. Sci.*, vol. 26, no. 1, pp. 398–402, 1979.

[85] H. Schölermann and H. Klein, "Optimizing the energy resolution of scintillation counters at high energies," *Nucl. Instrum. Methods*, vol. 169, no. 1, pp. 25–31, 1980.

[86] G. Dietze and H. Klein, "Gamma-calibration of NE 213 scintillation counters," *Nucl. Instrum. Methods Phys. Res.*, vol. 193, no. 3, pp. 549–556, 1982.

[87] R. Cherubini, G. Moschini, R. Nino, R. Policroniades, and A. Varela, "Gamma calibration of organic scintillators," *Nucl. Instrum. Methods Phys. Res., Sect. A*, vol. 281, no. 2, pp. 349–352, 1989.

[88] M. Norsworthy, A. Poitrasson-Rivière, M. Ruch, S. Clarke, and S. Pozzi, "Evaluation of neutron light output response functions in EJ-309 organic scintillators," *Nucl. Instrum. Methods Phys. Res., Sect. A*, vol. 842, pp. 20–27, 2017.

[89] A. Hristova, E. Vapirev, L. Tsankov, and V. Jordanov, "Compton edge energy calibration of organic detectors," *Int. J. Radiat. Appl. Instrum. Part A*, vol. 41, no. 9, pp. 887–889, 1990.

[90] L. Swiderski, R. Marcinkowski, M. Moszynski, W. Czarnacki, M. Szawlowski, T. Szczesniak, G. Pausch, C. Plettner, and K. Roemer, "Electron response of some low-Z scintillators in wide energy range," *J. Instrum.*, vol. 7, no. 06, p. P06011, 2012.

[91] T. Novotny, L. Buermann, S. Guldbakke, and H. Klein, "Response of NE213 liquid scintillation detectors to high-energy photons (7 MeV $< E_\gamma >$ 20 MeV)," *Nucl. Instrum. Methods Phys. Res., Sect. A*, vol. 400, no. 2-3, pp. 356–366, 1997.

[92] S. Ogorodnikov and V. Petrunin, "Processing of interlaced images in 4–10 MeV dual energy customs system for material recognition," *Phys. Rev. Spec. Top. Accel Beams*, vol. 5, no. 10, p. 104701, 2002.

[93] A. Gilbert, B. McDonald, S. Robinson, K. Jarman, T. White, and M. Deinert, "Non-invasive material discrimination using spectral x-ray radiography," *J. Appl. Phys.*, vol. 115, no. 15, p. 154901, 2014.

[94] A. Gilbert, B. McDonald, and M. Deinert, "Advanced algorithms for radiographic material discrimination and inspection system design," *Nucl. Instrum. Methods in Physics Res., Sect. B*, vol. 385, pp. 51–58, 2016.

[95] B. Ishkhanov, A. Kurilik, D. Rudenko, K. Stopani, and V. Shvedunov, "Multiple-beam method for object scanning," *Bulletin of the Russian Academy of Sciences: Physics*, vol. 72, no. 6, pp. 859–862, 2008.

[96] "DPP PSD User Manual - UM2580," October 2015. User's Manual for the DT 5730.

[97] P. Rose Jr and A. Erickson, "High-energy γ rays resulting from low-energy nuclear reactions in light nuclei," *Phys. Rev. C: Nucl. Phys.*, vol. 97, no. 6, p. 064305, 2018.

[98] J. Eberhardt, S. Rainey, R. Stevens, B. Sowerby, and J. Tickner, "Fast neutron radiography scanner for the detection of contraband in air cargo containers," *Appl. Radiat. Isot.*, vol. 63, no. 2, pp. 179–188, 2005.

[99] B. Sowerby and J. Tickner, "Recent advances in fast neutron radiography for cargo inspection," *Nucl. Instrum. Methods Phys. Res., Sect. A*, vol. 580, no. 1, pp. 799–802, 2007.

[100] K. Kang, H. Hu, Y. Xie, Q. Miao, Y. Yang, Y. Li, Z. Chen, and X. Wang, "Method and equipment for discriminating materials by employing fast neutron and continuous spectral x-ray," July 15 2008. US Patent 7,399,976.

[101] B. Sowerby and J. Tickner, "Radiographic equipment, international patent application no," tech. rep., PCT/AU03/01641, Filing date: 10 Dec, 2003.

[102] J. Rynes, J. Bendahan, T. Gozani, R. Loveman, J. Stevenson, and C. Bell, "Gamma-ray and neutron radiography as part of a pulsed fast neutron analysis inspection system1," *Nucl. Instrum. Methods Phys. Res., Sect. A*, vol. 422, no. 1-3, pp. 895–899, 1999.

[103] M. Brandis, V. Dangendorf, C. Piel, D. Vartsky, B. Bromberger, D. Bar, E. Friedman, I. Mardor, I. Mor, K. Tittelmeier, *et al.*, "Nuclear-reaction-based radiation source for explosives-and snm-detection in massive cargo," in *AIP Conference Proceedings*, vol. 1336, pp. 711–716, AIP, 2011.

[104] Z. Hartwig, "The ADAQ framework: An integrated toolkit for data acquisition and analysis with real and simulated radiation detectors," *Nucl. Instrum. Methods Phys. Res., Sect. A*, vol. 815, pp. 42–49, 2016.

[105] J. Kelley, J. Purcell, and C. Sheu, "Energy levels of light nuclei A = 12," Mar 2019.

[106] F. Ajzenberg-Selove, "Energy levels of light nuclei A = 15," Jan 2019.

[107] M. Taylor, R. Smith, F. Dossing, and R. Franich, "Robust calculation of effective atomic numbers: The Auto-Z_{eff} software," *Med. Phys.*, vol. 39, no. 4, pp. 1769–1778, 2012.

[108] M. Herman, C. S. E. W. Group, *et al.*, "ENDF-6 formats manual data formats and procedures for the evaluated nuclear data file ENDF/B-VI and ENDF/B-VII," tech. rep., Brookhaven National Laboratory (BNL) National Nuclear Data Center, 2009.

[109] H. Lemmel and P. McLaughlin, "BROND-2.2. Russian evaluated neutron reaction data library. summary documentation," tech. rep., International Atomic Energy Agency, 1994.

[110] N. Cutmore, Y. Liu, and J. Tickner, "Development and commercialization of a fast-neutron/x-ray cargo scanner," in *Technologies for Homeland Security (HST), 2010 IEEE International Conference on*, pp. 330–336, IEEE, 2010.

[111] F. Becchetti, R. Raymond, R. Torres-Isea, A. Di Fulvio, S. Clarke, S. Pozzi, and M. Febbraro, "Recent developments in deuterated scintillators for neutron measurements at low-energy accelerators," *Nucl. Instrum. Methods Phys. Res., Sect. A*, 2017.

[112] M. Carman, A. Glenn, A. Mabe, F. Becchetti, S. Payne, and N. Zaitseva, "Solution growth of a deuterated trans-stilbene crystal for fast neutron detection," *J. Cryst. Growth*, vol. 498, pp. 51–55, 2018.

[113] F. Becchetti, R. Torres-Isea, A. Di Fulvio, S. Pozzi, J. Nattress, I. Jovanovic, M. Febbraro, N. Zaitseva, and L. Carman, "Deuterated stilbene (stilbene-d12): An improved detector for fast neutrons," *Nucl. Instrum. Methods in Physics Res., Sect. A*, 2018.

[114] J. Nattress, M. Mayer, A. Foster, A. Meddeb, C. Trivelpiece, Z. Ounaies, and I. Jovanovic, "Capture-gated spectroscopic measurements of monoenergetic neutrons with a composite scintillation detector," *IEEE Trans. Nucl. Sci.*, vol. 63, no. 2, pp. 1227–1235, 2016.

[115] J. Nattress, K. Ogren, A. Foster, A. Meddeb, Z. Ounaies, and I. Jovanovic, "Discriminating uranium isotopes using the time-emission profiles of long-lived delayed neutrons," *Phys. Rev. Appl.*, vol. 10, no. 2, p. 024049, 2018.

[116] N. Bohr and J. Wheeler, "The mechanism of nuclear fission," *Phys. Rev.*, vol. 56, pp. 426–450, Sep 1939.

[117] M. Kinlaw and A. Hunt, "Fissionable isotope identification using the time dependence of delayed neutron emission," *Nucl. Instrum. Methods Phys. Res., Sect. A*, vol. 562, no. 2, pp. 1081 – 1084, 2006.

[118] M. Mayer, J. Nattress, and I. Jovanovic, "Detection of special nuclear material from delayed neutron emission induced by a dual-particle monoenergetic source," *Appl. Phys. Lett.*, vol. 108, no. 26, p. 264102, 2016.

[119] C. Moss, M. Brener, C. Hollas, and W. Myers, "Portable active interrogation system," *Nucl. Instrum. Methods Phys. Res., Sect. B*, vol. 241, no. 1, pp. 793 – 797, 2005.

[120] W. Myers, C. Goulding, and C. Hollas, "Determination of the ^{235}U enrichment of bulk uranium samples using delayed neutrons," *Tech. Rep. No. LA-UR-06-3984, Los Alamos National Laboratory*, 1 2006.

[121] M. Sellers, D. Kelly, and E. Corcoran, "An automated delayed neutron counting system for mass determinations of special nuclear materials," *J. Radioanal. Nucl. Chem.*, vol. 291, pp. 281–285, Feb 2012.

[122] X. Li, R. Henkelmann, and F. Baumgrtner, "Rapid determination of uranium and plutonium content in mixtures through measurement of the intensity time curve of delayed neutrons," *Nucl. Instrum. Methods Phys. Res., Sect. B*, vol. 215, no. 1, pp. 246 – 251, 2004.

[123] R. Kouzes, "The ^{3}He supply problem," *Tech. Rep. PNNL-18388, Pacific Northwest National Laboratory*, 5 2009.

[124] R. Rothe, "Extrapolated experimental critical parameters of unreflected and steel-reflected massive enriched uranium metal spherical and hemispherical assemblies," *Tech. Rep INEEL/EXT-97-01401, Lockheed Idaho Technologies Co., Idaho National Engineering and Environmental Lab.*, 1997.

[125] D. Chichester and E. Seabury, "Using electronic neutron generators in active interrogation to detect shielded fissionable material," in *Nuclear Science Symposium Conference Record, 2008. NSS'08. IEEE*, pp. 3361–3367, IEEE, 2008.

[126] M. Kinlaw and A. Hunt, "Time dependence of delayed neutron emission for fissionable isotope identification," *Appl. Phys. Lett.*, vol. 86, no. 25, p. 254104, 2005.

[127] D. Saphier, D. Ilberg, S. Shalev, and S. Yiftah, "Evaluated delayed neutron spectra and their importance in reactor calculations," *Nucl. Sci. and Engineering*, vol. 62, no. 4, pp. 660–694, 1977.

[128] G. Keepin, T. Wimett, and R. Zeigler, "Delayed neutrons from fissionable isotopes of uranium, plutonium and thorium," *J. Nucl. Energy*, vol. 6, no. 1-2, pp. IN2–21, 1957.

[129] W. Bertozzi, S. Korbly, R. Ledoux, and W. Park, "Nuclear resonance fluorescence and effective Z determination applied to detection and imaging of special nuclear material, explosives, toxic substances and contraband," *Nucl. Instrum. Methods Phys. Res., Sect. B*, vol. 261, no. 1-2, pp. 331–336, 2007.